Preparation and Characterization of Bioactive Silica-based Ceramics derived from Rice Husk Ash

A Thesis Submitted in Partial Fulfillment of the
Requirements for the Degree of

DOCTOR OF PHILOSOPHY

by

Jyoti Prakash Nayak
(Roll No. 507CR002)

Supervisor:
Dr. Japes Bera

DEPARTMENT OF CERAMIC ENGINEERING
NATIONAL INSTITUTE OF TECHNOLOGY, ROURKELA
AUGUST, 2010

Dedicated to my parents
and
years of hard work.....

NATIONAL INSTITUTE OF TECHNOLOGY
ROURKELA, INDIA

Dr. Japes Bera
Associate Professor,
Department of Ceramic Engineering,
N. I. T. Rourkela,
Rourkela- 769008, Orissa, India

18th August, 2010

CERTIFICATE

This is to certify that the thesis entitled "**Preparation and characterization of bioactive silica-based ceramics derived from rice husk ash**" being submitted by Mr. Jyoti Prakash Nayak for the degree of Doctor of Philosophy in Engineering from N.I.T. Rourkela, is a record of bonafied research work carried out by him under my supervision at the Department of Ceramic Engineering. In my opinion, this is a fit piece of work for submission for the degree of Doctor of Philosophy. To the best of our knowledge, the work has not been submitted to any other University or Institute for the award of any degree or diploma.

(Dr. J. Bera)

Mail ID: jbera@nitrkl.ac.in, jbera@rediffmail.com
Phone No: +91-661-2462201 (O), +91-661-2463204 (R), +91-9437246159 (M)

ACKNOWLEDGEMENTS

With deep regards and profound respect, I avail this opportunity to express my deep sense of gratitude and indebtedness to Prof. Japes Bera, Department of Ceramic Engineering, N. I. T. Rourkela, for introducing the present research topic and for inspiring guidance. Two things that I have learned from him-quantitative approaches of scientific problems and critical evaluation of results will be the invaluable legacy that I will carry on for the rest of my career.

I would like to express my gratitude to Prof. Santanu Bhattacharyya especially, for his valuable suggestions, encouragements and helps at various stages of the work. Including him, I want to thank other members of my thesis Advisory Committee: Prof. S. K. Pratihar and Prof. (Mrs.) S. Mishra (Department of Chemical Engineering), for their useful comments and suggestions for the work included in this thesis. I would also like to thank the professors in Ceramic Engineering department who I have a wonderful intellectual interaction with during my research work.

I express my sincere thanks to Prof. S. K. Sarangi, Director, NIT Rourkela for providing the financial assistanceship inform of institute fellowship, sponsored by MHRD, Government of India during the last year of my research work. I also want to thank Ministry of Environment and Forests, Govt. of India for sponsoring me to start the research work.

It was a nice and memorable association with all the staff of my department with whom I have enjoyed the working in research period- I wish to give them my heartfelt thanks.

Finally, I would like to thank my family - my wife Baby and my little angel "Gunu" who have been supporting me with love that I cherish the most. Last but definitely not least, my parents and my relatives are so lovingly acknowledged. My father, always catching my fall, all your support and endless encouragement is acknowledged. My mother, for all your encouragement and prayers are so much appreciated.

Maa Tarini - Namaste

Date: 18.08.2010 **(Jyoti Prakash Nayak)**

ABSTRACT

This thesis deals with the preparation and characterization of amorphous silica based bioactive ceramics using rice husk ash (RHA) as silica source. Three types of silica precursors were prepared depending on impurity and forms. Ceramics were fabricated through conventional powder compaction, polymeric sponge replication and gelcasting methods. Bioglass-ceramics and mesoporous silica aerogel were also prepared using silica precursor. Mechanical, *in vitro* bioactivity and biodegradability properties of above ceramics were investigated.

Brown ash (BA), obtained by burning husk at 700 ^{o}C, contains about 96 wt.% amorphous SiO_2 and the rest 4% impurities like CaO, Fe_2O_3, K_2O, ZnO, and Mn_2O_3. White ash (WA), prepared by burning acid-leached husk, and contains almost pure silica (99.86%). Silica gel (SG) powder was prepared from BA through the alkaline extraction of silica from ash followed by acid neutralization. SG contains about 99.79% silica. During sintering, amorphous silica transformed into cristobalite phase at 1000, 1200, and 1300 ^{o}C, respectively for BA, SG, and WA ceramics. The earlier phase transformation in BA was due to its highest impurity content. There was a fall in compressive strength of all three (BA, SG and WA) sintered silica ceramics as and when amorphous silica transformed to cristobalite. This was due to the crack formation by the high-low displacive phase transformation of cristobalite.

Amorphous silica based scaffolds were fabricated by slurry impregnation process using polymeric sponge as the replica. The aqueous slurry with 40 wt.% solid loading showed good thixotropic behaviour in presence of polyvinyl alcohol (PVA) binder. The strength of scaffold decreased above a sintering temperature where the amorphous silica transformed into cristobalite. *In vitro* bioactivity test showed the formation of apatite layer on silica scaffold surface.

Amorphous silica-based porous ceramics was also prepared by gel casting method using SG powder. The slurry with 42 vol.% solid loading in 1:30 (MBAM:AM) monomer cross-linker solution, showed good thixotropic behaviour and generated a good casting. Casted body also showed good machinability. Sintered gel-casted body having ~25% porosity showed a mechanical strength of 27.5 ± 0.2 MPa. *In vitro* bioactivity experiment showed the formation of apatite layer on silica body.

Soda-lime-silica based bioglass-ceramics was synthesized via sol-gel route utilizing sodium silicate, derived from rice husk ash. Gel powder was calcined at 700 °C for 2 h to get a reactive glass-ceramic powder. The calcined powder mainly contains combeite-I ($Na_6Ca_3Si_6O_{18}$) crystalline phase dispersed in amorphous glass matrix. The material was sintered at different temperatures ranging from 900-1050 ^oC for 2 h. Glass-ceramics sintered at 1000 ^oC showed better mechanical property among all. Strength of 1050 ^oC sintered body was low due to the formation of cracks in it.

Crystalline combeite phase of the glass-ceramics was found to dissolve easily in TRIS buffer solution. Carbonated hydroxyapatite was formed on the surface of the glass-ceramics within 3-days of incubation in SBF. 900 ^oC sintered body showed better bioactivity and biodegradability than others. On increasing sintering temperature, both bioactivity and biodegradability of glass-ceramic decreased due to the transformation of glass into crystalline phases. Optimum sintering temperature for the material should be around 950-1000 ^oC with respect to strength and bioactivity.

Silica aerogel was successfully prepared through ambient pressure drying method using sodium silicate that was derived from WA. Surface modification and strengthening of wet gel was obtained by aging it in tetraethylorthosilicate (TEOS)/ethanol solution. Low surface tension liquid *n*-heptane was used to suppress capillary stresses and associated shrinkage during ambient pressure drying. Aerogel with low density (0.67), high porosity (80%) and a specific surface area of 273 $m^2.g^{-1}$ was obtained. Mesoporous aerogel was tested for its bio-activity and degradability. Apatite was formed on aerogel surface within 7-days of incubation in SBF. Aerogel showed quick release of silicic acid in TRIS buffer solution during biodegradability test.

All these results suggest that the rice husk ash could be a promising low cost raw material for the preparation of bioactive amorphous silica, bioglass-ceramics and mesoporous aerogel. Reticulated and gelcasted porous ceramics, bioglass-ceramics and aerogel can be used as novel low cost biomaterial for different clinical applications like; scaffold for Tissue engineering, biosensor, drug delivery, and protein encapsulations etc.

Keywords:

Rice husk; Rice husk ash; Silica; Amorphous; Ceramics; Porous Ceramics; Scaffold; Gelcasting; Sol-gel; Glass-ceramics; Aerogel; Silanol; Bioactivity; Biodegradability; Apatite; Microstructure; Compressive strength.

CONTENTS

		Page No.
	Acknowledgement	iv
	Abstract	v
	Table of Contents	viii
	List of Figures	xiv
	List of Tables	xix
	Acronyms and Symbol	xx
Chapter 1 - Introduction		
1.1	Introduction	1
1.2	Layout of the Thesis	5
	References	7
Chapter 2 - Literature Review		
2.1	Amorphous Silica Derived from Rice Husk Ash	10
2.2	Bioactivity of Silica-based Ceramics	11
2.3	Bioactive Silica-based Ceramics by Powder Compaction Method	14
2.4	Bioactive Silica-based Scaffold Prepared by Polymer Sponge Replication Technique	15
2.5	Bioactive Silica-based Ceramics Prepared by Gelcasting Method	16
2.6	Bioglass-Ceramics	17
2.7	Silica Aerogel	20
2.8	Summary and Scope of Work	23
2.9	Objectives of Present Work	24
	References	25
Chapter 3 - Experimental Details		
3.1	**Preparation of Amorphous Silica Precursor**	32
	3.1.1 Preparation of Rice Husk Ash Silica	32
	3.1.2 Characterization of Ash Silica	32

3.1.2.1 Chemical Analysis 32
3.1.2.2 Phase Analysis 34
3.1.2.3 Fourier Transformed Infrared (FTIR) Analysis 34
3.1.3 Preparation of Silica Gel Precursor 35
3.1.4 Characterization of Silica Gel 35
3.1.4.1 Chemical, Phase and FTIR Analysis 35
3.1.4.2 Microstructure and EDS Analysis 36
3.2 **Silica Ceramics Prepared by Powder Compaction Method** 37
3.2.1 Preparation of Silica Ceramics 37
3.2.2 Characterization of Silica powders and Ceramics 38
3.2.2.1 Particle Size Distribution of BA, WA and SG Powders 38
3.2.2.2 Phase Analysis and Rietveld Quantitative Phase Analysis 39
3.2.2.3 Density and Porosity of Sintered Specimen 40
3.2.2.4 Mechanical Property 41
3.2.2.5 *In vitro* Bioactivity 41
3.2.2.6 *In vitro* Biodegradability 43
3.3 **Silica-based Scaffolds Prepared by Sponge Replication Technique** 45
3.3.1 Preparation of Silica Scaffolds 45
3.3.2 Characterization of Silica Powders and Scaffolds 46
3.3.2.1 Zeta-potential 46
3.3.2.2 Sedimentation Test 47
3.3.2.3 Slurry Rheology 47
3.3.2.4 Fabrication of Reticulated Porous Body 48
3.3.2.5 Sintering of Reticulated Porous Body 48
3.3.2.6 Density and Porosity of Sintered Specimen 49
3.3.2.7 Mechanical Property 49
3.3.2.8 *In vitro* Bioactivity 49
3.4 **Silica-Based Ceramics Prepared by Gelcasting Method** 50
3.4.1 Preparation of Gelcasted Body 50

3.4.2 Characterization of Gelcasted Body 50
3.4.2.1 Slurry Preparation 50
3.4.2.2 Fabrication of Gelcasted body 52
3.4.2.3 Thermal Decomposition Behaviour of Gelcast Body 53
3.4.2.4 Sintering and Mechanical Property of Gelcast Body 53
3.4.2.5 *In vitro* Bioactivity 53
3.5 **Sol-gel Synthesis of Glass-Ceramics** 54
3.5.1 Preparation of Glass-Ceramics 54
3.5.2 Characterization of Gel Powder and Glass-Ceramics 54
3.5.2.1 Thermal Analysis of Gel Powder 54
3.5.2.2 Sintering and Phase Analysis of Glass-Ceramics 54
3.5.2.3 Mechanical Properties of Glass-Ceramics 56
3.5.2.4 *In vitro* Bioactivity of Glass-Ceramics 56
3.5.2.5 *In vitro* Biodegradability of Glass-Ceramics 56
3.6 **Silica Aerogel by Ambient Pressure Drying** 56
3.6.1 Preparation of Silica Aerogel 56
3.6.2 Characterization of Aerogel 57
3.6.2.1 Density, Apparent Porosity, Microstructure and FTIR analysis 57
3.6.2.2 Surface Area and Pore Size Distribution 57
3.6.2.3 *In vitro* Bioactivity and Biodegradability of Aerogel 59
References 60

Chapter 4 – Results and Discussion

4.1 **Preparation and Characterization of Amorphous Silica Precursors** 61
4.1.1 Introduction 61
4.1.2 Results and Discussion 61
4.1.2.1 Phase Analysis 61
4.1.2.2 Chemical Analysis 63

4.1.2.3 FTIR Analysis 64
4.1.3 Summary 65
4.2 **Silica-based Ceramics Prepared by Powder Compaction Method** 66
4.2.1 Introduction 66
4.2.2 Results and Discussion 66
4.2.2.1 Particle Size Distribution 66
4.2.2.2 Phase Analysis 67
4.2.2.3 FTIR Analysis 69
4.2.2.4 Density and Apparent Porosity 70
4.2.2.5 Mechanical Property and Microstructure 72
4.2.2.6 *In vitro* Bioactivity 77
4.2.2.6.1 Phase Analysis 77
4.2.2.6.2 Microstructural Analysis 79
4.2.2.7 *In vitro* Biodegradability 80
4.2.3 Summary 81
4.3 **Silica-based Scaffold Prepared by Polymer Sponge Replication Technique** 82
4.3.1 Introduction 82
4.3.2 Results and Discussion 82
4.3.2.1 Particle Size Distribution 82
4.3.2.2 Zeta-potential 83
4.3.2.3 Sedimentation Behaviour 83
4.3.2.4 Slurry Rheology 84
4.3.2.5 Thermal Decomposition Behavior of Impregnated Sponge 86
4.3.2.6 Mechanical Property 87
4.3.2.7 *In vitro* Bioactivity 89
4.3.2.7.1 Phase Analysis 89
4.3.2.7.2 Microstructural Analysis 90
4.3.3 Summary 92
4.4 **Porous Silica Ceramics Prepared by Gelcasting Technique** 93

4.4.1 Introduction 93
4.4.2 Results and Discussion 93
4.4.2.1 Zeta-potential (ζ) 93
4.4.2.2 Sedimentation 94
4.4.2.3 Gelation Time 95
4.4.2.4 Slurry Rheology 97
4.4.2.5 Thermal Decomposition Behaviour of Gelcasted body 98
4.4.2.6 Mechanical Property 99
4.4.2.7 *In vitro* Bioactivity 101
4.4.2.7.1 Phase Analysis 101
4.4.2.7.2 Microstructural Analysis 102
4.4.3 Summary 102
4.5 **Sol-gel Glass-Ceramics** 103
4.5.1 Introduction 103
4.5.2 Results and Discussion 103
4.5.2.1 Thermal Decomposition of Gel Powder 103
4.5.2.2 Phase Analysis 104
4.5.2.3 Particle Size Distribution of Glass-ceramics Powder 106
4.5.2.4 Mechanical and Microstructural Properties 107
4.5.2.5 *In vitro* Bioactivity 108
4.5.2.5.1 Phase and Microstructural Analysis 108
4.5.2.5.2 Effect of Sintering on Bioactivity 111
4.5.2.6 *In vitro* Biodegradability 114
4.5.2.7 Physical Model 115
4.5.3 Summary 117
4.6 **Silica Aerogel Prepared by Ambient Pressure Drying** 118
4.6.1 Introduction 118
4.6.2 Results and Discussion 118

4.6.2.1 Ambient pressure Drying Mechanism 118
4.6.2.2 Aerogel and its Characterization 119
4.6.2.3 *In vitro* Bioactivity 123
4.6.2.4 *In vitro* Biodegradability 124
4.6.3 Summary 125
References 126
Chapter 5 – Epilogue
5.1 Conclusions 129
5.2 Scope of Future work 130
Publications resulting from the Ph.D. work 131
Curriculum Vitae 132

LIST OF FIGURES

Fig. No	Figure Caption	Page No
Chapter 3		
Fig. 3.1	Flow diagram for the preparation of BA and WA silica precursors.	33
Fig. 3.2	Silica hydrogel (a) and Dried Silica Gel (b).	35
Fig. 3.3	Flow diagram of the preparation of silica gel from BA.	34
Fig. 3.4	Flow diagram for the preparation of silica-based bioactive ceramics by powder compaction method.	38
Fig. 3.5	Absorbance at 820 nm as a function of concentration of silicon.	44
Fig. 3.6	Flow diagram for preparation of silica scaffolds.	45
Fig. 3.7	Schematic representation of electrical double layer and zeta-potential.	46
Fig. 3.8	(a) Optical photograph, and (b) SEM of raw sponge.	48
Fig. 3.9	Flow diagram for preparation of bioactive silica ceramics using gelcasting techniques.	51
Fig. 3.10	**(a);** (I) is the slurry in a beaker before gelling, (II) demolding of casted body from the beaker, (III) green gel casted body, (IV) dried cylindrical gelcated body, and **(b)** rod shaped demolded gel casted body along with PVC pipe and machined disk-shaped green bodies.	52
Fig. 3.11	Flow diagram of the procedure to prepare bioglass-ceramics.	55

Fig. 3.12 Flow diagram of the procedure used to prepare silica aerogel by ambient pressure drying technique using WA as silica source. 58

Chapter 4

Fig. 4.1 X-ray diffraction patterns for WA, BA, cleaned husk and raw husk. 61

Fig. 4.2 X-ray diffraction patterns for (a) Unwashed and (b) Washed Silica gel (SG). 62

Fig. 4.3 SEM and EDS photographs of (a) Unwashed and (b) Washed silica gel. 63

Fig. 4.4 FTIR spectra of (a) BA, (b) WA and (c) SG powders. 65

Fig. 4.5 Particle size distribution of BA, WA, and SG powders. 66

Fig. 4.6 Amorphous and crystalline XRD patterns of sintered specimen made of (a) BA, (b) SG, and (c) WA. Sintering temperature and crystalline phases are indicated. 67

Fig. 4.7 Rietveld refinement output for quantitative phase estimation of BA. 69

Fig. 4.8 FTIR spectra of BA, SG, and WA specimens. Sintering temperature is presented with each spectra. 70

Fig. 4.9 Variation of (a) bulk density and (b) water absorption of specimen with sintering temperature. 71

Fig. 4.10 Variation of compressive strength with sintering temperature. 73

Fig. 4.11 Surface microstructure of BA specimen sintered at different temperatures. 74

Fig. 4.12 Surface microstructure of SG specimen sintered at different temperatures. 75

Fig. 4.13 Surface microstructure of WA specimen sintered at different temperatures. 76

Fig. 4.14 XRD patterns of the silica ceramics after SBF incubation for different days; (a) BA (sintered at 900 ^{o}C), (b) SG (sintered at 1100 ^{o}C) and (c) WA (sintered at 1200 ^{o}C). 77

Fig. 4.15 Schematic diagram representing the events take place at the interface between amorphous silica ceramics and SBF. 78

Fig. 4.16 SEM images and EDS spectra of BA (a-b), SG (c-d) and WA (e-f) surfaces after incubation in SBF for 14 and 21 days respectively. 79

Fig. 4.17 (a) Change of silicon concentration, and (b) pH in TRIS medium with incubation time. 80

Fig. 4.18 Particle size distribution of different silica powders. 82

Fig. 4.19 Zeta potential of different silica powders with pH. 83

Fig. 4.20 Sedimentation heights as a function of pH for silica powders. 84

Fig. 4.21 Rheological behaviors of different silica slurries (a) shear rate vs. viscosity (b) shear rate vs. shear stress. 85

Fig. 4.22 BA-slurry impregnated dry sponge cubes. 86

Fig. 4.23 Fabricated green and sintered sponge cubes. 86

Fig. 4.24 Weight losses as a function of temperature (heating rate@10 ^{o}C/min) for impregnated sponge. 87

Fig. 4.25 Effect of sintering temperature on porosity of different RPCs. 87

Fig. 4.26 Effect of sintering temperature on compressive strength of the RPCs. 88

Fig. 4.27 Compressive stress-strain curve of the SG based RPC. 89

Fig. 4.28 XRD patterns of SG scaffold (a) without and (b) with SBF treatment. 90

Fig. 4.29	SEM micrographs and EDS graph of SG scaffold with (a) open and inter connected pores and (b, c, d, e) deposited carbonated HAp on strut boundary with sponge-wig like structure.	91
Fig. 4.30	Particle size distribution of silica gel powder.	93
Fig. 4.31	Zeta potential of silica gel powder with pH measured in 1:30 premix solution.	94
Fig. 4.32	Sedimentation behaviour of SG particles at different pH when dispersed in 1:30 premix solution.	95
Fig. 4.33	Variation of gelation time with initiator concentration (slurry with 42 vol.% solid loading).	96
Fig. 4.34	Optimized silica gel slurry after preparation.	97
Fig. 4.35	Rheological behavior of the optimized slurry.	97
Fig. 4.36	TGA-DSC curves of gelcast body at a heating rate of 10 ^{o}C/min.	98
Fig. 4.37	Different sintered shapes prepared by machining gelcasted ingot.	99
Fig. 4.38	Variation of porosity and compressive strength of gelcasted specimen with sintering temperature.	100
Fig. 4.39	XRD pattern of gelcasted SG-body after sintering at 1100 and 1200 ^{o}C.	100
Fig. 4.40	Surface microstructure of a gelcasted SG pellet after sintering at (a) 1100, and (b) 1200 ^{o}C.	101
Fig. 4.41	XRD patterns of SG scaffold (a) without, and (b) with SBF incubation.	101
Fig. 4.42	SEM and EDS of SG surface after 28 days SBF incubation.	102
Fig. 4.43	DSC-TGA plot of soda-lime-silicate gel powder.	104

Fig. 4.44 XRD patterns of gel powder; (a) as prepared, and after calcination at (b) 300 (c) 500 (d) 700 and (e) 900 ^{o}C. 105

Fig. 4.45 XRD patterns of glass-ceramics; (a) as prepared (b) powder calcined at 700 ^{o}C, and pellet sintered at (c) 900, (d) 950, (e) 1000, (f) 1050 ^{o}C. 106

Fig. 4.46 Particle size distribution of glass-ceramics powder. 107

Fig. 4.47 Change of bulk density, porosity and compressive strength of glass-ceramics with sintering temperatures. 108

Fig. 4.48 Surface microstructures of glass-ceramics those sintered at (a) 900, (b) 950, (c) 1000 and (d) 1050 ^{o}C. 109

Fig. 4.49 XRD patterns of glass-ceramic surface after incubation in SBF for different time periods. 110

Fig. 4.50 SEM image and EDS spectra of glass-ceramics; (a) as prepared, and after incubation in SBF for (b) 3 (c) 14, and (d) 21 days. 110

Fig. 4.51 XRD patterns of glass-ceramics specimen, (a) sintered at 900 ^{o}C; and the patterns after 3-days SBF incubation of specimen those sintered at (b) 900, (c) 950, (d) 1000, and (e) 1050 ^{o}C. 112

Fig. 4.52 SEM image and EDS spectra of 3-days SBF incubated glass-ceramic specimen those sintered at (a) 900, (b) 950 (c) 1000, and (d) 1050 ^{o}C respectively. 113

Fig. 4.53 Dissolution kinetics of glass-ceramics those sintered at different temperatures; (a) Change in pH of TRIS medium, and (b) water absorption capacity of specimen with incubation period. 114

Fig. 4.54 Schematic diagram representing the events take place at the interface between bioglass-ceramics and the SBF. 116

Fig. 4.55 Photographs of silica aerogel (a) strengthened by TEOS, (b) dried monolithic translucent piece. 119

Fig. 4.56 SEM and EDS photographs of silica aerogel. 120

Fig. 4.57 DSC/TGA curves of air-dried silica aerogel. 120

Fig. 4.58 FTIR spectra of silica aerogel after heating at different temperatures. 121

Fig. 4.59 Nitrogen adsorption-desorption isotherm of silica aerogel. 122

Fig. 4.60 Pore size distribution of silica aerogel. 122

Fig. 4.61 SEM images and EDS spectra of aerogel after incubation in SBF for (a) 7 (b) 14 and (c) 21 days. 123

Fig. 4.62 XRD pattern of aerogel specimen after 21-days incubation in SBF. 124

Fig. 4.63 Change of silicon concentration and pH in TRIS medium with incubation time for aerogel biodegradation. 125

LIST OF TABLES

Table No	Table Caption	Page No
Table 3.1	Amounts of reagents for preparation of SBF.	42
Table 4.1	Chemical analysis of raw materials (mass %).	64

Acronyms & Symbol

A	Area of Cross-section
APS	Ammonium persulfate
AM	Acrylamide
BA	Brown Ash
BD	Bulk density
BET	Brunauer-Emmet-Teller
BGC	Bioglass-ceramics
BOD	Biological Oxygen Demand
BSE	Back scattered electrons
D	Diameter
DTA	Differential thermal analysis
EDS	Energy dispersive X-ray analysis
EtOH	Ethanol
FTIR	Fourier Transformed Infrared
G	Goodness of fit
GC	Glass-ceramics
HAp	Hydroxyapatite
HCA	Hdroxycarbonate Apatite
Kg	Kilogram
kmol	Kilomole
MBAM	Methylene-bisacrylamide
min	Minutes
mL	Milliliter
mm	Millimeter
mol	Mole
MPa	Mega Pascal
MW	Molecular Weight
P	Breaking Load
P_o	Vapor pressure

pH	Potential of Hydrogen
PVA	Polyvinyl alcohol
PVC	Polyvinyl Chloride
RH	Rice Husk
RHA	Rice Husk Ash
SBF	Simulated Body Fluid
SE	Secondary Electron
SEM	Scanning Electron Microscope
SG	Silica Gel
T	Transmittance
TE	Tissue Engineering
TEMED	Tetramethylethylenediamine
TEOS	Tetraethyl orthosilicate
TGA	Thermo gravimetric analysis
TMOS	Tetramethyl orthosilicate
UV/VIS	Ultra Violet-Visible
vol	Volume
W_a	Suspended weight
W_d	Dry weight
W_s	Soaked weight
WA	White Ash
XRF	X-ray Fluorescence
XRD	X-ray diffraction
Y_i	Observed intensity
Y_{ic}	Calculated intensity
cm	Centimeter
gm	Gram
h	Hour (s)
K	Kelvin
KV	Kilo volt
nm	Nano meter

r	Radius
t	Thickness
wt	Weight
Å	Angstrom
θ	Bragg's angle
^{o}C	Degree Celsius
μ m	Micronmeter
g	Gram
β	Beta
α	Alpha
ζ	Zeta-potential
%	Percentage
~	About
±	Standard Deviation
<	Less than
>	Greater than
γ	Surface tension
π	Pie

Chapter 1

Introduction

1.1 Introduction

During the past four decades, a great revolution has occurred in the uses of ceramics to improve the quality of human life. This revolution is the innovative use of specially designed ceramics-termed as “bioceramics” for the potential replacement or repairing of lost, injured or diseased bone [1].

When a biomaterial is placed within the human body, tissue reacts towards the implant in a variety of ways depending on the material type. According to the tissue responses, a biomaterial may be classified into bioinert, bioactive, and bioresorbable [2]. The term bioinert refers to any materials that after introducing into the physiological environment, it will induce a minimal biological response with absence of toxic in nature [3]. Several ceramic materials, like titania, alumina, and partially stabilized zirconia are widely used clinically as bioinert materials.

A bioactive material can be defined as that able to form bone like apatite layer on its surface when in contact with physiological fluids in vivo or with simulated body fluids (SBF) [4]. This layer seems to be responsible for the bonding of bioactive ceramics to the living bone. Bioactive ceramics like, glass, glass-ceramics, hydroxyapatite (HAp), calcium phosphates, and calcium silicate have been used for practical clinical applications. Bioactive ceramics may be resorbable or non-resorbable. Bioresorbable refers to a material that upon placement within the living body starts to dissolve (resorbed) and slowly replaced by advancing tissue (such as bone). Common examples of bioresorbable ceramic material is tricalcium phosphate [$Ca_3(PO_4)_2$]. Calcium oxide, calcium carbonate and gypsum are other common bioresorbable materials that have also been utilized.

Bioactive ceramics have attracted increasing attention as promising biomaterials for bone tissue engineering [5]. Bone is a complex biomineralized system with an intricate hierarchical microstructure assembled through the deposition of apatite minerals within a collagenous matrix [6]. Even if bone is known for its self-healing abilities, it cannot grapple with larger defects. The current treatment methods used to treat bone defects such as transplantation and implantation do not restore the original function of the tissue it replaces. Thus, a tissue engineered solution is considered ideal [7].

Tissue engineering is the use of a combination of cells, engineering and materials methods to repair or replace portions of or whole tissues (i.e., bone, cartilage, blood vessels, bladder, skin etc.). A key component in tissue engineering for bone regeneration is the scaffold that serves as a template for cell interactions and the formation of bone-extracellular matrix to provide structural support to the newly formed tissues [8]. The clinical success of the tissue-engineered construct is critically dependent on the biomaterials and three-dimensional scaffolds which guide the growth of new tissue *in vitro* and in vivo [9].

Since the discovery of silica-based bioactive glass by Hench in 1971 and then ordered mesoporous silica materials in the early 1990s by scientists of the Mobil Corporation [10] and Waseda University [11], these materials lead to the development of a wide area of research on new silica-based bioactive materials for biomedical applications [12]. Recently, the potential applications of silica-based materials like, amorphous silica spheres [13], nano sphere of SiO_2-γFe_2O_3 [14], bioglass [15], bioactive glass-ceramics [16], mesoporous silica gel [17], silica aerogel [18] and silica star gel [19] have been expanded into the biomedical field for bone tissue regeneration and drug delivery purposes.

Silica in crystalline form induces adverse biological effects, while amorphous silica is known to be bioactive, biocompatible, biodegradable, and non-toxic in living tissue, as well as in corresponding simulated physiological conditions [20, 21]. Nowadays, along with above stated amorphous silica-based materials, amorphous fumed and precipitated silicas are increasingly used in diagnostic and biomedical research.

In general, amorphous silica is prepared using silicon alkoxide raw materials; such as tetramethylorthosilicate (TMOS), tetraethylorthosilicate (TEOS) and polyethoxydisiloxane (PEDS), etc [22, 23]. However, such precursors are fairly expensive [24]. Thus alternative low cost amorphous silica precursors are required to substitute alkoxides. In that respect, a cheap source of amorphous silica of bio-origin would be the rice husk ash (RAH). Although RHA contains minor amount of other metallic impurities; it may be safely used in physiological environment as it is generated from biomass.

Bioactive ceramics are used in the form of powder, densed ceramics, highly porous reticulated ceramics, mesoporous ceramics, etc. Dense and porous ceramics are fabricated through different methods like powder compaction, fiber bonding, solvent casting/particulate leaching, gas foaming, phase separation, replication technique, gelcasting, and sol-gel technique, etc [25-30]. Among them, powder compaction method is mostly applicable for dense ceramics, the rest are for porous ceramics preparation.

Powder compaction, is the simplest method of producing dense structures of rectangular, cubical, cylindrical and circular shapes. On the other hand, replication technique is the most popular and the simplest method for producing reticulated porous ceramics (RPC). The basic principle of this method involves dipping a sacrificial organic template (polymer sponge) in ceramic slurry, squeezing the excess slurry out, then drying at room temperature followed by pyrolysis and sintering which will eliminate the template and results in a RPC [31]. Nowadays, HAp, calcium phosphate, bioactive glass and glass-ceramics porous scaffolds are being fabricated through this route. Due to the presence of ordered 3D interconnected open cell porous structure analogous to the spongious bone, it allows cell attachment, proliferation, and differentiation, and pathways for biofluids [32]. However, the mechanical properties of RPC scaffold still remain poor due to the presence of high percent porosity and large pores.

Strength of porous body can be improved by decreasing pore size and increasing packing density of structure. Gelcast ceramics can provide these characteristics. Gel casting is a well-known wet forming method based on the combination of ceramic processing and polymer chemistry. This process involves the dispersion of a ceramic powder into a monomer solution and casting of this suspension into a non-porous mould. Polymerization is then promoted by initiator/catalyst and consequently ceramic particles are entrapped into the rigid and homogeneous polymeric network [33]. The main advantage of this method is the high strength of green body that assures its machinability. According to Jones and Hench [34], gel-casting results in the production of scaffolds most closely mimicking the structure of trabecular bone. Moreover, the sintered gel-cast bodies show relatively high mechanical strength than the RPCs due to their well-densified connecting-cells [35]. Different bioactive ceramics like HAp, calcium

phosphate, and glass-ceramics are fabricated to complex shapes by this method for different clinical applications.

As far as the bioactivity is concerned, silica-based glass and glass-ceramics are most bioactive among all bioceramics [36]. Bioactive glasses and glass-ceramics have attracted much attention towards clinical applications due to their good bioactivity, osteoconductivity and biodegradability characteristics [37-39]. Glass-ceramics have added advantage of better mechanical properties than glass [40]. Therefore, it is proposed that bioactive glass-ceramics with mechanical properties much closer to that of natural bone can be prepared [41]. Generally, glass-ceramics are prepared by the traditional melting, quenching, and subsequent preheating for crystallization of glass [42–44]. This method has disadvantage of evaporation of volatile component during high temperature processing [45]. An alternative approach to prepare glass-ceramics without melting operation is the sol-gel technique, which requires low processing temperature [46, 47]. This route enables a wide range of compositions with high purity, homogeneity and production of various shapes; such as monoliths, powders, fibers or coatings [48]. Additionally, glass-ceramics obtained by this route exhibit higher surface area and porosity which are the critical factors for their bioactivity [49]. Conventional sol-gel process uses expensive alkoxysilane precursors for glass preparation. Research is going on to get an alternative low cost silica source for sol-gel glass-ceramics. As stated above, RHA can be a low cost source of amorphous silica for sol-gel glass-ceramics, as the amorphous material can be easily dissolved into solution.

At present the most intense research work is going on in the area of ordered mesoporous silica for drug delivery and other biomedical applications. The important feature of mesoporous material is to host molecular size of particles within it. Silica aerogel is one such ordered mesoporous material and is also used in biomedical applications for controlled release of drugs, peptides, hormones, etc [50].

Aerogels are usually prepared by supercritical drying of wet silica gels [51-53]. However, supercritical drying process is so energy intensive and dangerous that real practice and commercialization of the process is difficult [54]. An alternative cost-effective process is required for commercial success for the production of aerogels.

Ambient pressure drying technique is an alternative process for aerogel synthesis. At the same time, the use of cost effective silica source (RHA) for the preparation of aerogel will be more economical and commercializable.

With this brief introduction about silica-based bioceramics and its different fabrication techniques, this work presents some attempts to prepare bioactive amorphous silica-based ceramics using rice husk ash and to characterize the bioactivity of these ceramics.

1.2 Layout of the Thesis

The thesis has been divided into five chapters:

Chapter-1 presents a brief introduction of different silica based bioactive ceramics, their fabrications and applications. The layout of the thesis is presented at the end of this chapter.

Chapter-2 consists of a thorough literature review. This chapter incorporates background information about amorphous silica derived from rice husk ash, bioactivity of silica-based ceramics, bioactive silica-based ceramics by powder compaction method, bioactive silica-based scaffolds prepared by polymer sponge replication technique, bioactive silica-based ceramics prepared by gelcasting method, bioglass-ceramics using sol-gel technique, and silica aerogel by ambient pressure drying.

Chapter-3 gives a detailed description of the experimental procedures, the materials, and the characterization methods used in this research work.

Chapter-4 describes the results and discussion, which has been divided into six sections, where, **section 1** speaks about the preparation and characterization of amorphous silica precursors, **section 2** explains about the preparation and characterization of bioactive silica ceramics by powder pressing method, **Section 3** describes about the properties of amorphous silica scaffolds prepared by polymeric sponge replication technique, **section 4** narrates the characteristics of bioactive silica ceramics prepared by gelcasting method, **section 5** tells about sol-gel synthesis and characterization of bioglass-ceramics using RHA as silica source and finally **section 6** discusses the preparation of silica aerogel by ambient pressure drying technique and its bioactivity characteristics.

Chapter-5 points out the conclusions based on the results of the investigation carried out in **chapter 4**, and it also gives remarks for future work that could be carried out for further exploitation of research.

A list of references has been given towards the end of each chapter. Finally, a list of publications in-peer reviewed national and international journals related to the present research work has been presented at the end.

References

[1] L.L. Hench, J. Am. Ceram. Soc. 74 [7] (1991) 1487.

[2] L.L. Hench, Biomaterials 19 (1998) 1419.

[3] S.M. Best, A.E. Porter, E.S. Thian, J. Huang, J. Eur. Ceram. Soc. 28 (2008) 1319.

[4] L.L. Hench, I.D. Xynos, J.M. Polak, J. Biomat. Sci. Polym E 15 (2004) 543.

[5] V. Maquet, A.R. Boccaccini, L. Pravata, I. Notingher, R. Jerome, Biomaterials 25 (2004) 4185.

[6] S.S. Liao, F.Z. Cui, W. Zhang, Q.L. Feng, J. Biomed. Mater. Res. B 69 (2004) 158.

[7] A.I. Muthutantri, Novel processing of porous bioceramics, Ph.D. thesis (2009).

[8] V. Karageorgiou, D. Kaplan, Biomaterials 26 (2005) 5474.

[9] A. Vats, N.S. Tolley, J.M. Polak, J.E. Gough, Clin. Otolaryngol. 28 (2003) 165.

[10] C. T, Kresge, M. E. Leonowicz, W. J. Roth, J. C. Vartuli, J. S. Beck, Nature 359 (1992) 710.

[11] T. Yanagisawa, T. Shimizu, K. Kuroda, C. Kato, Bull. Chem. Soc. Japan, 63 (1990) 988.

[12] A. Izquierdo-Barba, M. Colilla, M. Vallet-Regi, Journal of Nanomaterials, doi:10.1155/2008/106970.

[13] A. H. Lu, F. Schuth, Adv. Mater. 18 (2006) 1793.

[14] S. Mornet, J. Portier, E. Duguet, J. Magn. Magn. Mater. 293 (2005) 127.

[15] C. A. Harper, Handbook of Ceramics, Glasses and Diamonds, Blacklick, McGraw-Hill Professional Pub (2001).

[16] P. Li, Q. Yang, F. Zhang, T. Kokubo, J. Mater. Sci. Mater. Med. 3 (1992) 452.

[17] F. Balas, M. Manzano, P. Horcajada, M. Vallet-Regi, J. Am. Chem. Soc. 128 (2006) 8116.

[18] J.A. Toledo-Fernandez, R.O Mendoza-Serna, V. Morales, N. de la Rosa-Fox, M. Pinero, A. Santos, L. Esquivias, J. Mater. Sci-Mater Medicine 19 (2008) 2207.

[19] M. Manzano, D. Arcos, M. Rodriguez-Delgado, E. Ruiz, F. J. Gil, M. Vallet-Regi, Chem. Mater., vol. 18, pp. 5696-5703, 2006.

[20] P. Kortesuo, M. Ahola, S. Karlson, I. Kangasniemi, A. Yli-Urpo, J. Kiesvaara, Biomaterials 21 (2000) 193.

[21] A. nieto, S. Areva, T. Wilson, R. Viitala, M. Vallet-Regi, Acta Biomater. 5 (2009) 3478.

[22] S. Radin, G. El-Bassyouni, E.J. Vresilovic, E. Schepers, P. Ducheyne, Biomaterials 26 (2005) 1043.

[23] J. Andersson, J. Rosenholm, S. Areva, M. Linden, Chem. Mater. 16 (2004) 4160.

[24] Q. Tang, T. Wang, J. of Supercritical Fluids 35 (2005) 91.

[25] A.G. Mikos, A.J. Thorsen, L.A. Czerwonka, Y. Bao, R. Langer, D.N. Winslow, J.P. Vacanti, Polymer 35 (1994) 1068.

[26] Y.S. Nam, J.J. Yoon, T.G. Park, J. Biomed. Mater. Res. 53 (2000) 1.

[27] E. Ebaretonbofa, J.R.G. Evans, J Porous Mater. 9 (2002) 257.

[28] Y.S. Choi, S.R. Hong, Y.M. Lee, K.W. Song, Y.S. Nam, T.G. Park, J. Biomed. Mater. Res. 48 (1999) 631.

[29] S. Deville, E. Saiz, A. Tomsia, Biomater. 27 (2006) 5480.

[30] C. Wu, J. Chang, W. Zhai, S. Ni, J. Wang, J. Biomed. Mater. Res. B 78 (2006) 47.

[31] K. Schwartzwalder, H. Somers, A. V. Somers, (1963) US Patent No. 3090094.

[32] Q.Z. Chen, I.D. Thompson, A.R. Boccaccini, Biomater. 27 (2006) 2414.

[33] O.O. Omatete, M.A. Janney, R. A. Strehlow, Am. Ceram. Soc. Bull. 70 (10) (1991) 1641.

[34] J.R. Jones, L.L. Hench, Curr. Opin. Solid State Mater. Sci. 7 (2003) 301.

[35] P. Sepulveda, F.S. Ortega, M.D.M. Innocentini, V.C. Pandolfelli, J. Am. Ceram. Soc. 83 (12) (2000) 3021.

[36] D.L. Wheeler, M.J. Montfort, S.W. McLoughlin, J. Biomed. Mater. Res. A 55 (2001) 603.

[37] J. Wilson, S.B. Low, J. Appl. Biomater. 3 (1992) 123.

[38] M. Vallet-Regi, C.V. Ragel, A.J. Salinas, Eur. J. Inorg. Chem. (2003) 1029.

[39] L.L. Hench, J. Am. Ceram. Soc. 74 (1991) 1487.

[40] T. Kokubo, S. Ito, S. Sakka, T. Yamamuro, J. Mater. Sci. 21 (1986) 536.

[41] A. Salinas, M. Vallet-Regi, Z. Anorg, Allg. Chem. 663 (2007) 1762.

[42] T. Kasuga, Y. Abe, J. Non-Cryst. Solids 243 (1999) 70.

[43] Y. Zhang, J.D. Santos, J. Non-Cryst. Solids 272 (2000) 14.

[44] S. Kumar, P. Vinatier, A. Levasseur, K.J. Rao, J. Solid State Chem. 177 (2004) 1723.

[45] Z. Hong, A. Liu, L. Chen, X. Chen, X. Jing, J Non-Cryst. Solids 355 (2009) 368.

[46] D.B. Joroch, D.C. Clupper, J Biomed. Mater. Res. 82A (2007) 575.

[47] J. Roman, S. Padilla, M. Vallet-Regi, Chem. Mater. 15 (2003) 798.

[48] J. Lao, J.M. Nedelec, Ph. Moretto, E. Jallot, Nuclear Instru. Methods in Phy. Res. B 245 (2006) 511.

[49] M. Vallet-Regi, L. Ruiz-Gonzalez, I. Izquierdo, J.M. Gonzalez-Calbet, J. Mater. Chem. 16 (2006) 26.

[50] Gill, A. Ballesteros, Trends Biotechnol 18 (2000) 282.

[51] H. Tamon, T. Kitamura, M. Okazaki, J. Colloid Interf. Sci. 197 (1998) 353.

[52] S. Yoda, S. Ohshima, F. Ikazaki, J. Non-Cryst. Solids 231 (1998) 41.

[53] Q. Tang, T. Wang, J. Supercritical Fluids, 35 (2005) 91.

[54] F. Shi, L. Wang, J. Liu, Mater. Lett 60 (2006) 3718.

Chapter 2

Literature Review

2.1 Amorphous Silica Derived from Rice Husk Ash

Rice husk ash (RHA) is a cheap source of amorphous silica. It is generated by burning rice husk (RH), an agricultural byproduct. RH is used as a fuel for generation of energy mainly in rice milling plants [1]. A large quantity of RHA is generated as waste material from rice mill. RHA is also generated from industries like brick making, distilleries, furnaces, gasifiers, and power plants, where RH is used as a fuel [2]. Usually, the ash is dumped in the open, which causes air and water pollution by blowing wind. Thus it is a great challenge to dispose off RHA or to utilize it economically for other useful purposes.

RHA contains mainly silica [3] and that silica may be used for a variety of purposes. Silica of the ash may be either amorphous or crystalline or mixture of both, depending on the burning temperature [4, 5]. The ashes obtained after slow combustion of husk at low temperatures contain amorphous silica, whereas ash formed at higher temperatures contains mostly crystalline silica. This crystalline silica comprises mainly cristobalite and tridymite with small proportions of quartz [6]. There are limited uses of crystalline silica as compared to the amorphous silica, because amorphous silica has high surface area and is very reactive due to its nano-particle size. Amorphous silica of RHA has been widely used in vegetable oil refining, pharmaceutical products, detergents, adhesives, chromatograph column packing, and different ceramic compositions [7-9].

Amorphous silica can be prepared by burning the husks in a controlled temperature. According to Hamad et al [10] and Jain et al [11], ash prepared at a temperature of about 500 to 600 ^{o}C, consists of amorphous silica. Cristobalite was formed at 800 ^{o}C. At 1150 ^{o}C, both cristobalite and tridymite were present [10]. However, Nehdi et al [12] stated that silica in RHA can remain in amorphous form at combustion temperatures up to 900 ^{o}C if the combustion time is less than one hour, whereas crystalline silica is produced at 1000 ^{o}C with combustion time greater than 5 min [12]. Chopra et al [13] has reported that for incineration temperatures up to 700 °C the silica was predominantly in amorphous form. Adam et al [14], Kurama et al [15], and Della et al [16] have prepared white silica powder by pyrolyzing the RH in a muffle furnace at 700 ^{o}C for 5 hours.

Completely burnt ash is grey or whitish in colour, while partially burnt ash is blackish [17, 18]. RHA generally contains 90-95% silica, rest being impurities like magnesium, calcium, iron, sodium, potassium, phosphorus, manganese, and zinc; of which the concentration of calcium is highest [16, 6]. The ash containing >99% (w/w) silica can be prepared by acid leaching of husk before burning [6, 19, 20, 21].

Quality of RHA silica depends on the leaching procedure. Real et al [20] found that leaching of rice husks with an acid solution before their combustion would yield silica powder of high specific surface area. However, if the ash is leached with acid, the specific surface area of silica would be poor [20]. Different kind of acids like HCl, H_2SO_4, H_3PO_4 and HNO_3 are used for acid treatment of RH [18, 20, 21, 22, 23]. Liou et al [24] suggested that leaching of husk with HCl is better than that with H_2SO_4, HNO_3 or H_3PO_4.

Several researchers suggested that RHA can be an economically viable raw material for the production of silicates and silica gel [25-28]. The amorphous natures of silica makes it extractable by simple boiling in alkali solution and hence provide a low energy method as an alternative to the current high energy method for the production of silicates using crystalline silica [29]. Silica gel can be prepared by acid neutralization of sodium silicate extracted from RHA [25, 30, 31].

Adam and Chua [32] did the work on the adsorption of palmytic acid on chemically modified RHA. Bonded phase octadecylsilyl (ODS) silica has been prepared by Burns et al [33] using purified RHA, reflux with sodium hydroxide solution followed by precipitation as a gel. The gel was spray dried, further purified by washing with concentrated hydrochloric acid then distilled water prior to vacuum drying and silanization and end-capping. Guha and Roy [34] have prepared silica gel from RHA to use in gas chromatography. They reported that the silica gel prepared from RHA is comparable with commercial silica gel.

2.2 Bioactivity of Silica-based Ceramics

Silica plays an integral role in the bioactivity and osteogenic potential of bioglass, as shown by Hench et al [35]. They suggested that the high density of surface silanol groups (Si-OH) that exist on amorphous silica is the basis for enhanced hydroxyapatite (HAp)

and bone formation in bioglass and related glass ceramic systems. The silanol groups are proposed to be very effective at inducing HAp formation [36].

Hypothesis on physiological silicon research was developed by Hench [37] and Birchall [38]. Silicic acid is essential for the healthy growth of bone and connective tissue. They conclude that the interaction of silicic acid with many metals in vivo produces positive health effects. Mann et al [39] suggested on the bioactivity of amorphous silica. Silica is present in aquatic organisms, the protruding spicules of certain sponges, and the teeth of certain molluscs. These biosilicates are made up of particulate or solid-gel silica with species-specific sizes, shapes, and aggregate arrangements.

` Xynos et al [40] pointed out that, silica based materials provide an additional parameter in the form of biologically active, soluble SiO_2, which is known to affect, e.g., osteoblast activity. Hench et al [41, 42] also suggested that amorphous silica owing to its bioactivity is used in medical devices. Pereira et al [43] reported that silica-gel samples with high volume percentage porosity and pore size > 2 nm are suitable for inducing *in vitro* hydroxycarbonate apatite (HCA) formation in simulated body solutions.

Kortesuo et al [44] pointed out that amorphous silica is biocompatible and degradable in living tissue, as well as in corresponding simulated physiological conditions. Kros et al [45] studied the toxicity of silica over silica based hybrid material. They proved that sol-gel silica coating material is biocompatible and non-toxic, and the response of cells such as osteoblasts to silica gels was quite good as studied by Anderson et al [46]. Several authors suggested that silica nanoparticles are biocompatible and degrade over time in the body [47–49].

The biocompatibility of silica precursor was monitored by Gill and Ballesteros [50]. It was also shown by Meyer et al [51] that tetraalkoxysilanes can be successfully exchanged for tetrakis (2-hydroxyethyl) orthosilicate (THEOS). Several researchers like Radin et al [49], Santos et al [52], and Avnir et al [53] suggested that silica xerogel prepared from alkoxysilane can be coated on titanium at room temperature, especially for cardiovascular therapeutic applications. The silica xerogel system is an attractive material to apply to metallic substrates, because sol-gel derived silica xerogels are known to have

excellent bioactivity and exhibit chemical bonding to the surrounding tissues, particularly bone.

Gallardo et al [54] reported that, porous silica gels obtained from TEOS and polyacrylic acid (PAA) was bioactive *in vitro*. Nieto et al [55] studied the cell viability in a wet silica gel, made from TEOS and found that the cells can stay alive within the gel. Klein et al [56] also studied on bone bonding ability of silica gel with respect to the synthesis temperature of the gel and shown that the lower temperature treatment at 400 and 600°C allowed the silica gels to be degraded easily, while gels treated at 800 and 1000°C were more stable.

Many researchers suggested that sol-gel derived silicas are potential biomaterials and they have been studied both for tissue regeneration and drug delivery applications. They are used either in a pure SiO_2 gel form or in the form of composites [57-61]. Kortesuo et al [44] observed that, no changes in liver, kidney, uterus or lymph nodes related to silica xerogel, even though the applied amount of silica xerogel was high.

Recently, some reviews reported on sol-gel silica and hybrid biomaterials and the processes of biosilicification [62-64]. Novel synthetic approaches, allowing the immobilization of enzymes, living cells, antibodies, immune molecules, polysaccharides, phospholipids, nucleic acids, proteins and other biomolecules in the sol-gel matrices, have been proposed. Kros et al [45] studied prospects of silica based hybrid materials for glucose sensor. This hybrid material was found to be non-toxic and also slows down the growth of fibroblasts on its surface, which is important since a thick capsule could inhibit the diffusion of glucose to an implanted glucose sensor [65, 66].

Many researchers including Hench et al [67] and Sepulveda et al [68] studied the dissolution features of glass and glass-ceramics in SBF medium. Silica is a bio-degradable material as stated by Carlisle [69] and proved by other researchers. Xie et al [70] studied the dissolution characteristics of bioactive titanium-particle-containing dicalcium silicate coating in tris-hydroxy methyl amino methane (TRIS) buffered solution.

Dissolution study of porous poly (DL-lactide-co-glycolide) (PLGA)/bioactive glass composite was carried out in TRIS medium by Orva et al [71]. Similar dissolution

features of zinc-containing bioactive glasses in TRIS medium was also studied by Aina et al [72].

2.3 Bioactive Silica-based Ceramics by Powder Compaction Method

Powder pressing technique is the conventional ceramic manufacturing process commonly used to produce "green" bodies prior to final sintering. In this process ceramic powders are compacted using die and punch to give different shapes.

Silica based bioceramics have also been prepared by this conventional powder compaction method by several researchers. Lin et al [73] studied the biocompatibility of $CaSiO_3$ ceramics. $CaSiO_3$ powder was uniaxially compacted and sintered in air. The sintered $CaSiO_3$ ceramics showed excellent biocompatibility.

Ni et al [74] studied the preparation and characterization of forsterite (Mg_2SiO_4) bioceramics. Forsterite powder was uniaxially pressed and sintered at different temperatures. The *in vitro* study showed the significant osteoblasts adhesion, spreading and growing on the surface of forsterite ceramic.

Wu et al [75] prepared bredigite ($Ca_7MgSi_4O_{16}$) ceramics by uniaxial pressing of the bredigite powders at 10 MPa followed by isostatic pressing at 200 MPa. The compact specimens were sintered at 1350 ^oC for 8 h. The apatite formation was observed within 7-days immersion in SBF upon the bredigite ceramics. The cell proliferation was also very good on the surface of this kind of silica based biomaterials.

Agathopoulos et al [76] studied bioactivity of a new silica based bioceramic, by characterizing it through *in vitro* assessment. They used glass powder and compacted by uniaxial pressing. Compacted discs were sintered at several temperatures between 650 to 920 ^oC. Glass-ceramics sintered at 800 ^oC showed better mechanical property and bioactivity.

Similarly, Liu et al. studied the bioactivity, biodegradability and mechanical strength of silica-based bioglass-ceramics. The bioglass powder was pressed and sintered at 500, 800, 1000, and 1200 ^oC, respectively. At 1000 ^oC, the ceramic material showed maximum density. The formation of hydroxyl-carbonate apatite layer on the surface of 7-days SBF incubated specimen confirmed its bioactivity [77].

Many researchers also studied the synthesis, mechanical property and bioactivity of nanocrystalline apatite [78], hydroxyapatite [79], hydroxyapatite-CaO and hydroxyapatite-CaO-bioactive glass [80], calcium-phosphate [81], β-TCP [82], calcium carbonate [83] etc. using powder pressing technique.

2.4 Bioactive Silica-based Scaffold Prepared by Polymer Sponge Replication Technique

The sponge replication method is a very popular method of producing ceramic foams owing to its simplicity and efficiency. The method was patented in 1963 by Schwartzwalder and Somers [84]. The method involves the use of a polymeric template, usually polyurethane (PU) foam, which is immersed in slurry that infiltrates the porous structure of the template by repetition of compression/release processes. Excess slurry is squeezed out from the polymeric template, to obtain a homogeneous coating on the foam struts and the foam is allowed to dry either at ambient temperature for 12 hours [85] or at elevated temperatures of approximately 80 °C for about 10 minutes [86].

The dried body is heat treated to burn out the polymer template and sintered at higher temperatures to obtain dense structures. The result is a three-dimensional open-cell foam structure of high porosity and interconnectivity. The structure is known as reticulated porous ceramic (RPC). Using the sponge replication technique it is possible to obtain RPC of high porosity (~90%), pore size of >400-500 μm and pore interconnectivity [84].

Han et al [87, 88] investigated the preparation of porous silica composite using the reticulate method. They studied the effect of sintering temperature and addition of SiO_2 on the strength of the porous body. The strength of the porous body decreased at the temperature at which cristobalite phase appeared. On adding 30 wt.% of SiO_2, the composite porous body achieved maximum compressive strength and on further addition of silica content, the strength was decreased. At 1360 ^oC sintering temperature and 30 wt.% of SiO_2 addition, the silica composites were able to obtain up to 80% porous and interconnected structures. These composites were also deduced that the compressive strength of porous body has an exponential reduction with porosity.

Wen et al [89], also prepared porous silica composites by choosing different sponge templates and the relationship between pore size, porosity and mechanical strength of the sintered products were investigated. It is important to burn out the polymer template slowly, using an appropriate heating rate, in order to minimize the damage (e.g. formation of microcracks) to the ceramic coating [90].

Kim et al [91] used this reticulate method to fabricate a scaffold-coating system using poly (α-caprolactone) (PCL) polymer and HA hybrid, that are be used in hard tissue regeneration. This was an attempt to improve the mechanical properties of scaffolds and to enhance wound healing by incorporating vancomycin, which is an antibiotic. Callcut and Knowles [92] used glass reinforced slurry to fabricate scaffolds and the foams were coated twice. A significant enhancement of both the scaffold density and mechanical properties was observed and there seemed to be no degradation of the macrostructure by using the poly urethane (PU) template. Zhu et al [93], improved the mechanical strength of porous body by vacuum degassing the slurry, which was used for impregnation.

Jones et al [94] studied the bioactivity and mechanical property of silica-based glass-ceramic scaffold. The scaffolds were sintered at 600, 700, 800 and 1000 ^{o}C. As sintering temperatures were increased, compressive strength increased from 0.34 to 2.26 MPa. Bioactivity of this scaffold decreased on increasing the temperature from 600 to 1000 ^{o}C, however, apatite formation was observed within 3-days incubation in SBF for all glass-ceramic specimens.

Ramay and Zhang [95] introduced a method of producing scaffolds by combining the gel-casting and the replication method. This was an attempt to overcome the disadvantages and to develop a method to combine the advantages of both methods. It was possible to obtain a pore size range of 200-400 μm of interconnected porosity and the elastic modulus obtained was comparable to that of cortical bone. These features were more favorable for bone tissue engineering applications than the structures produced only by gel-casting.

2.5 Bioactive Silica-based Ceramics Prepared by Gelcasting Method

Gelcasting is considered to be one of the most versatile routes for producing foam structures of complex shapes and good mechanical properties. This method involves

preparing homogeneous slurry that consists of the ceramic powder, water, dispersing agents and a monomer solution. Into this slurry, initiators and catalysts are added to promote polymerization at the time of gelling. The gelled body with a rubbery texture is dried, machined and then fired to remove the polymer [96, 97].

Gelcasting method has also been used to produce silica based porous body for different applications. Xueman [98] studied the rheological properties of aqueous silicon slurry used for gelcasting. They concluded that, rheology of silicon slurries would be influenced by solid concentration, concentration of dispersant and high-speed dispersing time.

Yiechen et al [99], studied the preparation of gelcasted body using fused silica of 60 wt.% in the slurry. By using this technique, silica based ceramics were able to withstand 40 MPa of bending strength on addition of nano meter silica dopant.

Zhang et al [100], prepared porous silica-based gelcasted body, where pores were developed by purging N_2 into the silica slurry of 68 wt.% solid loading. The porous body contained ~73.5 % porosity with pores size of 90 to 340 μm.

Li et al had studied the change of shrinkage rate with porosity of porous silica ceramics, which was prepared by gelcasting technique [101]. Padilla et al studied the bioactivity and biocompatibility of gel-casted porous bodies with different shapes prepared by using HA/sol-gel glass mixtures [102]. These materials showed *in vitro* bioactive behavior in simulated body fluid; additionally, the proliferation and spreading assays with osteoblastic cells (HOS) showed that the materials are biocompatible.

2.6 Bioglass-Ceramics

In the 1970's, Hench et al [103] reported the bioactive material, Bioglass. It was then realized that the special properties of this kind of ceramic material could be exploited to provide better materials for biomedical applications. The field has since expanded enormously. Bioglass® 45S5, was a four-component silica glass (45 wt.% SiO_2, 24.5 wt.% CaO, 24.5 wt.% Na_2O and 6 wt.% P_2O_5). The low silica content and the presence of sodium ions in the glass result in very rapid ion exchange with the proton and hydronium ions of physiological solutions. The ion exchange creates alkalinity at the implant

interface with the body fluid leading to the nucleation and crystallization of a carbonate apatite layer that is equivalent chemically and structurally to the biological bone mineral [104].

Hench et al [105] had studied the melt-derived bioactive glasses, i.e. ternary system of Na_2O-CaO-SiO_2 glasses, which was highly reactive and showed good bioactivity when exposed to an aqueous medium of SBF.

Kokubo [106] had discussed the bioactivity of glass-ceramics (GC) on the basis of their surface chemistry. The observed result shows that apatite phase present in the GC does not play an important role in forming the chemical bond to bone. However, Ca-P rich layer formed on the surface of the GC in the body environment plays the essential role in forming the chemical bond between the glass-ceramic and bone.

Ohtsuki et al [107] had reported an intimate contact between living tissues and Ceravital glasses. Vogel and Holan [108] developed the Bioverit family of melt-derived GC. They found that its ability to form the apatite layer in GC decreased with increasing MgO content.

Roman et al [109] had studied the bioactivity of melt-derived CaO-SiO_2-P_2O_5-MgO-CaF_2 GC, which was chemically treated with HCl for different time period through *in vitro* studies. Verne et al [110] studied the bioactivity of different sets of melt-derived glasses and GC belonging to the CaO-SiO_2-P_2O_5-MgO-K_2O-Na_2O system. Both glass and GC showed bioactivity after the pretreatment in SBF.

Agathopoulos et al [76] studied the bioactivity of a new silica based bioceramic, SiO_2-Al_2O_3-B_2O_3-MgO-CaO-Na_2O-F GC, by characterizing it through *in vitro* assessment. Glass was prepared by conventional melting procedure. The glass powder was compacted by uniaxial pressing and compacted disks were sintered at several temperatures between 650 to 920 ^oC. GC sintered at 800 ^oC showed better mechanical property and bioactivity. Submicron precipitates, enriched in Ca and P (found by EDS), were uniformly formed on the surface of glass-ceramics after 7 days of immersion in SBF.

Itala et al [111] had studied the property of porous bioactive glasses, which were immersed in SBF for several hours. In this study, it was revealed that sintering temperature also affects the formation of crystalline hydroxyapatite layer on the specimen after immersion in SBF for 20-24 hours.

In the early 1990s, sol-gel processing was introduced for the synthesis of bioactive glasses [112]. The sol-gel route allows glasses of higher purity and homogeneity to be obtained at temperatures notably lower than those required to obtain glasses by the melting method. These bioactive glasses, converted into bioactive glass-ceramics (BGC) have higher bioactivity and resorbability *in vitro*, which have application as bone graft material [113].

Various research groups used the sol-gel route for the preparation of BGC in the ternary SiO_2-CaO-P_2O_5, quaternary SiO_2-CaO-P_2O_5-Mg systems and the binary SiO_2-CaO system for biomedical applications. *In vitro* studies have shown that nucleation and crystallization rates of HCA depend on many factors including the sol-gel glass composition.

Xia and Chang [114] prepared nano BGC using the sol-gel technique. In this study, they prepared nano bioactive-glass powders. The size of the bioactive glass particles were controlled in the range of 20-40 nm by controlling the concentration of the ammonia solution in the alkali-mediated sol-gel process.

Li et al [115] studied the bioactivity of sol-gel derived quaternary bioglass system between SiO_2, CaO, P_2O_5 and Na_2O, formed apatite layers in a TRIS buffer solution. Lao et al [116] prepared gel-glass powders containing 75wt.% SiO_2, 25wt.% CaO using the sol-gel process. The reason for choosing a glass in the SiO_2-CaO binary system was due to the expected higher homogeneity in the glass. Furthermore, the study of the Ca-P layer growth process was easier since the phosphate ions were only coming from the solution.

Balamurugan et al [117] studied the *in vitro* bioactivity and biocompatibility of sol-gel derived glass composed of SiO_2-CaO-P_2O_5-ZnO. Incorporation of Zn into the bioglass system does not diminish the bioactivity of bioglass. Addition of Zn is beneficial for cell attachment and for maintaining the pH of SBF within the physiological limit by forming zinc hydroxide in the SBF solution.

SiO_2-CaO-P_2O_5 BGC nanoparticles were prepared by Hong et al [118], via the combination of sol-gel and coprecipitation processes. BGC nanoparticles with 30-100 nm in diameter were obtained. After 3-days soaking in SBF solution, the BGC nanoparticles could rapidly induce the carbonated hydroxyapatite from solution.

Bioactivity of GC is fully dependent upon the sintering temperature or crystallization temperature of the material. On increasing the sintering temperature, bioactivity and bio-dissolvability of the specimen decreased, although, mechanical properties of the specimen effectively increased [119]. Similar observation was also made by Peitl et al [120] when studying the GC having a chemical composition of $1Na_2O$-$2CaO$-$3SiO_2$ and $1.5Na_2O$-$1.5CaO$-$3SiO_2$, containing different wt.% of P_2O_5.

Similarly, Liu et al [77] studied the bioactivity, biodegradability and mechanical strength of sol-gel derived bioglass coated alumina scaffolds. Their study resulted in bioglass powder with the composition of 58 mol% SiO_2-38 mol% CaO-4 mol% P_2O_5. The bioglass powder was then pressed uniaxially and sintered at 500, 800, 1000, and 1200 ^oC, respectively. It was found that at sintering temperatures above 800 ^oC, the bioactivity and bio degradability of the bioglass started to decrease.

2.7 Silica Aerogel

Aerogels, which are highly porous, low-density materials consisting of nano-sized pores, are of interests for applications as varied as thermal insulation, catalysis, drug delivery, etc [121].

The synthesis of silica aerogel can be divided into three general steps, which are (a) preparation of gel, (b) ageing of gel, and (c) drying of gel. In the first step, colloidal system of liquid character changed into colloidal system of solid character in which the dispersed substance forms a continuous, coherent framework that is interpenetrated by liquid. The gel prepared is aged in its mother solution to strengthen the gel, so that shrinkage during the drying step will be a minimum. In the last step, the gel should be freed of the pore liquid. To prevent the collapse of the gel structure, drying is made to take place under special precaution.

Kistler in 1931 [122] first attempted the preparation of silica aerogel by removing the liquid from a gel by a gas (air). The liquid held inside the gel has greater pressure than its vapour. To transform this liquid into a supercritical fluid (gas), a certain temperature is required which is known as critical temperature. Above that critical temperature the air can be replaced for that supercritical fluid to get a non-collapsed gel structure [123].

During drying under atmospheric conditions, the nanostructured porous layers are exposed to the capillary force and large surface tension, which destroys the microstructure and cause the shrinkage of the gel [124]. Supercritical drying (SCD) method is usually used to solve this problem. In this process, the liquid in a substance is transformed into gas in the absence of surface tension and capillary stress. Thus, no damage occurs to the material's delicate nanostructured pore network. However, the SCD is relatively an expensive process due to its high-pressure operating condition. For this reason there is a great interest in subcritical or ambient pressure drying.

Ambient-pressure method for silica aerogel includes both surface modification and network strengthening of sol-gel derived silica wet gel. To prepare silica gel, silicon alkoxides like, tetramethoxysilane (TMOS) tetraethoxysilane (TEOS), methyltriethoxysilane (MTES) and polyethoxydisiloxane (PEDS) are mainly used [125-128]. In Ambient-pressure method, the water-alcohol mixture in the pores of the gel is first exchanged for a water-free solvent. Then, reaction with silylating agent takes place so that Si-OH groups are silylated. Silylation is carried out directly in the water phase of the hydrogel, which results in a solvent exchange as well as a phase separation of the gel water and the solvent. The replacement of H from the Si-OH groups by the hydrolytically stable Si-R groups through the oxygen bond prevents the adsorption of water and hence results in the hydrophobic aerogels [129].

Washing in H_2O/ethanol (EtOH) increases the liquid permeability of the solid part of the gel by a dissolution reprecipitation process for silica. Aging in a siloxane solution increases the stiffness and strength of the alcogel by adding new monomers to the silica network as stated by Kirkbir et al [130]. Einarsrud et al [131] removed the pore water through exchanging EtOH and *n*-heptane.

All the silicon alkoxides materials are not only expensive but also hazardous and can cause blindness (with TMOS). To avoid the cost of raw materials, Schwertfeger et al [124] used water glass as a cheaper silica source. Waterglass (or sodium silicate) solution was used for low-cost aerogel production by Kistler [132] using super critical drying method. Water glass based aerogel was also prepared by Schwertfeger [124], Tyler [133], Rao [134] and others using SCD method. Einarsrud et al [128] investigated properties of aerogels synthesized by different precursors and reported that waterglass, produced aerogel with the highest degree of monolithicity because these gels had the highest stiffness and the largest pore size.

In the case of water glass based aerogel, the sol preparation is quite different. The sol in this case is silicic acid (H_2SiO_3) which is produced by exchanging Na^+ ions of water glass with H^+. To remove sodium ions in the water glass, the dilute sodium silicate is passed through ion-exchange column filled with strong acidic cation resin such as sulphonated polystyrene. Adopting this ion exchanging technique, Lee et al [135] and Hwang et al [136] have prepared silica aerogel. But, Sarawade et al [137] had removed the sodium portion from the silica aerogel beads by washing with distilled water for 12 h. Silica aerogel was prepared in this study by ambient pressure drying method using sodium silicate as silica precursor.

Wang and Tang [138, 139] prepared silica aerogel from RHA by sol-gel process followed by supercritical drying. A new process for preparing silica aerogel was proposed. RHA, which is not only cheap but also rich in silica, was used as the silicon source. Li and Wang [140] prepared the aerogel through sol-gel process using RHA; a small quantity of TEOS was used as the modifier, and added into the hydro-sol. Then the aerogel was prepared by drying the gel at atmospheric pressure.

Several authors have suggested that silica aerogel is a promising biocompatible scaffold for the immobilization of biological material for a variety of applications [141] and as matrices in the design of biosensors [142-144].

Fernandez et al [145] studied the preparation and bioactivity of wollastonite/aerogels composites obtained from a TEOS-MTES matrix through the sol-

gel process. Bioactivity of this aerogel was studied by immersing it in SBF for 25 days. A spherical apatite layer covered the entire surface of the aerogel.

Li et al [146] prepared protein encapsulated silica aerogel to form bioaerogel via the sol-gel polymerization of TEOS with an ionic liquid as the solvent and pore-forming agent and the solvent extraction process. The final gel was dried through Freeze-drying process. It was found that the DsRed protein was quite stable in this aerogel.

2.8 Summary and Scope of Work

From this brief survey, it may be concluded that amorphous silica of RHA can be used for different novel applications. This amorphous silica has a promising future as a bio-material because it originates from biomass.

Literature survey shows that silica-based materials are frequently used for different bio-applications due to their good bioactivity and bio-degradability characteristics. Silica-based bioceramics are mainly prepared from silicon alkoxides. However, there is no report on the preparation of silica-based bioceramics using RHA and/or silica gel derived from RHA.

From the literature survey it has been found that silica-based ceramics which are being used for different bio-applications are made by conventional pressing technique. For that reason, amorphous silica derived from RHA should be investigated for its bioactivity on the specimen fabricated through conventional pressing method, because this method is very simple and quick.

Literature survey shows that silica-based reticulated porous ceramics are also fabricated through sponge replication technique. Most of the ceramics are silicate glass, glass-ceramics and fused silica ceramics. However, there is no report on preparation of pure amorphous silica-based scaffolds by replication technique. Similarly, silica-based porous ceramics have also been fabricated by gelcasting technique. But, there is no report on gelcasting of pure amorphous silica-based porous ceramics.

From the literature survey it has been found that sol-gel derived silica-based bioglass-ceramics are better than melt driven one. All the silica-based bioceramics are mainly prepared by using silicon alkoxides as silica precursors. However, there is no

report on preparation of silica-based bioglass-ceramics by sol-gel technique using RHA as silica precursors.

It has been found that ambient pressure dried silica aerogel is much more cost effective than supercritical dried aerogel. Also, silica aerogel has been prepared mainly by using silicon alkoxides as silica precursors. There is no report on preparation of bioactive silica aerogel through ambient pressure drying process using RHA as the silica precursor.

2.9 Objectives of Present Work

The aim of the present study is the utilization of amorphous silica from rice husk ash for bio-active ceramic preparation with the following objectives:

(a) Preparation and characterization of amorphous silica derived from rice husk and silica gel derived from husk ash.

(b) Preparation and characterization of silica-based bioactive ceramics by conventional pressing method.

(c) Fabrication and characterization of silica-based reticulated porous scaffold using polymeric sponge replication technique.

(d) Fabrication and characterization of silica-based bioactive porous ceramics using gelcasting technique.

(e) Sol-gel synthesis of bioglass-ceramics using rice husk ash as a source for silica and its characterization.

(f) Preparation of bioactive silica aerogel through ambient pressure drying using husk ash as silica source.

References

[1] F. Bondioli, F. Andreola, L. Barbieri, T. Manfredini, A.M. Ferrari, J. Eur. Ceram. Soci. 27 (2007) 3483.

[2] A. Sharma, T.R. Rao, Bioresource Technology 67 (1999) 53.

[3] M. Andreoli, G.T. Luca, E.S. Miyamaru Seo, Materials Letters 44 (2000) 294.

[4] Bronzeoak Ltd., 3 MWe Rice Husk Power plants in Indonesia: A Feasibility Study. Internal Report, 2001.

[5] The UK Steel Association (www.uksteel.org).

[6] T-Z Liou, Mater. Sci. Eng. A 364 (2004) 313.

[7] C.J. Brinker, G.W. Scherer, Applications. In: Sol–Gel Science, The Physics and Chemistry of Sol–Gel Processing. Academic Press, Inc., San Diego, CA, (1990).

[8] R.K. Iler, Silica gels and powders. In: Iler, R.K. (Ed.), The Chemistry of Silica. John Wiley and Sons, New York, NY, (1979).

[9] A. Proctor, P.K. Clark, C.A. Parker, J. AOCS 72 (1995) 459.

[10] M.A. Hamad, I.A. Khattab, Thermochim. Acta 48 (1981) 343.

[11] A. Jain, T.R. Rao, S.S. Sambi, P.D. Grover, Biomass and Bioenergy 7 (1995) 285.

[12] M. Nehdi, J. Duquette, A. El Damatty, Cement and Concrete Res. 33 (2003) 1203.

[13] S.K. Chopra, S.C. Ahluwalia, S. Laxmi, ESCAP/RCTT 3rd Workshop on Rice Husk Ash Cements, New Delhi, 1981.

[14] F. Adam, K. Kandasamy, S. Balakrishnan, J Colloid and Int. Sci. 304 (2006) 137.

[15] S. Kurama, H. Kurama, Ceram. Int. 34 (2) (2008) 269.

[16] V.P. Della, I. Kuhn, D. Hotza, Mater. Letters 57 (2002) 818.

[17] P.K. Metha, In Proc. UNIDO/ESCAP/RCTT Workshop on RHA, Cement, Prshuwur. Pukistun, 1979.

[18] M.A. Rahman, The Internatlonal Journal of Cement Composites and Lightweight Concrete, 9 (2) 1987.

[19] J. James, M.S. Rao, Thermochim. Acta 97 (1986) 329.

[20] C. Real, M.D. Alcala, J.M. Criado, J. Am. Ceram. Soc. 79 (8) (1996) 2012.

[21] K. Kandasamy, S. Balakrishnan, J. Colloid Inter. Sci. 304 (2006) 137.

[22] A. Chakraverty, P. Mishra, H.D. Banerjee, J. Mater. Sci. 23 (1988) 21.

[23] H. Halimaton, N.M.M. Mohd, E. Salasiah, L. Endang, R. Zainab, J. Non-Cryst. Solids 211 (1997) 126.

[24] T-H Liou, F-W Chang, J-J Lo, Ind. Eng. Chem. Res. 36 (1997) 568.

[25] U. Kalapathy, A. Proctor, J. Shultz, Bioresour. Technol. 85 (2002) 285.

[26] R.V. Krishnaro, M.M. Godkhindi, Ceram. Int. 18 (1992) 243.

[27] P.W. Lender, R. Ruiter, Inorganic and Metal-Containing Polymeric Materials. Plenum Press, New York, (1990).

[28] T.C. Luan, T.C. Chou, Ind. Eng. Chem. Res. 29 (1990) 1922.

[29] D.D. Bui, Rice husk ash a mineral admixture for high performance concrete, Civil Engineering and Geosciences, Ph.D. Thesis, Delft University of Technology, Delft, 2001.

[30] U. Kalapathy, A. Proctor, J. Schultz, Biores. Technol. 73 (2000a) 257.

[31] S.R. Kamath, A. Proctor, Cereal Chem. 75 (1998) 484.

[32] F. Adam, J.H. Chua, J. Colloid and Inter. Sci. 280 (2004) 55.

[33] D.T. Burns, K. Tungkananurak, D. Jadsadapattarakul, Microchim. Acta 154 (2006) 81.

[34] O.K. Guha, J. Roy, J. Chromatography. 437 (1988) 244.

[35] L.L. Hench, H.A. Paschall, J. Biomed. Mater. Res. 7 (1973) 25.

[36] P. Li, C. Ohtsuli, T. Kokubo, N. Soga, N. Nakamura, T. Yamamuro, J. Am. Ceram. Soc. 75 (1992) 2094.

[37] L.L. Hench, Chem. Ind. 14 (1995) 547.

[38] J.D. Birchall, Chem. Sot. Rev. 24 (1995) 351.

[39] S. Mann, Biomimetic Materials Chemistry, New York, (1996).

[40] I.D. Xynos, A.J. Edgar, L.D.K. Buttery, L.L. Hench, J.M. Polak, J. Biomed. Mater. Res. 55 (2001) 151.

[41] L.L. Hench, J.M. Polak, Science 295 (2002) 1014.

[42] L.L. Hench, J. Am. Ceram. Soc. 74 (1991) 1487.

[43] M. Pereira, A. Clark, L.L. Hench, J. Am. Ceram. Soc. 78 (1995) 2463.

[44] P. Kortesuo, M. Ahola, S. Karlson, I. Kangasniemi, A. Yli-Urpo, J. Kiesvaara, Biomaterials 21 (2000) 193.

[45] A. Kros, M. Gerritse, V.S.I. Sprakel, N.A.J.M. Sommerdijk, J.A. Jansen, R.J.M. Nolte, Sensors Actuators B 81 (2001) 68.

[46] S.I. Anderson, S. Downes, C.C. Perry, A.M. Caballero, J. Mater. Sci-Mater. Med. 9 (1998) 731.

[47] C. Barbe, J. Bartlett, L.G. Kong, K. Finnie, H.Q. Lin, M. Larkin, et al. Adv. Mater. 16 (2004) 1959.

[48] A. Roy, T.Y. Ohulchanskyy, H.E. Pudavar, E.J. Bergey, A.R. Oseroff, J. Morgan, et al. J. Am. Chem. Soc. 125 (2003) 7860.

[49] S. Radin, G. El-Bassyouni, E.J. Vresilovic, E. Schepers, P. Ducheyne, Biomaterials 26 (2005) 1043.

[50] I. Gill, A. Ballesteros, J. Am. Chem. Soc. 120 (1998) 8587.

[51] M. Meyer, A. Fischer, H. Hoffmann, J. Phys. Chem. B 106 (2002) 1528.

[52] E.M. Santos, S. Radin, B.J. Shenker, I.M. Shapiro, P. Ducheyne, J. Biomed. Mater. Res. 41 (1998) 87.

[53] D. Avnir, T. Coradin, O. Lev, J. Livage, J. Mater. Chem. 16 (2006) 1013.

[54] G. Janet, G. Pablo, J.M. Galliano, P. Lopez, Biomaterials 23 (2002) 4277.

[55] A. nieto, S. Areva, T. Wilson, R. Viitala, M. Vallet-Regi, Acta Biomater. 5 (2009) 3478.

[56] C.P.A.T. Klein, P. Li, J.M.A. de Blieck-Hogervorstt, K. de Groot, Biomaterials 16 (1995) 715.

[57] M. Vallet-Regi, A. Ramila, R.P. Del Real, J. Perez-Pariente, Chem. Mater. 13 (2001) 308.

[58] M. Vallet-Regi, F. Balas, M. Colilla, M. Manzano, Solid State Sci. 9 (2007) 768.

[59] T. Peltola, M. Jokinen, S. Veittola, J. Simola, A. Yli-Urpo, J. Biomed. Mater. Res. 54 (2001) 579.

[60] M. Vallet-Regi, F. Balas, D. Arcos, Angew Chem Int Ed 46 (2007) 7548.

[61] D. Arcos, I. Izquierdo-Barba, M. Vallet-Regi, J. Mater. Sci-Mater. Medicine 20 (2009) 447.

[62] C. Sanchez, B. Julian, P. Belleville, M. Popall, J. Mater. Chem. 15 (2005) 3559.

[63] C. Sanchez, H. Ariribart, M.M.G. Guille, Nat. Mater. 4 (2005) 277.

[64] D. Avnir, T. Coradin, O. Lev, J. Livage, J. Mater. Chem. 16 (2006) 1013.

[65] S.P. Hudson, R.F. Pradera, R. Langer, D.S. Kohane, Biomaterials 29 (2008) 4045.

[66] T. Nash, A.C. Allison, J.S. Harington, Nature 210 (1966) 259.

[67] L.L. Hench, R.J. Splinter, W.C. Allen, T.K. Greeenlee, J. Biomed. Mater. Res. 2 (1971) 117.

[68] P. Sepulveda, J. R. Jones, L. L. Hench, J. Biomed. Mater. Res. 61 (2) (2002) 301.

[69] E.M. Carlisle, Science 167 (1970) 279.

[70] Y. Xie, X. Liu, P.K. Chu, X. Zheng, C. Ding, Surface & Coatings Techno 200 (2005) 1950.

[71] E. Orava, J. Korventausta, M. Rosenberg, M. Jokinen, A. Rosling, Polymer Degradation and Stability 92 (2007) 14.

[72] V. Aina, G. Malavasi, A. Fiorio Pla, L. Munaron, C. Morterra, Acta Biomater. 5 (2009) 1211.

[73] K. Lin, W. Zhai, S. Ni, J. Chang, Y. Zeng, W. Qian, Ceram. Intl. 31 (2005) 323.

[74] S. Ni, L. Chou, J. Chang, Ceram. Intl. 33 (2007) 83.

[75] C. Wu, J. Chang, J. Wang, S. Ni, W. Zhai, Biomaterials 26 (2005) 2925.

[76] S. Agathopoulos, D. U. Tulyaganov, P. Valerio, J.M.F. Ferreira, Biomaterials 26 (2005) 2255.

[77] J. Liu, X. Miao, Ceram. Intl. 30 (2004) 1781.

[78] C. Drouet, F. Bosc, M. Banu, C. Largeot, C. Combes, G. Dechambre, C. Estournes, G. Raimbeaux, C. Rey, Powder Technol. 190 (2009) 118.

[79] M. Trecant-Viana, T. Le Neel, C. Canto-Nicolazo, E. Champion, M. Leroy, G. Daculsi, J. Phys. 7 (1997).

[80] E. Hatzistavrou, X. Chatzistavrou, L. Papadopoulou, N. Kantiranis, E. Kontonasaki, A.R. Boccaccini, K.M. Paraskevopoulos, Mater. Sc. Eng. C 30 (2010) 497.

[81] C. Balazsi, F. Weber, Z. Kover , E. Horvath, C. Nemeth, J. Euro. Ceram. Soc. 27 (2007) 1601.

[82] K. Lin, J. Chang, J. Lu, W. Wu, Y. Zeng, Ceram. Intl. 33 (2007) 979.

[83] A. Lucas-Girot, P. Langlois, J.C. Sangleboeuf, A. Ouammou, T. Rouxel, J. Gaude, Biomaterials 23 (2002) 503.

[84] K. Schwartzwalder, H. Somers, A. V. Somers, US Patent No. 3090094 (1963).

[85] Q.Z. Chen, A.R. Boccaccini, H.B. Zhang, D.Z. Wang, M.J. Edirisinghe, J.Am. Ceram. Soc. 89 (2006a) 1534.

[86] H.W. Kim, H.E. Kim, J. C. Knowles, J Biomedical Mater Res B-Appl. Biomater. 70 (2004a) 270.

[87] Y.S. Han, J.B. Li, B. Chi, Z.H. Wen, J. Porous Mater. 10 (2003) 41.

[88] Y.S. Han, J.B. Li, Q.M. Wei, Z.H. Wen, Mater. Letters 57 (2003) 3847.

[89] Z.H. Wen, Y.S. Han, L. Liang, J.B. Li, Mater. Char. 59(9) (2008) 1335.

[90] H.W. Kim, H.E. Kim, J.C. Knowles, J. Biomed Mater Res-Appl. Biomater. 70B (2004a) 270.

[91] H.W. Kim, J.C. Knowles, H.E. Kim, J. Mater. Sci-Mater. Medicine 16 (2005b) 189.

[92] S. Callcut, J.C. Knowles, J. Mater. Sci-Mater. Medicine 13 (2002) 485.

[93] X. Zhu, D. Jiang, S. Tan, Mater. Letters 51 (2001) 363.

[94] J.R. Jones, L.M. Ehrenfried, L.L. Hench, Biomaterials 27 (2006) 964.

[95] H.R. Ramay, M.Q. Zhang, Biomaterials, 24, (2003) 3293.

[96] P. Sepulveda, Am. Ceram. Soc. Bul. 76 (1997) 61.

[97] S. Dhara, M. Pradhan, D. Ghosh, P. Bhargava, Adv. Appl. Ceram. 104 (2005) 9.

[98] P. Xueman, X. Mingxia, L. Hui, L. Xiaolei, J. Huiming, Colloids and Surf. A 317 (2008) 136.

[99] H. Yichen, W. Zhongjian, L. Jianying, J. Non-Cryst. Solids 354 (2008) 1285.

[100] F-Z Zhang, T. Kato, M. Fuji, M. Takahashi, J. Eur. Ceram. Soc. 26 (2006) 667.

[101] S. Li, H. Du, D. Yang, J.G.D. Song, G. Li, Key Engg. Mater. 434-435 (2010) 79.

[102] S. Padilla, S. Sanchez-Salcedo, M. Vallet-Regi, J. Biomed. Mater. Res. A 75(1) (2005) 63.

[103] L.L. Hench, O. Anderson, Wilson J (Eds.), An introduction to bioceramics. World Scientific, Singapore (1993).

[104] L.L. Hench, J. Am. Ceram. Soc. 74 (1991) 1487.

[105] L.L. Hench, R.J. Spinter, W.C. Allen, T.K. Greenlee, J. Biomed Mater.Res.2 (1971) 117.

[106] T. Kokubo, J. Non-Cryst. Solids 138 (1990) 120.

[107] C. Ohtsuki, H. Kushitani, T. Kokubo, S. Kotani, T. Yamamuro, J. Biomed. Mater. Res. 25 (1991) 1363.

[108] W. Vogel, W. Holan, J. Non-Cryst. Solids (1990) 1223.

[109] J. Roman, A.J. Salinas, M. Vallet-Regi, J.M. Oliveira, R.N. Correia, M.H. Fernandes, Biomaterials 22 (2001) 2013.

[110] E. Verne, O. Bretcanu, C. Balagna, C.L. Bianchi, M. Cannas, S. Gatti, C. Vitale-Brovarone, J. Mater. Sci: Mater. Medicine 20 (2009) 75.

[111] A. Itala, H.O. Ylaneen, J. Yrjans, T. Heono, T. Hentunen, M. Hupa, H. T. Aro, J. Biomed. Mater. Res. 62 (2002) 404.

[112] R. Li, A.E. Clark, L.L. Hench, J. Appl. Biomaterials 2 (1991) 231.

[113] D.B. Joroch, D.C. Clupper, J Biomed. Mater. Res. 82A (2007) 575.

[114] W. Xia, J. Chang, Mater. Letters 61 (2007) 3251.

[115] R. Li, A.E. Clark, L.L. Hench, in Transactions of 16th Annual Meeting of the Societey for Biomaterials (Charleston SC, May 20-23, 1990), Vol. XII. Society for Biomaterials, Algonquin, IL, 40 (1990).

[116] J. Lao, J.M. Nedelec, P. Moretto, E. Jallot, N.I.M. in Phy Res B 245 (2006) 511.

[117] A. Balamurugan, G. Balossier, S. Kannan, J. Michel, A.H.S. Rebelo, J.M.F. Ferreira, Acta Biomater. 3 (2007) 255.

[118] Z. Hong, A. Liu, L. Chen, X. Chen, X. Jing, J. Non-Cryst. Solids 355 (2009) 368.

[119] L.L. Hench, O. Peital, G.L. Torre, E.D. Zanotto, Bioactive ceramics and Method of preparing., USPTO: US Patent 5981412 (1997).

[120] O. Peital, E.D. Zanotto, L.L. Hench, J. Non-Cryst solids, 292 (2001) 115.

[121] G.W. Scherer, Adv. Colloid Interf. Sci. 76–77 (1998) 321.

[122] S.S Kistler, Nature 127 (1931) 741.

[123] S. Frohnhoff, R.A. Fischer, T. Heinrich, Thin Solid Films 255 (1995) 115.

[124] F. Schwertfeger, D. Frank, M. Schmidt, J. Non-Cryst. Solids. 225 (1998) 24.

[125] J.H. Harreld, T. Ebina, G. Stucky, J. Non-Cryst. Solids 298 (2002) 241.

[126] L.A. Colon, Y. Guo, A. Fermier, Anal. Chem. 68 (1996) 2753.

[127] N. Ishizuka, H. Minakuchi, K. Nakanishi, N. Soga, K. Hosoya, N. Tanaka, Anal. Chem. 72 (2000) 1275.

[128] M-A. Einarsrud, E. Nilsen, A. Rigacci, G.M. Pajonk, D. Valette, M. Durant, B. Chevalier, P. Nitz, F. Ehrburger-Dolle, J. Non-Cryst. Solids 285 (2001) 1.

[129] F. Schuth, K.S.W. Sing, J. Weitkamp, (Eds.), Hand Book of Porous Solids, 3 (2002) 2014.

[130] F. Kirkbir, H. Murata, D. Meyers, S. Ray Chaudhuri, J. Non-Cryst. Solids 225 (1998) 14.

[131] M-A. Einarsrud, J. Non-Cryst. Solids 225 (1998) 1.

[132] S.S. Kistler, J. Phys. Chem. 36 (1932) 52.

[133] L.J. Tyler, Dow Corning, GB 682574, (1959).

[134] A.V. Rao, A.P. Rao, M.M. Kulkarni, J. Non-Cryst. Solids 350 (2004a) 224.

[135] C.J. Lee, G.S. Kim, S.H. Hyun, J. Mater. Sci. 37 (2002) 2237.

[136] S-W. Hwang, H.H. Jung, S.H. Hyun, Y.S. Ahn, J. Sol-Gel Sci. Technol. 41 (2007) 139.

[137] P.B. Sarawade, J-K Kim, A. Hilonga, H.T. Kim, Solid State Sci. 12 (2010) 911.

[138] T.Wang, Q. Tang, CN Patent 1449997A (2003).

[139] Q. Tang, T.Wang, J. Supercrit. Fluids 35 (2005) 91.

[140] T. Li, T. Wang, Mater. Chem. Phy. 112 (2008) 308.

[141] M. Power, B. Hosticka, E. Black, C. Daitch, P. Norris, J. Non-Cryst Solids 285 (2001) 303.

[142] X. Chen, G.S. Wilson, Langmuir 20 (2004) 8762.

[143] J.M. Wallace, J.K. Rice, J.J. Pietron, R.M. Stroud, J.W. Long, D.R. Rolison, Nano Lett. 3 (2003) 1463.

[144] Anon, Science 302 (2003) 199.

[145] J.A. Toledo-Fernandez, R. Mendoza-Serna, V. Morales, N.de la Rosa-Fox, M. Pinero, A. Santos, L. Esquivias, J Mater Sci: Mater. Medicine 19 (2008) 2207.

[146] Y.K. Li, M.J. Chou, T-Y Wu, T-R Jinn, Y.W. Chen-Yang, Acta Biomater. 4 (2008) 725.

Chapter 3

Experimental Details

3.1 Preparation of Amorphous Silica Precursor

3.1.1 Preparation of Rice Husk Ash Silica

Rice husk (RH) was collected from a local rice mill. Unwanted fine dust materials were removed through air-blowing separation technique and then washed properly to remove the physically adhered impurities using tap water. After successive washing, RH was dried in an air-circulated oven at 100 ± 2 ^{o}C for 12 h to get clean and dry RH.

The cleaned RH was burned at 700 ^{o}C for 6 h in air to get the rice husk ash (RHA). The ash was brownish in colour and termed brown ash (BA). To get impurity free ash, cleaned husk was acid leached using 3 N HCl (Merck, India) solutions under boiling condition for 1 h followed by thorough washing with warm distilled water to remove acid. The husk was then dried and burned following same procedure stated above for BA. The ash thus obtained was whitish in color and designated as WA. Fig. 3.1 shows the flow diagram of preparation of BA and WA.

3.1.2 Characterization of Ash Silica

3.1.2.1 Chemical Analysis

Elemental content of RH, BA and WA was determined by X-ray fluorescence (XRF, Horiba MESA 500W). XRF spectroscopy is widely used for the qualitative and quantitative elemental analysis of samples. XRF has the advantage of generally being non-destructive, multi-elemental detection, fast analysis, and cost effective. The main disadvantage is that analyses are generally restricted to elements heavier than fluorine.

The principle of X-ray fluorescence is as follows; the sample excited by X-rays emits a short wavelength radiation (fluorescence), characteristic of each alloying element. A parallel beam of the secondary radiation is directed, by means of a collimator, onto the analyzing crystal, it is separated according to wavelengths and then reflected into a radiation detector mounted on a high precision goniometer. The angular position of crystal and goniometer is a function of the wavelength and allows the identification of the element in the matrix.

Since XRF technique determines the surface elemental content of particles, samples were finely ground to minimize the possible effect of non-uniform distribution of

elements of the material. Ground samples were dried at 130 ^{o}C for 2 h and stored under nitrogen. Samples were loaded into the vacuum sampling chamber of the XRF and analyzed after the vacuum reached < 0.01 Torr. This precaution was taken to minimize contribution from residual moisture of the samples and oxygen of the environment.

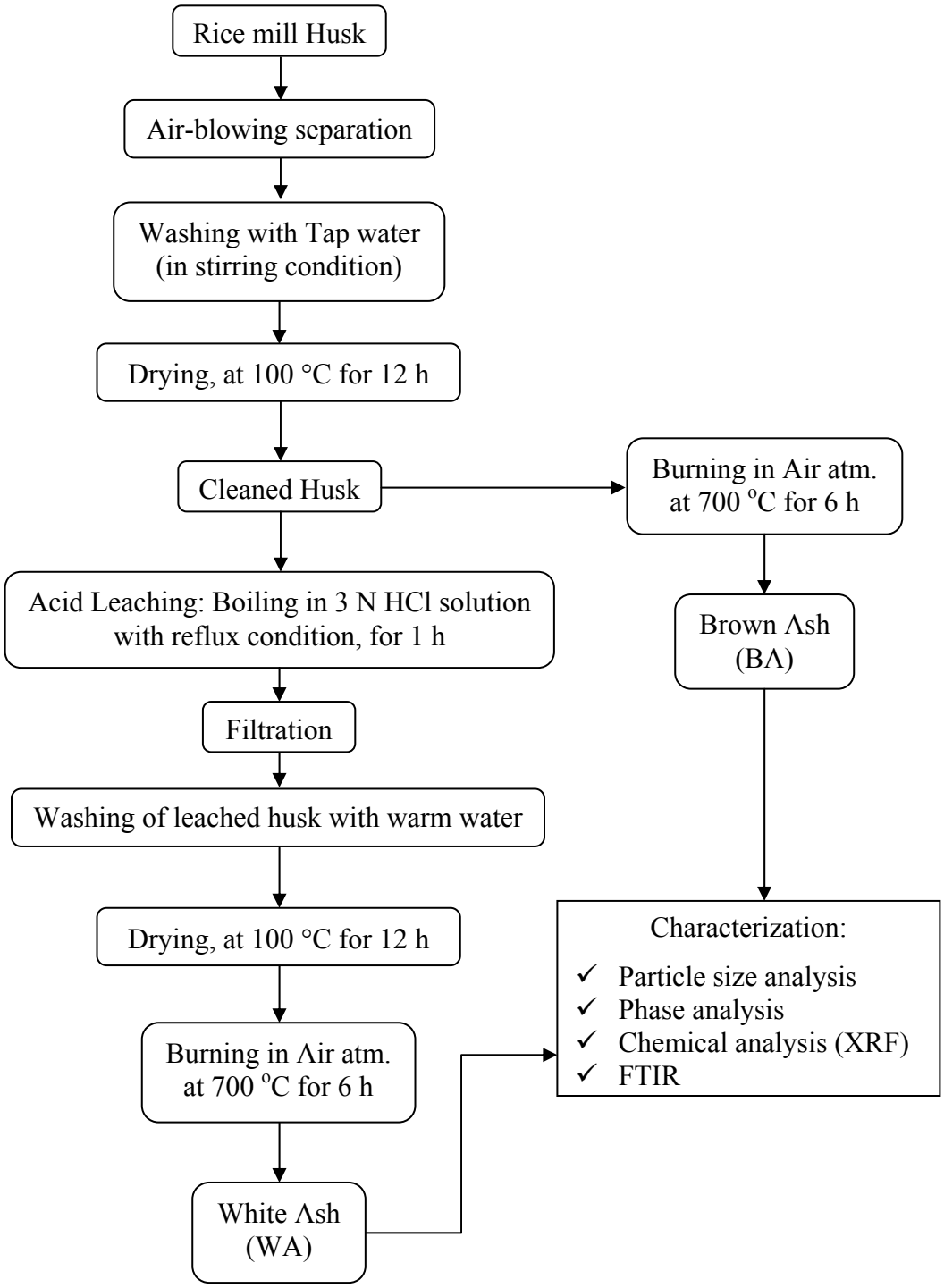

Fig. 3.1 Flow diagram for the preparation of BA and WA silica precursors.

3.1.2.2 Phase Analysis

BA and WA powders were analyzed for their phase content by X-ray powder diffraction performed with a Philip's Diffractometer (model: PW-1830, Philips, Netherlands). Powder sample is packed on a sample stage so that it can be irradiated by the X-ray. To detect the diffracted X-rays, an electronic detector is placed on the other side of the sample from the X-ray tube, and rotated through different Bragg's angles. The goniometer keeps track of the angle (θ), and the detector records the detected X-rays in units of counts/sec and sends this information to the computer. The operating parameters were; 40kV and 35mA with the Cu target, a step size of 0.02 (degree) with continuous scanning. X-ray intensity (counts/sec) was plotted against the angle two-theta (2θ). The angle (2θ) for each diffraction peak was then converted to d-spacing, using the Bragg equation. The identification of different phases was carried out by Hanawalt method using Philips X-pert high score software.

3.1.2.3 Fourier Transformed Infrared (FTIR) Analysis

FTIR spectroscopy was used to characterize the chemical functional groups present in BA and WA, based on the characteristics of vibrational and rotational energies of different molecular bonds in the materials. Fourier transformation is a mathematical operation used to translate a complex curve into its component curves. In a FTIR instrument, the complex curve is an interferogram, or the sum of the constructive and destructive interferences generated by overlapping light waves, and the component curves are the infrared spectrum. An interferogram is generated because of the unique optics of FTIR instrument. The key components are a moveable mirror and a beam splitter. The moveable mirror is responsible for the quality of the interferogram, and it is very important to rotate the mirror at constant speed. The beam splitter, a piece of semi-reflective material, splits the IR beam 50/50 to the fixed and moveable mirrors, and then recombines the beams after being reflected at each mirror. The standard infrared spectrum is then calculated from the Fourier transformed interferogram, giving a spectrum in percent transmittance (% T) vs. light frequency (cm^{-1}).

FTIR analyses of BA and WA powder were done at a resolution of 4 cm^{-1} using Spectrum RX-1 instrument (Perkin Elmer) in the wave number range 400 to 4000

cm^{-1}. A small amount of sample (1 wt.%) was thoroughly mixed with ground KBr in an agate mortar and a disc was prepared in vacuum maintaining a pressure of 33 kg/cm^2. The spectrogram of the sample is observed on computer monitor and a graphic representation of the spectra was taken.

3.1.3 Preparation of Silica Gel Precursor

Silica gel (SG) prepared using RHA was used for the preparation of silica ceramics for bio application. BA was used to synthesize SG raw material. BA was added to 1 M NaOH (Merck, India) solution and boiled for 1 h in reflux condition to extract silica from ash. The solution was filtered to separate the residue. The extracted sodium silicate solution was added drop wise into 1 N HCl solution with constant stirring until the solution pH reached 6. Within few minutes the solution turned into gel. The gel was washed thoroughly with distilled water to remove the sodium chloride. Washed gel is called hydro-gel (Fig. 3.2 (a)). The hydro-gel was dried at 150 °C for 12 h to get dried SG (Fig. 3.2 (b)) material. Fig. 3.3 shows the detailed flow diagram of preparation of silica gel (SG).

Fig. 3.2 Silica hydrogel (a) and Dried Silica Gel (b).

3.1.4 Characterization of Silica Gel

3.1.4.1 Chemical, Phase and FTIR Analysis

Chemical composition, phase and different functional groups associated in SG were determined by using XRF, XRD and FTIR respectively. Fundamentals and working principle and procedure of each experiment have been described in section 3.1.2.1, 3.1.2.2 & 3.1.2.3 respectively.

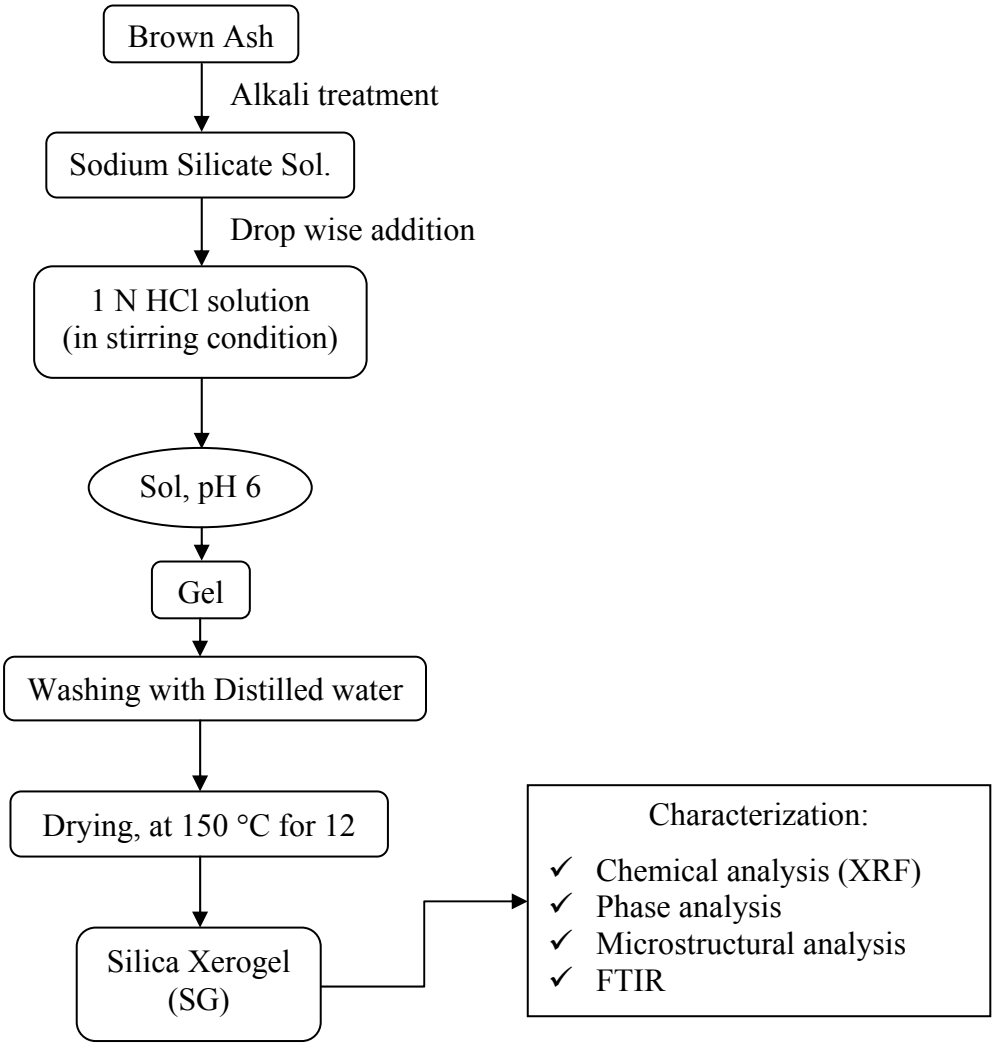

Fig. 3.3 Flow diagram of the preparation of silica gel from BA.

3.1.4.2 Microstructure and EDS Analysis

Microstructure of the SG specimen was analyzed by a Scanning Electron Microscope (SEM, Model: Jeol JSM-6480 LV, Japan). Elemental analysis was done by Energy Dispersive X-ray analysis; (EDAX or EDS, Oxford Instrument, INCA). In SEM, a hot tungsten filament electron gun under vacuum emits electrons which pass through a series of electromagnetic lenses. The sample is then bombarded with a fine beam of electrons having acceleration potentials range from 1-30 KV. A part of the beam is reflected as back scattered electrons (BSE) along with low energy secondary electron emission (SE), cathode luminescence, X-ray excitation and electron transmission also take place. Images

formed from the (SE) beam were studied in the extrinsic mode of SEM. The emitted secondary electrons are detected and displayed on a scanning TV display.

EDS is a technique used for identifying the elemental composition of specimen. The EDS analysis system works as an integrated feature of an electron microscope. During SEM scanning, the specimen is bombarded with an electron beam. The bombarding electrons collide with the electrons of the specimen atoms, knocking some of them off, thus, transferring some of its energy by emitting an X-ray. By measuring the amounts of energy present in the X-rays being released by a specimen, the identity of the atom from which the X-ray is emitted can be established. The output EDS spectrum normally displays peaks corresponding to the energy levels for which the most X-rays had been received. Each of these peaks is unique to an atom, and therefore corresponds to an individual element. The concentration of the element in the specimen is indicated by the high intensity of the peak in a spectrum.

3.2 Silica Ceramics Prepared by Powder Compaction Method

3.2.1 Preparation of Silica Ceramics

Amorphous silica-based ceramics were prepared using three different silica precursors BA, WA and SG. Fig. 3.4 show flow diagram for the preparation and characterization of silica ceramics by powder compaction method. All silica precursors were wet milled thoroughly in pot mill individually for 24 h to get fine powder. Particle size distributions of each powder were measured. The powders were granulated by blending 1 wt.% poly vinyl alcohol (PVA) (M.W. 85,000 Loba, India, LR grade) aqueous solution. The granulated powders were compacted to make pellets using circular die and punch. The weighed amount of powders were taken in a stearic acid lubricated die and punch and uniaxially pressed at 250 MPa pressure for 2 minutes to form cylindrical shapes (pellet) of 15 mm diameter and 3.5 mm thickness. Green densities were calculated from weight/volume ratio. Weight was measured using electronic balance, whereas volume was calculated from the dimension of the specimens.

The pellets were sintered at different sintering temperatures ranging from 700 to 1400 °C. The samples were heated from room temperature to 600 ^{o}C at a rate 2 ^{o}C/min followed by a soaking at 600 ^{o}C for 1 h for binder burnout. Thereafter, the samples were

heated at a rate 3 °C/min to final sintering temperature and sintered for 2 h. Then the specimens were cooled naturally to room temperature within the furnace.

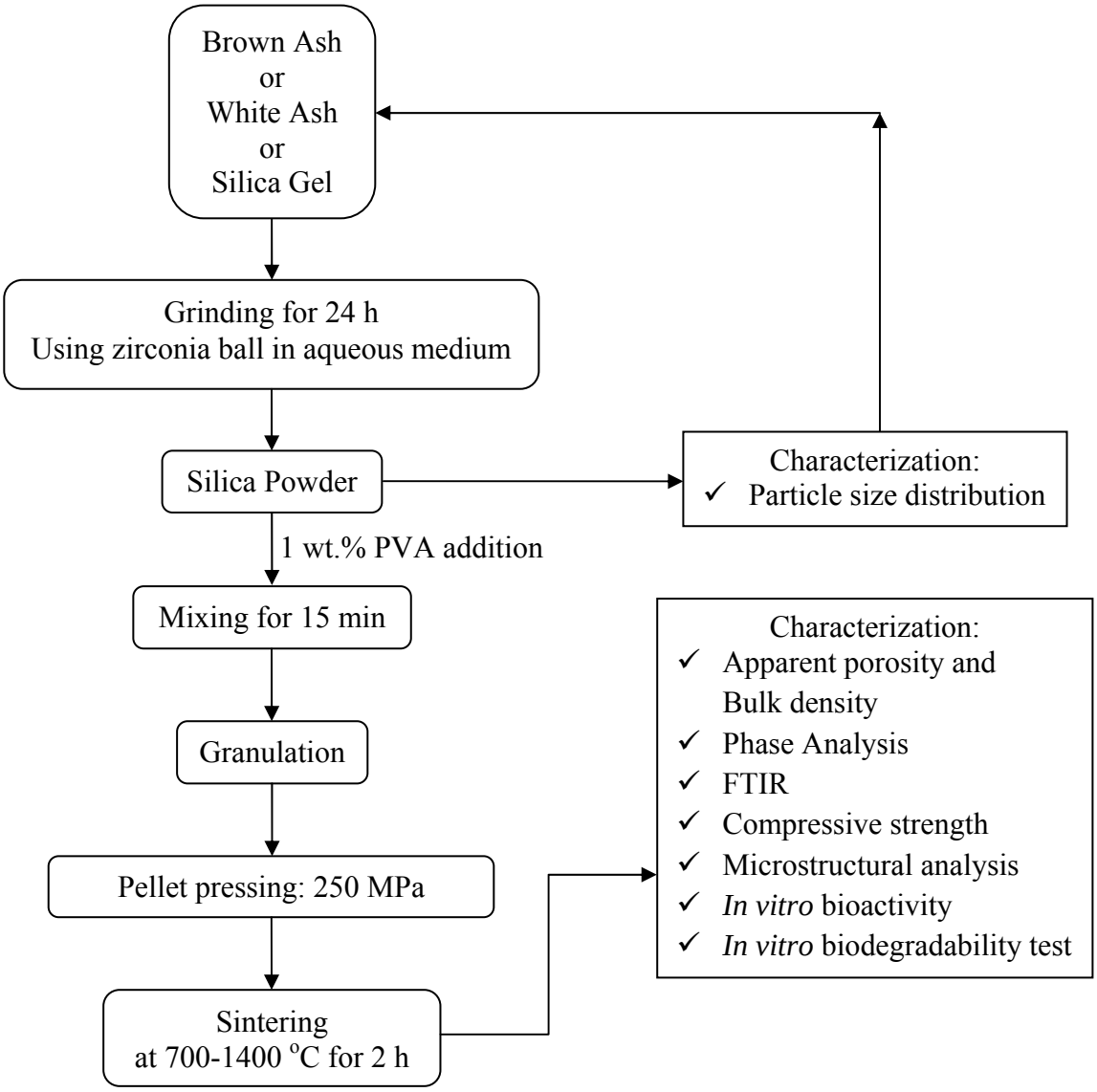

Fig. 3.4 Flow diagram for the preparation of silica-based ceramics by powder compaction method and its characterization.

3.2.2 Characterization of Silica Powders and Ceramics

3.2.2.1 Particle Size Distribution of BA, WA and SG Powders

A laser diffraction method with a multiple scattering technique was used to determine the particle size distribution of the BA, WA and SG powders using computer-controlled

particle size analyzer (Malvern, Mastersizer 2000, UK). The instrument correlates between the intensity and the angle of light scattered from the particle, and the particle size is calculated based on the Miescattering theory.

In order to capture scattered light signals over range of angles, the equipment utilizes a number of high-angle and back-scatter detectors, together with a short wavelength blue LED laser. As the particle size becomes smaller, the scattered light signal shifts to the side and rear with respect to the light source. Shorter wavelength detects the smaller particle size. The scattered light can be measured by a series of photo detectors placed on the opposite side of source at different angles. As the instrument measures clouds of particles rather than individual ones, it is known as an "ensemble" technique, with the advantage that at smaller sizes (e.g. 1 μm), the system measure literally millions of particles which gives some statistical significance to the measured results.

Powdered samples were well dispersed in water using Triton X-100 (Merck, India) as dispersant. A well-dispersed and agglomerate-free suspension was obtained using ultrasonic treatment (Sidilu Ultrasonics, India). The density of the powders was determined by pycnometer using water as medium.

3.2.2.2 Phase Analysis and Rietveld Quantitative Phase Analysis

Different phases of sintered specimen were analyzed by using XRD and functional radical groups were analyzed by FTIR techniques. The details of working principle and method of these techniques have been discussed earlier. For these purpose, the sintered specimens were ground thoroughly to get powders using agate mortar.

A Rietveld refinement procedure was used to analyze quantitative phase content using MAUDWEB [1] (version 2.031) software. The Rietveld method is a powerful technique to extract detailed structural information from powder diffraction data. In contrast to the conventional profile fitting, this method does not use integrated intensities of reflections but employs the entire powder diffraction pattern. In this method, each data point in the digitized intensity versus 2θ curve is an independent observation and during refinement, structure parameters, background parameters, scale factor and profile parameters are varied in a least squares procedure until the simulated pattern matches

well with observed pattern for the proposed structure model [2]. Scale parameters provide the quantitative amount of different phases used in refinement.

The quantity minimized in the least square refinement is the residual S_y [2]:

$$S_y = \frac{\Sigma W_i}{(Y_i - Y_{ci})^2} \tag{3.1}$$

Where, Y_i is observed intensity at the i^{th} Step, and Y_{ic} is calculated intensity at the i^{th} Step and $W_i = 1/Y_i$. Initially, the positions of the peaks were corrected by successive refinements of zero-shift error. Considering the integrated intensity of the peaks as a function of structural parameters only, the Marquardt least-squares procedures were adopted to minimize the difference between the observed and simulated patterns.

Rietveld refinement process will adjust the refineable parameters until the residual (equation 3.2) is minimized with some sense. The users of the Rietveld method have developed several "R_a" values that are now commonly used [2].

$$R_p \text{ ("R}_a\text{" pattern)} = \frac{\sum [Y_i(obs) - Y_i(calc)]}{\sum Y_i(obs)} \tag{3.2}$$

$$R_{wp} \text{ ("R}_a\text{" weighted pattern)} = \left\{ \frac{\sum W_i([Y_i(obs) - Y_i(calc)])^2}{\sum W_i(Y_i(obs))^2} \right\}^{1/2} \tag{3.3}$$

R_{wp} is the most meaningful of these R_a's because the numerator is the residual being minimized. Another useful numerical criterion is the "goodness of fit", G.

$$G = [S_y/(T-P)]^{1/2} \tag{3.4}$$

Where, T is the number of observations (e.g. the number of Y_i's used) and P is the number of parameters adjusted. A G value of 1.3 or less is usually considered to be quite satisfactory. The Rietveld refinement was carried out for BA ceramics for quantitative phase analysis in sintered ceramics.

3.2.2.3 Density and Porosity of Sintered Specimen

Bulk densities and apparent porosities of sintered pellets were measured by "Archimedes" principle. The specimens were weighted in their dry state. Samples were immersed in water and kept under a vacuum of 4 mm of mercury for 12 h to ensure that

water filled up the open pores completely. Then, soaked and suspended weights were measured. The apparent porosity and bulk density were calculated as follows:

Dry weight of the sample = W_d, Soaked weight of the sample = W_s, Suspended weight of the sample = W_a

$$\% \text{ Apparent Porosity} = \frac{W_s - W_d}{W_s - W_a} \times 100 \quad (3.5)$$

$$\text{Bulk Density} = \frac{W_d}{W_s - W_a} \quad (3.6)$$

3.2.2.4 Mechanical Property

The determination of the biaxial flexural strength is frequently necessary as part of the design of structural ceramics to provide information necessary to design an engineering structure. It is the ability of a cylinder, bar or slab to resist failure in compression. The compressive strength is expressed in MPa.

Six samples were taken from each variety (BA, WA and SG) to determine the compressive strength of sintered samples at each test and the average values have been reported. The strength was measured on cylindrical samples in a material testing machine (Hounsfiled H10KT, UK) by Brazilian disc methods. The samples were kept between two compressive fixtures and were broken at a cross head speed of 0.5 mm/min. The strength was calculated from the following formula as per ASTM spec [3]:

$$\sigma_{biaxial\ \ flexural\ \ strength} = \frac{2P}{\pi Dt} \quad (3.7)$$

where, “P” is the breaking load, “D” is the diameter of the pellet and “t” is the thickness of the pellet.

3.2.2.5 *In vitro* Bioactivity

In vitro bioactivity investigation of silica ceramics was carried out by using SBF. SBF was prepared as proposed by Tass [4]. Merck-grade NaCl (99.5%), $NaHCO_3$ (99%), KCl (99.0%), $MgCl_2.6H_2O$ (99%), $Na_2HPO_4.2H_2O$ (99.5%), $CaCl_2.2H_2O$ (99%),Na_2SO_4 (99.5%), TRIS buffer (99.5%) and HCl were used in the preparation of SBF in this study.

SBF was prepared following the Tass [4] protocol. The polyethylene bottle of 1000 mL capacity was cleaned thoroughly with dilute hydrochloric acid solution and then, with de-ionized water. 700 mL of de-ionized water was poured into the bottle, then

placed in a water bath and was kept stirring at a temperature of 36.5 °C, using a magnetic stirrer. Each chemical given in Table 3.1 was added into the water until $MgCl_2.6H_2O$, one by one following the order in the table. After complete dissolution of each reagent, 15 mL of 1 M HCl was added to avoid the turbidity of solution. The reagent $(CH_2OH_3)CNH_2$ was added little by little to avoid local increase in pH of the solution. At this point the pH value was approximately 7.5. The pH of the solution was adjusted to 7.4 by drop-wise addition of 1 M HCl. After the adjustment of pH, de-ionized water was added to the solution adjusting the total volume of the solution to 1000 mL.

Table 3.1 Amounts of reagents for preparation of SBF

Order	Reagent	SBF 1000 mL
#0	De-ionized water	700 mL
#1	NaCl	6.547
#2	$NaHCO_3$	2.268
#3	KCl	0.373
#4	$Na_2HPO_4.2H_2O$	0.178
#5	$MgCl_2.6H_2O$	0.305
#6	1 M HCl	15 mL
#7	$CaCl_2$	0.368
#8	Na_2SO_4	0.071
#9	$(CH_2OH_3)CNH_2$	6.057
#10	1 M HCl	Appropriate amount for adjusting pH

Disc shaped specimens (12.5 mm diameter and 1.5 mm thickness) were placed in 15 mL SBF with its surface vertical. This position allowed both surfaces to interact with SBF and avoided settling of ions on its surface which could be possible in horizontal position. The container (TARSON sterilized circular box) was closed and kept in incubator (BOD, Test master, India) at 37 ^oC. After 7, 14 and 21 days, samples were taken out and soaked in de-ionized water for 5 h and cleaned with caution so that surface is not damaged. Then it was kept in air tight dessicator for drying.

Phases and surface morphologies of SBF incubated silica ceramics were analyzed by using XRD and SEM-EDS respectively.

3.2.2.6 *In vitro* Biodegradability

The dissolution feature of silica ceramics was evaluated in TRIS buffer solution because, TRIS is the plain buffering agent used in most SBF preparations. TRIS solutions do not contain ions and thus represent maximum solubility and minimum reprecipitation activity for a bioactive material [5].

Pure TRIS buffer (99.5%, Merck grade) was dissolved in deionized water with a concentration of 6.1 gm/lit [6]. The solution pH was lowered to 8 using 1 M HCl solution. Analyte was made from fine powder of silica specimen. About 300 mg powders were stirred (60 rpm) in 200 mL TRIS solution at 37 ^{o}C for different time periods. pH of TRIS solution was measured after each soaking interval. Dissolved Si concentration was estimated through molybdenum blue complex absorbance at 820 nm [7] using Perkin Elmer Lambda 35 visible spectrophotometer. The detailed experimental procedure for the spectrophotometric determination of silicon was as follows:

***Preparation of Standard solutions*:**

All the standard solutions were prepared for this purpose according to the protocol of Grimaldi et al [8]. All reagents were of analytical grade (Merck, India) and stored in polyethylene containers prior to use.

(i) 1 N HCl solution.

(ii) Ammonium molybdate standard: 2.0 gm ammonium molybdate [$(NH_4)_6Mo_7O_{24}.4H_2O$] was dissolved in 100 mL water. There was no sign of precipitation.

(iii) Silicate standard: 204.05 mg sodium metasilicate ($Na_2SiO_3.9H_2O$; M.W. 284.216) was dissolved in 100 mL distilled water. Prior to dispensing, the sodium metasilicate was stored over a perchlorate desiccant.

(iv) Stannous Chloride standard: 5 gm of stannous chloride dihydrate was dissolved in 10 mL of hot hydrochloric acid, and diluted to 100 mL with water.

***Preparation of Calibration Chart*:**

Standard calibration line as shown in Fig. 3.5 was plotted for variation of silicon concentration. For this purpose, different concentration of silicate solutions was taken out

from the standard silicate solution, prepared by using sodium metasilicate as silicon source. Whole measurements were made using 40 mm path length cuvette.

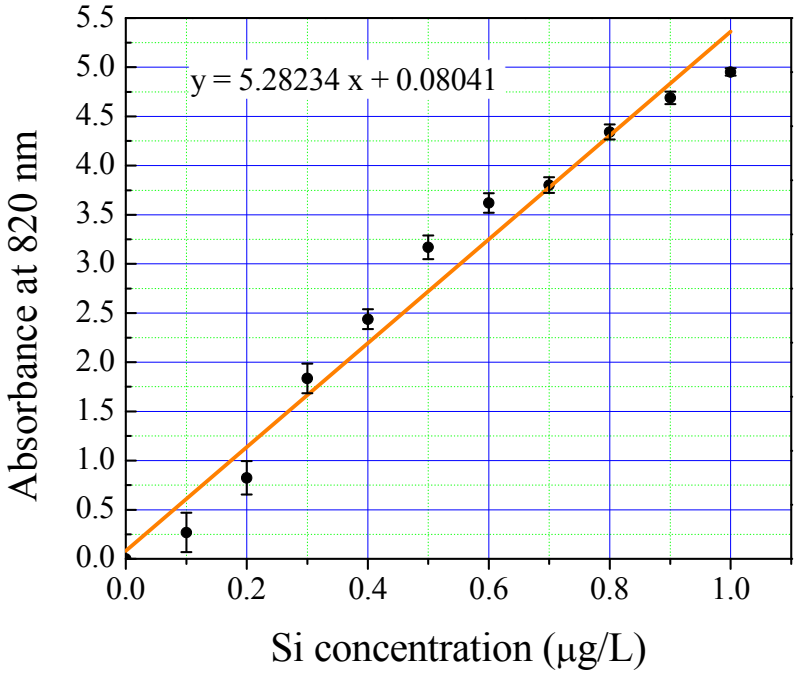

Fig. 3.5 Absorbance at 820 nm as a function of concentration of silicon.

A portion of the analyte was pipetted into a 50 mL separating funnel and the clear analyte collected. 1 mL of clear analyte was transferred to a polyethylene test tube; 0.1 mL concentrated HCl was added followed by 2.0 mL of the molybdate reagent (standard solution). Test sample was allowed to stand for 5 minutes at room temperature, permitting formation of silicomolybdic acid, which imparts a yellow color to the solution. 1 mL of the stannous chloride reductant solution (standard solution) is then added, and the contents of the tubes mixed by swirling, resulting in an intense blue coloration. Then the spectrophotometric determination of Si was performed at 820 nm using UV/VIS spectrophotometer. Baseline correction was done every time following the above procedure by using standard solutions before starting the experiment. The silicon present in the analyte was then determined by comparing results with a standard curve, as shown in Fig. 3.5. Mean value of six experimental data for each formulation were analyzed to determine statistical significance. All the standard solutions were prepared immediately before the start of the experiment.

3.3 Silica-based scaffolds prepared by sponge replication technique

3.3.1 Preparation of Silica Scaffolds

Three types of silica precursors namely BA, WA and SG were used in this work. All precursors were wet milled thoroughly in a pot mill individually for 24 h to get fine powders. Particle size distributions of each were analyzed. The ζ-potentials and sedimentation behaviours of silica particles were evaluated.

For slurry preparation, PVA (5 wt.% aqueous solution) was used as a binder. The 40 wt.% solid loaded slurry was prepared by milling for 15 h. The rheological behavior of the slurry was measured. Then, the slurry was de-aired and impregnated in poly urethane (PU) sponge templates. Impregnated sponge cubes were dried at room temperature. The dried sponges were sintered at different temperatures ranging from 800 to 1400 ^{o}C with a 2 h of dwelling at 550 ^{o}C for burn out of PU foam. The schematic flow diagram for the preparation and characterization of amorphous silica scaffolds is illustrated in Fig. 3.6.

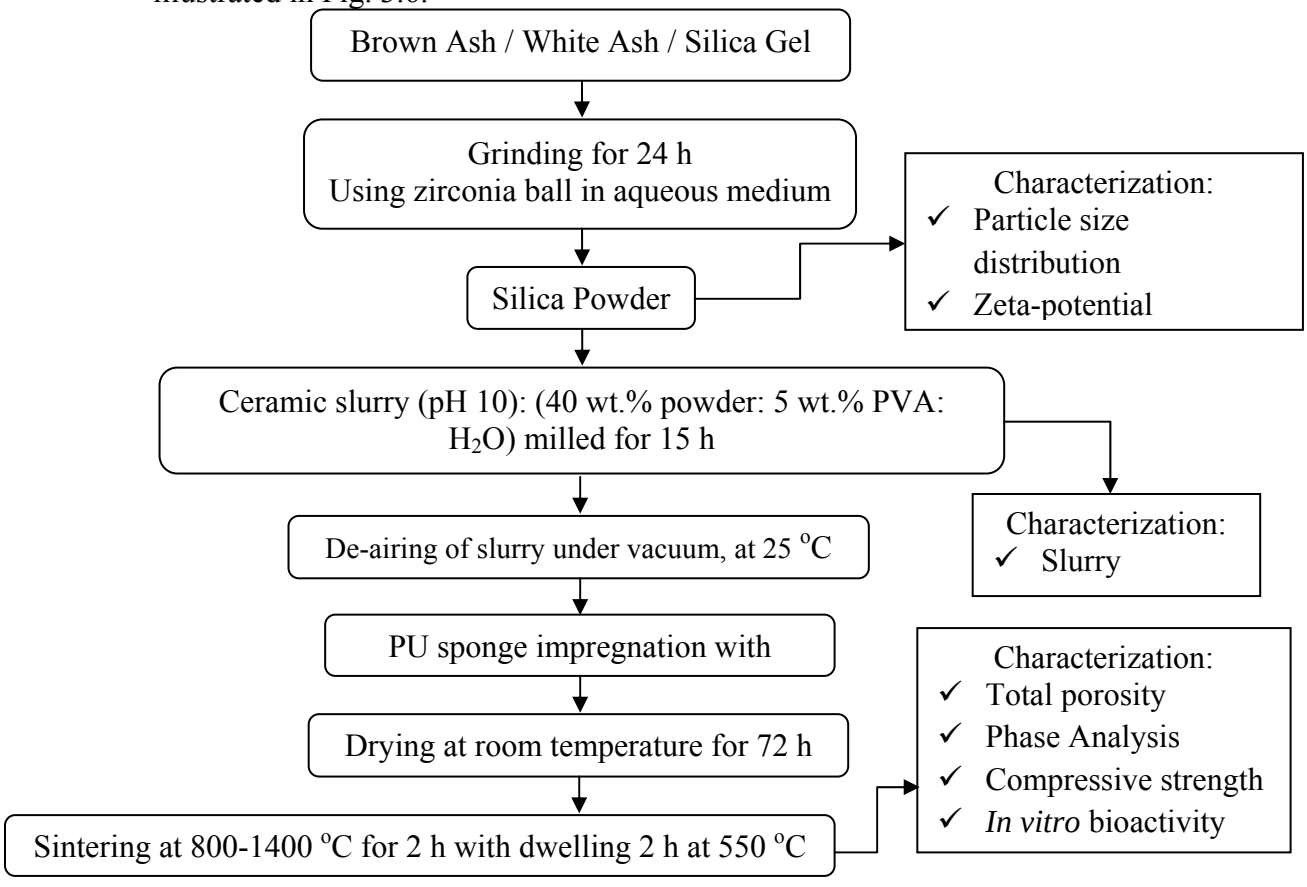

Fig. 3.6 Flow diagram for the preparation of silica scaffolds.

3.3.2 Characterization of Silica powders and Scaffolds

3.3.2.1 Zeta-potential (ζ)

Ceramic particles are generally charged particles due to the presence of surface broken bonds. When a ceramic particle is suspended in liquid, ions of an opposite charge will be attracted to the surface of the particle. The development of a net charge at the particle surface affects the distribution of ions in the surrounding interfacial region, resulting in an increased concentration of counter ions (ions of opposite charge to that of the particle) close to the surface. Thus an "electrical double layer" exists around each particle.

The liquid layer surrounding the particle exists as two parts; an "inner" region, called the "stern layer", where the ions are strongly bound and an outer, diffuse, region where they are less firmly attached. Within the diffuse layer there is a notational boundary inside which the ions and particles form a stable entity. When a particle moves (e.g. due to gravity), ions within the boundary move with it, but any ions beyond the boundary do not travel with the particle. This boundary is called the surface of hydrodynamic shear or "slipping plane". The potential that exists at this boundary is known as the "Zeta-potential". Fig. 3.7 shows the schematic representation of zeta-potential [9].

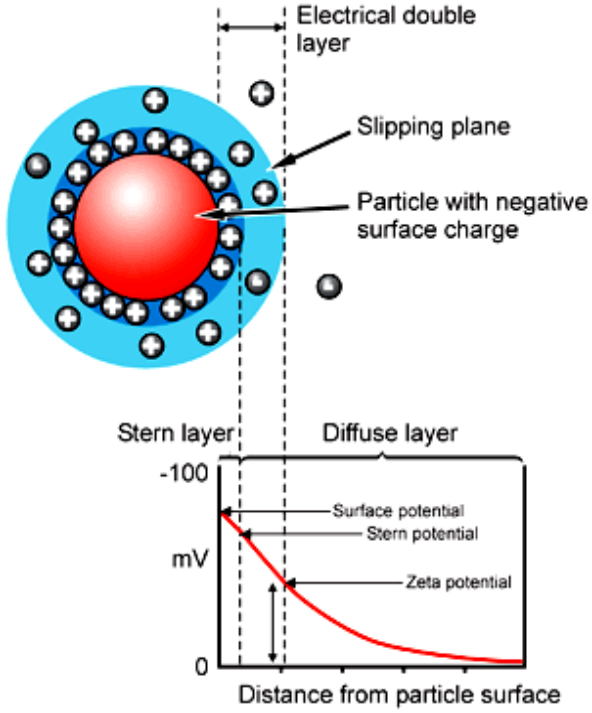

Fig. 3.7 Schematic representation of electrical double layer and zeta-potential [9].

The most important factor that affects zeta-potential is pH. Imagine a particle in suspension with a negative zeta-potential. If more alkali is added to this suspension then the particles will tend to aquire a more negative charge. If acid is then added to this suspension a point will be reached where the negative charge is neutralized. Any further addition of acid can cause a buildup of positive charge. The point where the surface has zero zeta-potential is called the "Isoelectric point". It is normally the point where the colloidal system is least stable.

Zeta potentials of silica precursors were measured using Zetasizer (Model No. 3000 HSA, Malvern, UK) on dilute suspensions of 0.01 gm of silica powder in 100 mL deionized water. The powders were dispersed in deionized water. Then the pH was adjusted to different values ranging from 2 to 12 using HCl or NH_4OH solutions, and then sonicated for 15 minutes. At each pH value, the ζ-potential was measured at least 5 times.

3.3.2.2 Sedimentation Test

The sedimentation behaviour of the 20 wt.% solid loaded silica suspensions was studied at different pH values (2-12). The suspension of each silica powder was prepared by sonicating the powder in aqueous medium for 30 minutes. Immediately after sonication, the suspensions were filled in graduated measuring cylinder with 25 mm inner diameter and 25 cm height. Suspensions were allowed to stand un-disturbed for 24 h. The heights of the interfaces between the clear, turbid and sedimentation section were recorded from the bottom of the cylinder.

3.3.2.3 Slurry Rheology

Rheology is the study of deformation and flow of substances. In other words, rheology is the study of the physical quantities such as yield stress (the minimum force required for a slurry to flow), viscosity (how 'runny' a slurry will be at a given laminar flow-rate), hysteresis (the changes in plastic viscosity and/or yield stress which are due, usually, to particle attrition or settling). The rheological behavior was measured using rheometer (Anton Paar, Physica MCR300, Austria) with a concentric-cylinder with 1.33 mm gap

between the inner and outer cylinder walls. Rheological tests were performed at a shear rate in the range 0-700 s^{-1}, with frequency of 1 Hz and strain amplitude of 1% at 25 ^{o}C.

3.3.2.4 Fabrication of reticulated porous body

Commercial polyurethane sponge with cell size of ≈45 pores per inch was used in this study. Fig. 3.8 (a) and (b) shows the optical and SEM photograph of raw sponge material.

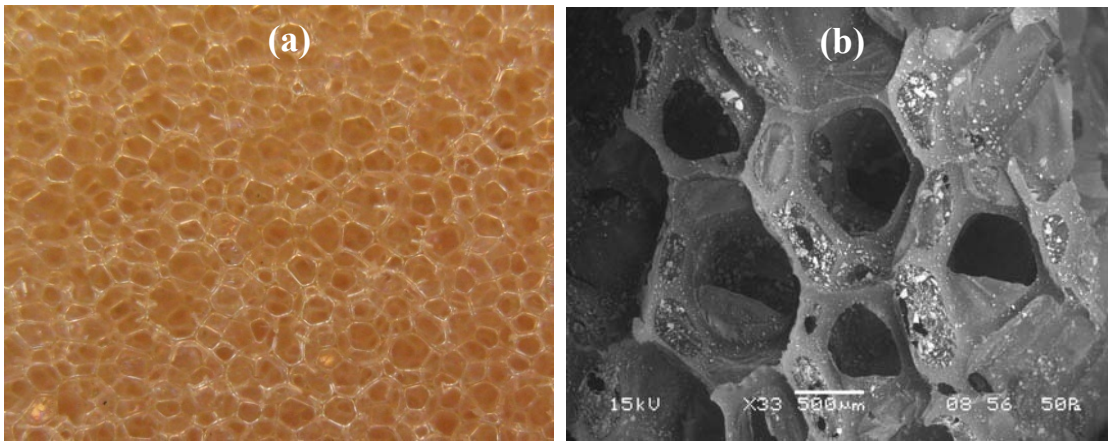

Fig. 3.8 (a) Optical photograph, and (b) SEM of raw sponge.

The sponges for impregnation were cut into ≈25×25×25 mm^3. After the slurry was de-aired, the polyurethane sponges were immersed in it and were compressed while submerged in order to fill all of the pores. After one minute, the impregnated sponge was removed from the slurry and excess slurry squeezed out from the sponge by means of pressing between two parallel plates to a constant gap width. After removal of the excess slurry, the samples were dried at room temperature for 24 h. The samples were then placed in a drying oven at 100 °C for 12 h.

3.3.2.5 Sintering of Reticulated Porous Body

The dried impregnated sponge cubes were sintered at different temperatures ranging from 800 to 1400 ^{o}C with a heating rate of 1 °C min^{-1} from room temperature to 600 °C, followed by holding at 600 ^{o}C for 2 h to burn out the polyurethane support. Subsequently, heating at 2 °C min^{-1} to final temperature and holding for 2 h. The samples were cooled naturally to room temperature within the furnace.

3.3.2.6 Density and Porosity of Sintered Specimen

The porosity of reticulated porous ceramics (RPC) was calculated on the basis of their apparent density (ρ) and true density (ρ_o) according to the following equation:

$$\text{Porosity (\%)} = (1- \rho/\rho_o) \times 100 \quad (3.8)$$

Apparent density was measured from RPC on the basis of their dimensions and weights. True densities of RPC were measured on powder by pycnometric method using water as liquid medium.

W_1= Weight of Empty Bottle; W_2= Weight of (Powder + Bottle)

W_3= Weight of (Powder + Bottle + Fluid); W_4= Weight of (Bottle + Fluid)

$$\text{True density } (\rho_o) = \left\{\left[(W_2 - W_1)\right]/\left[(W_4 - W_1) - (W_3 - W_2)\right]\right\} \times \text{Fluid density} \quad (3.9)$$

3.3.2.7 Mechanical Property

Compressive strength is the ability of a cube or slab to resist failure in compression. Compressive strength of six cubical RPCs from each variety (BA, WA and SG) was measured at each point and the average values have been reported for the point. The measurement was carried out by the material testing machine (Hounsfiled H10KT, UK). The cubes were kept between two compressive fixtures and were broken at a cross head speed of 0.2 mm/min. The strength of RPC body was calculated using following equation;

$$\boldsymbol{\sigma = F/A} \quad (3.10)$$

where, F = the force at each data point and A = area of cross section.

3.3.2.8 *In vitro* Bioactivity

Bioactivity of porous silica ceramics was tested in SBF solution. The details of the experiment have been described in section 3.3.2.5. Porous bodies were incubated in SBF solution for 8 weeks. Nature of phases formed and surface morphologies of SBF incubated scaffold were analyzed by using XRD and SEM-EDS respectively.

3.4 Silica-Based Ceramics Prepared by Gelcasting Method

3.4.1 Preparation of Gelcasted Body

Silica gel (SG) powder was used as silica precursor in this study. SG was prepared utilizing RHA produced by a local rice mill as a waste in boiler heating plant. SG was ground into fine powder and particle size distribution was measured. Zeta potential and sedimentation behaviour of SG powder were measured. Ceramic slurry for gelcasting was prepared by milling solid with monomer and cross-linker solution. Milled slurry was de-aired; initiator and catalyst were added. The final slurry was poured (casted) into a non porous mold. After monomer-cross-linker polymerized, the green bodies were demolded and dried at room temperature with controlled humidity. Finally, the green bodies were preheated at 150 ^{o}C for 6 h and machined into different shapes. The machined bodies were sintered. The schematic flow diagram for the preparation of silica ceramics by gelcasting technique is illustrated in Fig. 3.9.

3.4.2 Characterization Gelcasted Body

3.4.2.1 Slurry Preparation

Homogeneous slurry with good fluidity is required for the gelcasting. Particle size, zeta-potential and sedimentation behaviour of SG powder were measured. Both zeta potential and sedimentation behaviour were measured using suspension in 1:30 premix solution. Premix solution was prepared by using the reactive organic monomer system (15 wt.% of powder basis) of monofunctional acrylamide, $C_2H_3CONH_2$ (AM), difunctional N,N'-methylene-bisacrylamide $(C_2H_3CONH_2)_2CH_2$ (MBAM), and deionized water. SG slurry with 42 vol.% solid loading was prepared by mixing the powder in 1:30 premix solution. Ammonium hydroxide solution was used to maintain the pH at 10. The suspension was milled for 15 h in a plastic bottle with zirconia ball as grinding media to get homogeneous slurry. Fluidity of SG slurry was characterized by analyzing the slurry rheology.

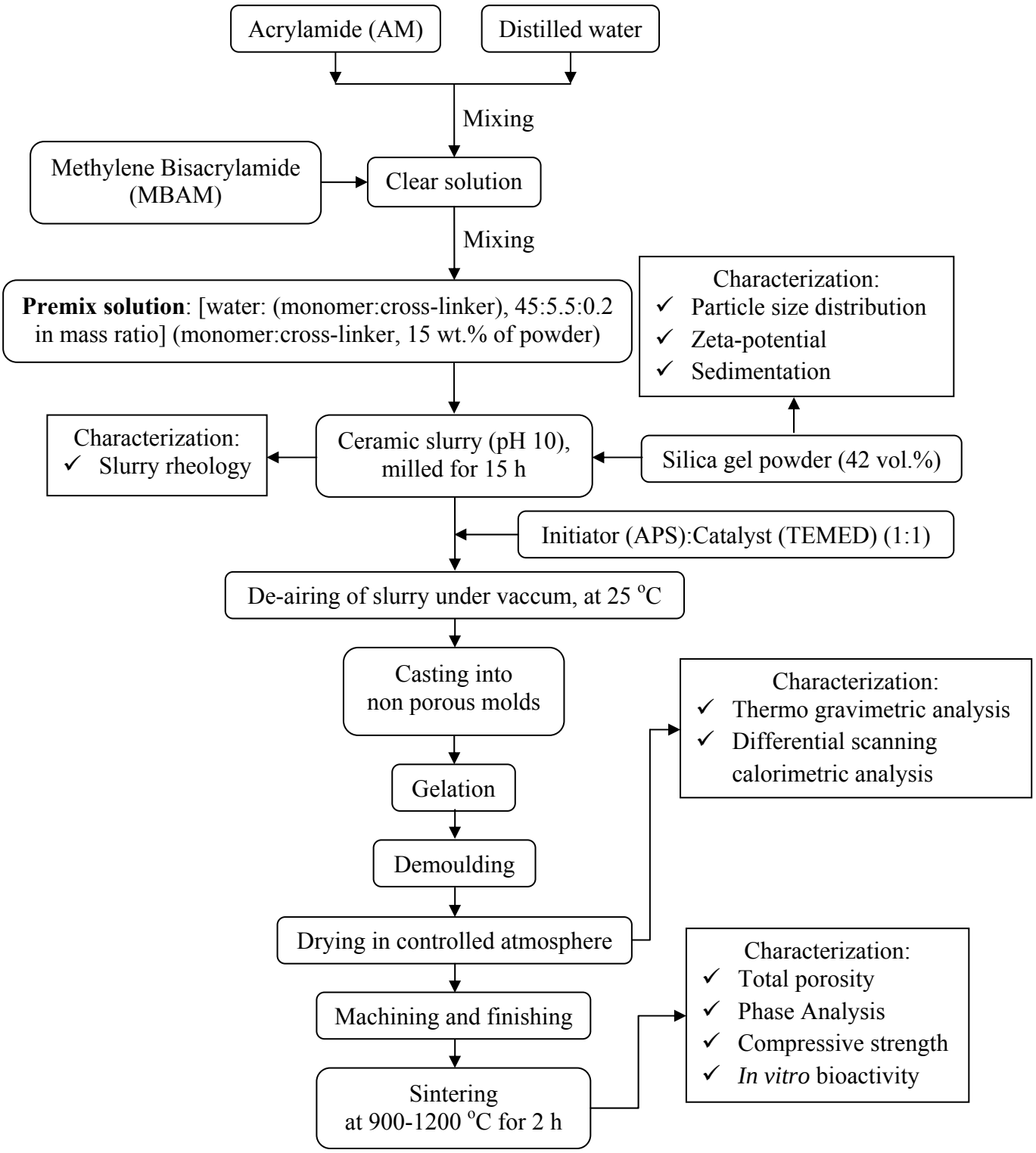

Fig. 3.9 Flow diagram for preparation of silica ceramics using gelcasting techniques.

3.4.2.2 Fabrication of Gelcasted body

Slurry was de-aired and mixed with ammonium persulfate (APS) as initiator and tetramethyl ethylenediamine (TEMED) as catalyst in the ratio of 1:1 (0.15 wt.% on powder basis). Afterwards, the slurry was cast into nonporous mold (PVC pipe and glass beaker). All the above operations were carried out at room temperature and ambient atmosphere. After gelation of slurry, solid bodies were demolded and dried at room temperature (27 ^{o}C) under controlled humidity (75% RH) to avoid cracking and non-uniform shrinkage due to rapid drying. Finally, the green bodies were dried at 110^{o}C for 12 h and machined into pellet like and other different shapes.

Fig. 3.10 shows the gel casted products. Fig. 3.10 (a); (I) is the slurry in a beaker before gelling, (II) demolding of casted body from the beaker, (III) green gel casted body, and (IV) dried cylindrical gelcated body. Similarly, Fig. 3.10 (b) shows rod shaped demolded gel casted body along with PVC pipe used for moulding purpose and cylindrical disk-shaped green bodies machined out from the green rod.

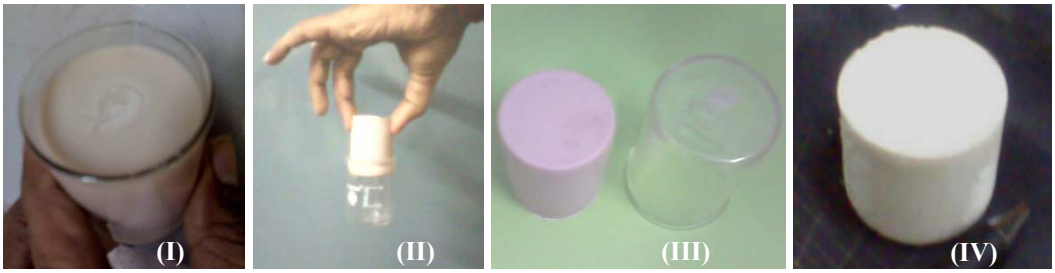

(a)

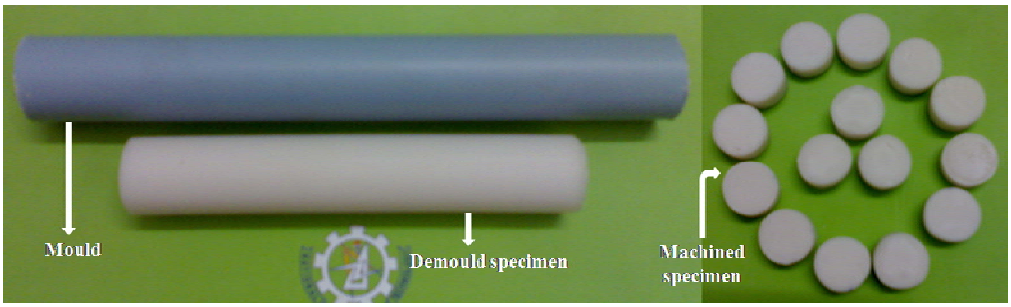

(b)

Fig. 3. 10 (a); (I) is the slurry in a beaker before gelling, (II) demolding of casted body from the beaker, (III) green gel casted body, (IV) dried cylindrical gelcated body, and **(b)** rod shaped demolded gel casted body along with PVC pipe and machined disk-shaped green bodies.

3.4.2.3 Thermal Decomposition Behaviour of Gelcast Body

Thermal decomposition behaviour of green gelcasted body was characterized by thermo gravimetric analysis (TGA) and differential scanning calorimetric analysis (DSC) using NETZSCH STA, Jupitor (Model No 449C), in N_2 atmosphere with the heating rate of 10 ^oC/min.

When a material undergoes physical or chemical change it absorbs or releases thermal energy. The temperature difference of the sample with respect to the reference inert material (α-Al_2O_3) during heating or cooling is plotted in a DSC curve as the deviation from zero base line. Exothermic or endothermic changes are shown in opposite directions of the baseline. TGA is a simple analytical technique that measures the weight loss (or weight gain) of a material as a function of temperature.

3.4.2.4 Sintering and Mechanical Property of Gelcast Body

The green gelcasted bodies were sintered at different temperatures, ranging from 900 to 1200 ^oC with a heating rate of 1 °C min^{-1} from room temperature to 600 °C, followed by a holding at 600 ^oC for 2 h to burn out the organic ingredients. Subsequently, sintering was carried out at final temperature with 2 h holding. The samples were cooled naturally to room temperature within the furnace.

Porosity and bulk density of the sintered gelcasted body (pellets) were calculated by "Archimedes" principle. Compressive strength of sintered gelcasted specimens was measured by the same procedure and calculations as described in section 3.2.2.4 with cross head speed of 0.2 mm/min. Six number of pellets were tested to determine the mean average compressive strength value at each point.

3.4.2.5 *In vitro* Bioactivity

Bioactivity of gelcasted sintered specimen was tested in SBF solution. The specimen was incubated in SBF for 28 days. Formation and growth of apatite on the surface of incubated specimen was analyzed through its phase analysis and surface morphologies respectively.

3.5 Sol-gel synthesis of glass-ceramics

3.5.1 Preparation of Glass-Ceramics

Glass-ceramics (GC), intended for bio-application, was prepared by sol-gel route using RHA as silica source. The flow diagram for this preparation is illustrated in Fig. 3.11. The glass-ceramics with composition (mol %) 50 SiO_2, 25 Na_2O and 25 CaO, was synthesized through sol-gel process. Sodium silicate solution (containing required stoichiometric ratio of SiO_2:Na_2O) and $Ca(NO_3)_2 \cdot 4H_2O$ (Merck, India) were used as precursors. Sodium silicate solution was prepared by boiling RHA ($SiO_2 \geq 99.87\%$, ±0.01) in 1 M NaOH solution. Calcium nitrate was dissolved in concentrated nitric acid to make the solution highly acidic. Silicate solution was then added drop wise into that highly acidic $Ca(NO_3)_2$ solution under constant stirring condition to avoid gel precipitation, as the gel was precipitated immediately when $Ca(NO_3)_2$ solution was added to sodium silicate solution. Final pH of the sol was 3. The sol turned into gel within 30 min at room temperature. The gel was aged for 3 days at 70 °C followed by drying at 150 °C for 48 h. Dried gel was crushed and ground into fine powder. Gel powder was calcined and then ground. Fine powders were compacted to form pellets followed by sintering for further characterization.

3.5.2 Characterization of Gel powder and Glass-Ceramics

3.5.2.1 Thermal Analysis of Gel Powder

Thermal decomposition behaviour of gel powder was determined by DSC/TGA analysis. The gel powder was heated from room temperature to 1000 ^oC with a heating rate of 10 ^oC/min. Gel powder was calcined at different temperatures up to 700 °C for 2 h to evaluate phase formation and crystallization behavior. Calcined powders (glass-ceramic powder) were analyzed for their crystalline phase content using XRD.

3.5.2.2 Sintering and Phase Analysis of Glass-Ceramics

The final glass-ceramics (GC) powder (calcined at 700 ^oC) was ground thoroughly. Particle size of GC powder was measured. The powder was pressed uniaxially at 250 MPa for 2 minutes to make pellets of 15 mm diameter and 3.5 mm thickness. Pellets were

sintered at 900, 950, 1000 and 1050 ^{o}C for 2 h with a heating rate of 2 °C min^{-1} from room temperature to final sintering temperature and were cooled naturally within the furnace. Phases of sintered specimen were analyzed by using XRD.

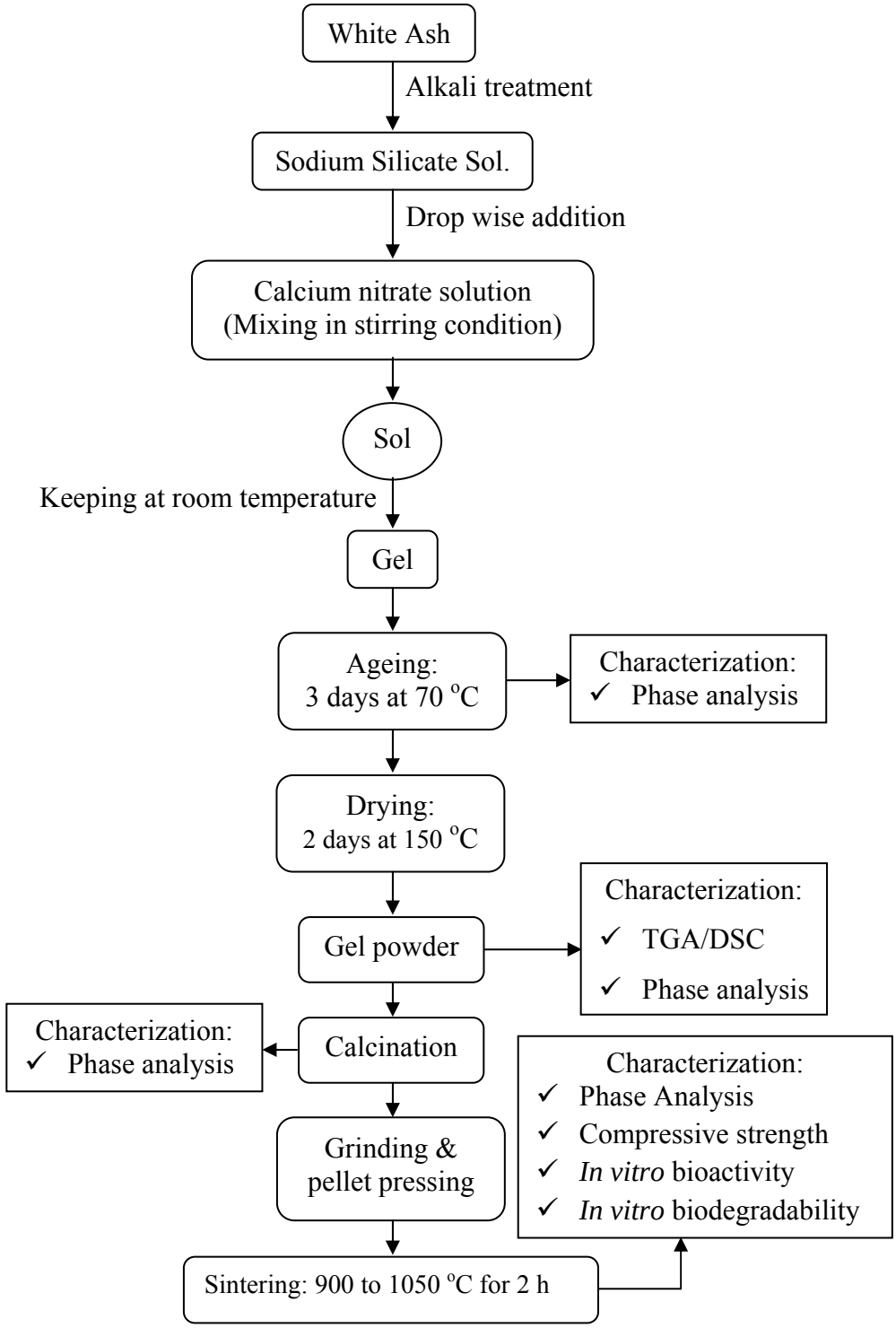

Fig. 3.11 Flow diagram of the procedure to prepare glass-ceramics.

3.5.2.3 Mechanical Properties of Glass-Ceramics

Mechanical strength was measured by compression test in an UTM using "Brazilian Disc" methods with a cross head speed of 0.5 mm min^{-1}. Six numbers of samples were tested to determine the mean average compressive strength value at each test. Surface morphologies were also investigated by SEM.

3.5.2.4 *In vitro* Bioactivity of Glass-Ceramics

The bioactivity of sintered pellets was examined by incubating the specimens in SBF solution. The change of apatite growth with incubation time periods and effect of sintering temperature on the bioactivity of sintered specimens were investigated. The surfaces of incubated specimen were investigated for phase analysis, morphology and elemental analysis by XRD, SEM and EDS respectively.

3.5.2.5 *In vitro* Biodegradability of Glass-Ceramics

In order to study the dissolution features of glass-ceramics, a TRIS buffer solution was chosen as dissolution medium. Pure TRIS was dissolved in deionized water with a concentration of 6.1 gm/lit. The solution pH was lowered to 8 using 1 M HCl solution. Sintered pellets were immersed in TRIS solution and incubated at 37 ^{o}C for different time periods upto 7 days. After each soaking experiment, pH of TRIS solution and water absorption capacity of specimen was measured.

3.6 Preparation of Aerogel by Ambient Pressure drying Method

3.6.1 Preparation of Silica Aerogel

Silica aerogel was prepared by ambient pressure drying technique using RHA as silica source. The detailed procedure of preparation is illustrated schematically in Fig. 3.12. All the chemicals used in this process were from Merck, India (GR grade with 99.9% purity). Silica gel was synthesized by neutralizing sodium silicate solution using 1 mol/L Nitric acid (HNO_3) solution; as per the procedure mentioned in section 3.1.3. The prepared gel was aged at room temperature for 24 h under sealed condition. The aged gel was washed using de-ionized water to remove sodium nitrate. The extent of Na removal was measured by analyzing Na-content of dried gel using EDS analysis. Subsequently, the

silica gel was soaked in a solution of 20 vol % H_2O/ethanol for 24 h at 50 °C followed by aging with ethanol at same condition. The ethanol treated gel was aged in a solution of 70 vol % Tetraethylorthosilicate (TEOS)/Ethanol for 24 h at 70 °C. The gel was washed with *n*-heptane for several times to remove TEOS/Ethanol solution from the gel. Then, it was aged in *n*-heptane at 50 °C for 24 h with 4 times renewal of fresh *n*-heptane. Finally, modified gels were aged for another 24 h in *n*-heptane at room temperature before air drying with partially covered condition. The gel was dried in 24 h interval at 50, 90, 120 and 150 ^oC with partially covered condition.

3.6.2 Characterization of Aerogel

3.6.2.1 Density, Apparent Porosity, Microstructure and FTIR Analysis

Bulk density and apparent porosity of silica aerogel was determined by "Archimedes" principle. The specimen was cut into rectangular shape and weighted in dry state. Sample was immersed in kerosene and kept under a vacuum of 4mm of mercury for 5 h to ensure that kerosene filled up the open pores completely. Then, soaked and suspended weights were measured. The apparent porosity and bulk density was calculated by using the formula mentioned in section 3.2.2.3. Surface morphology of aerogel specimen was analyzed by using SEM-EDS. On heating, different functional groups associated with aerogel sample were investigated through FTIR analysis.

3.6.2.2 Surface Area and Pore Size Distribution

Surface area and pore size distribution were measured by the nitrogen adsorption/desorption isotherm technique. BET (Brunauer, Emmet and Teller after the developers of the basic calculations) method was used for adsorption isotherm measurement using Quantachrome Autosorb (Model No: Nova 1200 BET).

The adsorption isotherm depends on the molar quantity of nitrogen (or it standard volume, V_a) adsorbed by the solid surface as a function of gas pressure. Plots of V_a against the reduced gas pressure, P/P_o, (P_o is the vapor pressure of nitrogen at 77K) reveal much about the pores of the adsorbing material simply by its shape and the hysteresis between the adsorption and desorption curves.

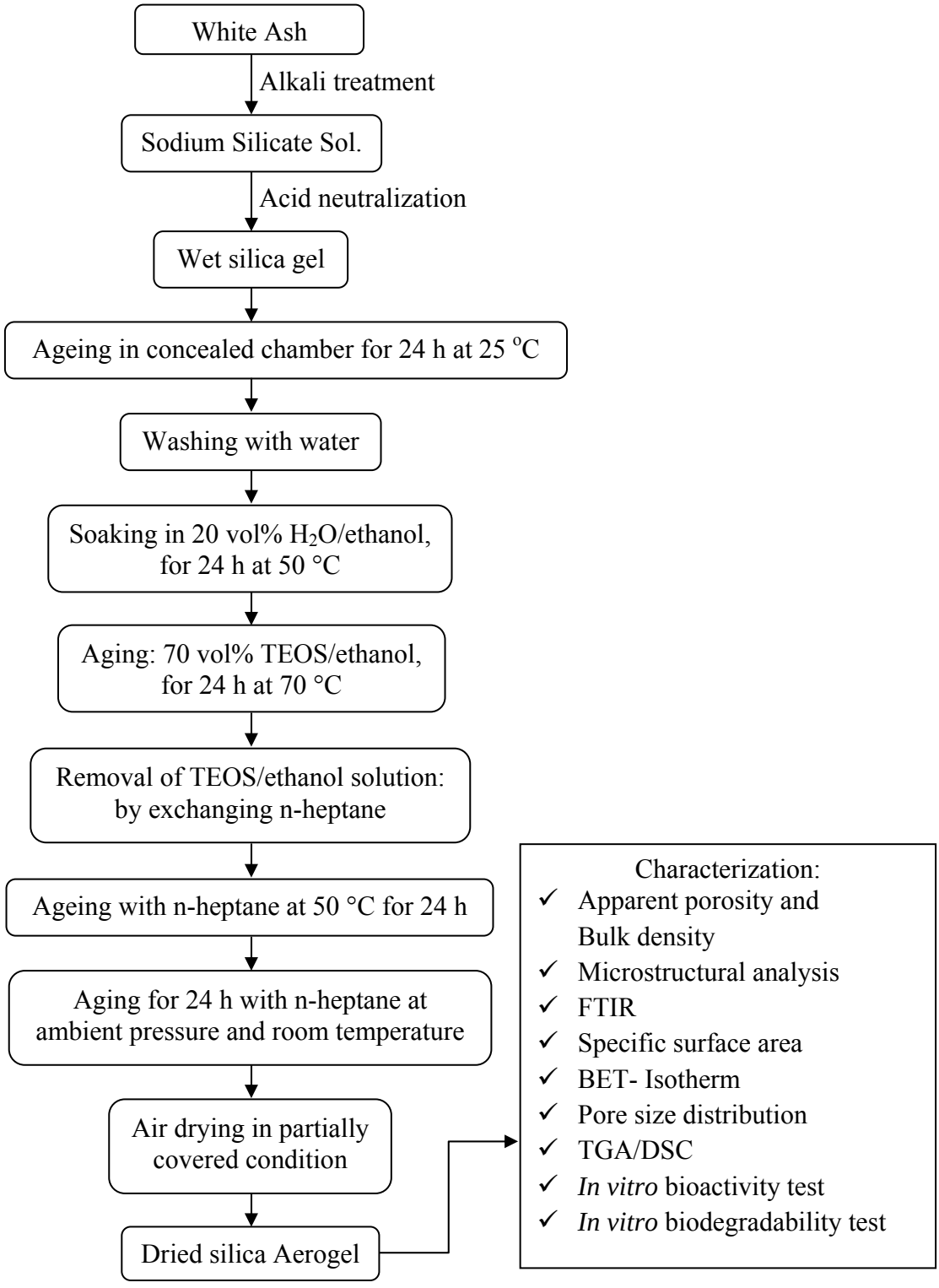

Fig. 3.12 Flow diagram of the procedure used to prepare silica aerogel by ambient pressure drying technique using WA as silica source.

The theory of BET enables the calculation of the specific surface area of the adsorbence, its pore size and volume from the adsorption/desorption data. This theory is based on the Langmuir monolayer adsorption on the solid theory. Brunauer, Emmett and Teller suggested a multilayer adsorption mechanism. The BET theory is based on the assumption that the forces active in the condensation of gases are also responsible for the binding energy in multi-molecular adsorption. By equating the rate of condensation of gas molecules onto an already adsorbed layer to the rate of evaporation from that layer and summing for an infinite number of layers, the following expression can be obtained:

$$\frac{p}{V_a(p^{LV}-p)} = \frac{1}{V_m C} + \frac{C-1}{V_m C}\left[\frac{p}{p^{LV}}\right] \qquad (3.11)$$

C is the constant, resulting from the difference between the enthalpy of adsorption of the first layer and enthalpy of condensation of nitrogen. The values of V_m and C may be obtained from a straight-line plot of $\frac{p}{V_a(p^{LV}-p)}$ vs. $\frac{p}{p^{LV}}$. The volume of the monolayer, V_m having been determined, allows the surface area of the sample to be determined using the area occupied by a single nitrogen molecule (16.2 Å at 77K).

This method was successfully applied to determine the specific surface area and pores size distribution of silica aerogel. About 0.05 gm of sample was taken in the sample cell and degassed at 150 ^{o}C in vacuum up to a maximum of 3 mbar. The sample holder mouth was closed by a stopper. Sample was cooled and the cell was placed in liquid nitrogen bath. The equipment measured the amount of gas adsorbed on the surface of the sample and the specific surface area was calculated.

3.6.2.3 *In vitro* Bioactivity and Biodegradability of Aerogel

Bioactivity of aerogel was checked by incubating the aerogel specimen in SBF for 7, 14 and 21 days at 37 ^{o}C. After being soaked, samples were rinsed with distilled water and dried in dessicator at room temperature. SBF incubated sample surface was then investigated by XRD for phase analysis, SEM for morphology and EDS for elemental analysis. The dissolution feature of aerogel sample was evaluated in TRIS buffer solution; the detail procedure about biodegradability of silica-based ceramics has been mentioned in section 3.2.2.5.

References

[1] H. M. Rietveld, J. Appl. Cryst. 2 (1969) 65.

[2] R. A. Young, Rietveld Method, International Union of Crystallography, Oxford University Press (1996).

[3] A.T. Procopio, A. Zavaliangos, J.C. Cunningham, J. Mater. Sc. 38 (2003) 3629-3639.

[4] A. Cuneyt Tas, Biomaterials 21 (2000) 1429.

[5] M.G. Cerruti, D. Greenspan, K. Powers, Biomater. 26 (2005) 4903.

[6] A. Nieto, S. Areva, T. Wilson, R. Viitala, M. Vallet-Regi, Acta Biomater. 5(9) (2009) 3478.

[7] O.G. Koch, G.A. Koch-Dedic (1974) In: Handbuch der Spurenanalyse Silicon molybdanblau-Verfahren. Springer-Verlag, Berlin.

[8] H. Levine, J.J. Rowe, F.S. Grimaldi, 27 (1955) 258.

[9] www.malvern.com

Chapter 4

Results & Discussion

4.1 Preparation and Characterization of Amorphous Silica Precursors

4.1.1. Introduction

Three types of amorphous silica powders were prepared using rice husk. They are brown ash (BA), white ash (WA) and silica gel (SG). BA was prepared by burning husk at 700 ^{o}C. WA was prepared by burning acid washed husk. The SG was prepared from BA through alkaline extraction of silica and acid neutralization processes. All these silica precursors were characterized for their phase analysis, chemical composition and FTIR analysis.

4.1.2. Results and Discussion

4.1.2.1 Phase Analysis

Fig. 4.1 shows the X-ray diffraction patterns of WA, BA along with raw and cleaned husk. In all cases broad peak zone centered near $2\theta=22^{o}$, signifies the amorphous nature of silica based materials. A sharp crystalline peak in raw husks at $2\theta=26.86^{o}$ was due to the presence of impurities sand particles as the peak was identified to match with quartz. There was no quartz peak in cleaned husk. BA and WA shows typical amorphous pattern of silica. They were prepared by burning the husk at 700 ^{o}C, as it is known that silica of husk remains amorphous upto about 850 ^{o}C [1]. There was no visible residual un-burnt carbon in BA and WA.

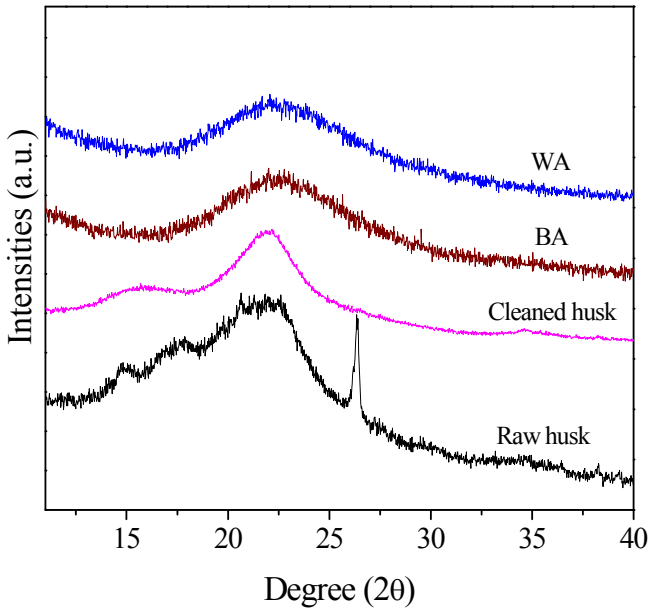

Fig. 4.1 X-ray diffraction patterns for WA, BA, cleaned husk and raw husk.

SG was prepared by acid neutralization of sodium silicate solution derived from BA. HCl was used for the neutralization. Fig. 4.2 shows the XRD patterns of SG as-prepared (unwashed) and after thorough washing. Unwashed SG exhibits presence of NaCl and Na_2SiO_3, as shown in Fig. 4.2 (a). These compounds were found because the sodium silicate was neutralized by HCl, as stated above. However, those crystalline peaks are absent in washed gel (Fig. 4.2 (b)). Washed SG is completely amorphous in nature.

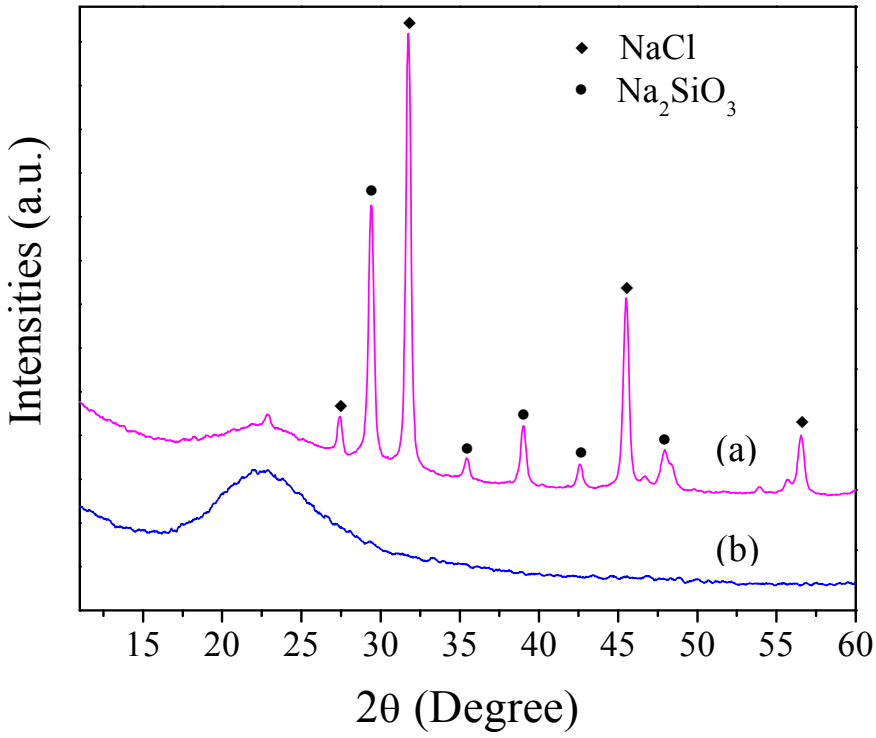

Fig. 4.2 X-ray diffraction patterns for (a) Unwashed and (b) Washed Silica gel (SG).

Presence of sodium based compound in unwashed SG was also confirmed by analyzing its surface microstructure (Fig. 4.3 (a)). Unwashed SG shows a granular morphology. EDS spectra shows Na and Cl peaks due to the presence of NaCl on the surface. During the drying of unwashed gel, dissolved NaCl comes to the surface along with water and dries into granular form. Those granules are absent in washed gel (Fig. 4.3 (b)). Corresponding EDS also shows no peaks for Na and Cl. It can be concluded that the washing procedure applied for the preparation of SG was efficient to remove all NaCl from silica hydrogel.

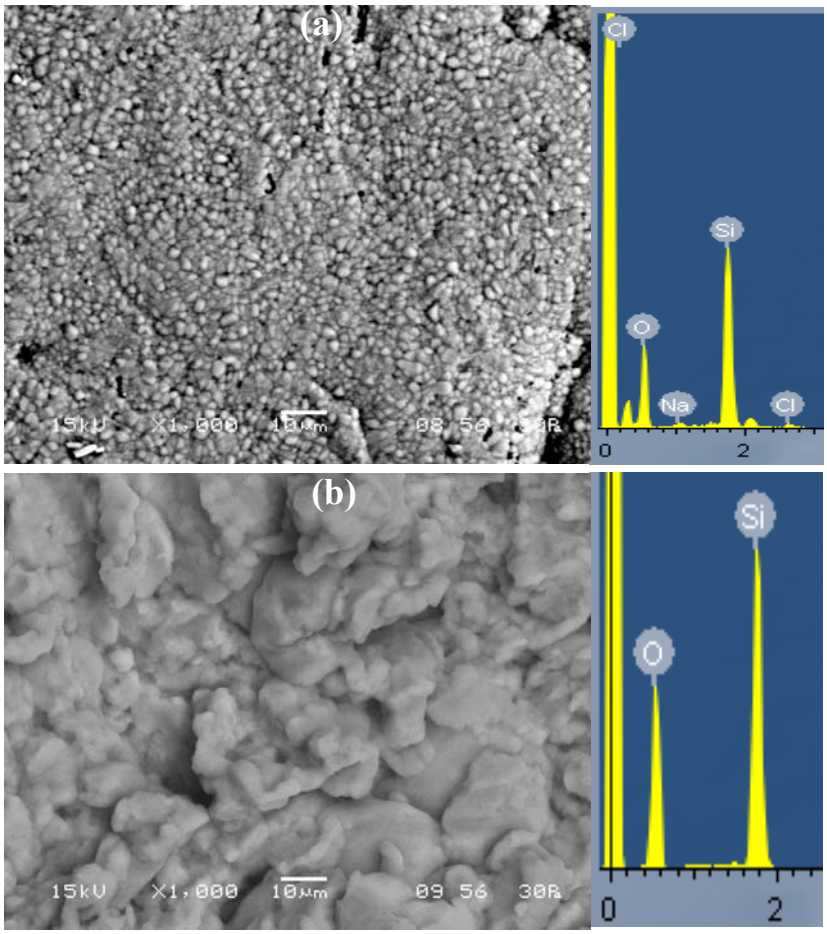

Fig. 4.3 SEM and EDS photographs of (a) Unwashed and (b) Washed silica gel.

4.1.2.2 Chemical Analysis

Chemical analysis of raw husk, BA, WA and SG was carried out using XRF. Table 4.1 shows the chemical composition (oxide basis) of three silica precursors. BA contains approximately 96% SiO_2 and the rest 4% are oxides of potassium, calcium, iron, zinc, and manganese. Except SiO_2, all other oxides may be considered as impurities. The brown colour of BA is attributed to the presence of these impurities. WA contains nearly pure SiO_2 (99.87%). It was prepared from the husk which was thoroughly acid leached. The acid leaching was effective to remove most of the impurities those stated above for BA. Silica content of SG is about 99.78%. The SG was prepared through alkali extraction of amorphous silica of BA, and then by acid neutralization of silicate solution to form gels. The impurities were low in SG compared to BA, because they were partially removed during the processing of gel.

Table 4.1 Chemical analysis of silica precursors (mass %)

Oxides	Raw Husk	Brown Ash	Silica Gel	White ash
Organic Matter	75.6			
SiO_2	17.26	96.01	99.79	99.87
K_2O	0.28	0.86	-	-
CaO	1.11	2.22	0.13	-
Fe_2O_3	2.86	0.57	0.03	0.13
Al_2O_3	1.37			
ZnO	0.67	0.06	0.05	-
Na_2O	0.84			
Mn_2O_3	0.11	0.28	-	-

4.1.2.3 FTIR Analysis

FTIR spectra of BA, WA and SG are shown in Fig. 4.4. Spectra for BA and WA are almost same. The broad band at 3410-3470 cm^{-1} is due to the stretching vibration of the O-H bond from the silanol groups (Si-OH) and is due to the adsorbed water molecules on the silica surface. The band at 2344 cm^{-1} is due to the carbonate which is absorbed in the sample from atmosphere during sample preparation. The band at 1090 cm^{-1} is due to the Si-O-Si asymmetric stretching vibration, while the band at 801 cm^{-1} has been assigned to the network Si-O-Si symmetric bond stretching vibration. The band at 470 cm^{-1} is associated with a network O-Si-O bond bending modes. The same IR peaks were obtained for SG, as stated above for BA and WA. Apart from these, the band at 1654 cm^{-1} is due to bending H-OH bond of adsorbed water molecules on SG and the band at 959 cm^{-1} is due to the stretching mode Si-OH typical of gel structure. It has been mentioned by several researchers that surface -OH can easily be formed when the silica gel is exposed to the atmosphere [2, 3].

4.1.3 Summary

Three different varieties of amorphous silica; namely, brown ash (BA), white ash (WA) and silica gel (SG) were prepared from rice husk. All were completely amorphous with some differences in purity or silica content. BA, prepared by burning husk, contains

about ~ 96 wt.% SiO_2 (by mass) and the rest 4 wt.% impurities like CaO, Fe_2O_3, K_2O, ZnO, and Mn_2O_3. WA, prepared by burning acid-leached husk, contains almost pure silica (99.87 wt.%). SG was prepared from BA through the alkaline extraction of silica from ash followed by acid neutralization. Silica content of SG was ~ 99.79 wt.%. SG was very prone to form surface -OH group due to it's gel structure. These raw materials have been used for the preparation of amorphous silica-based bioactive ceramics.

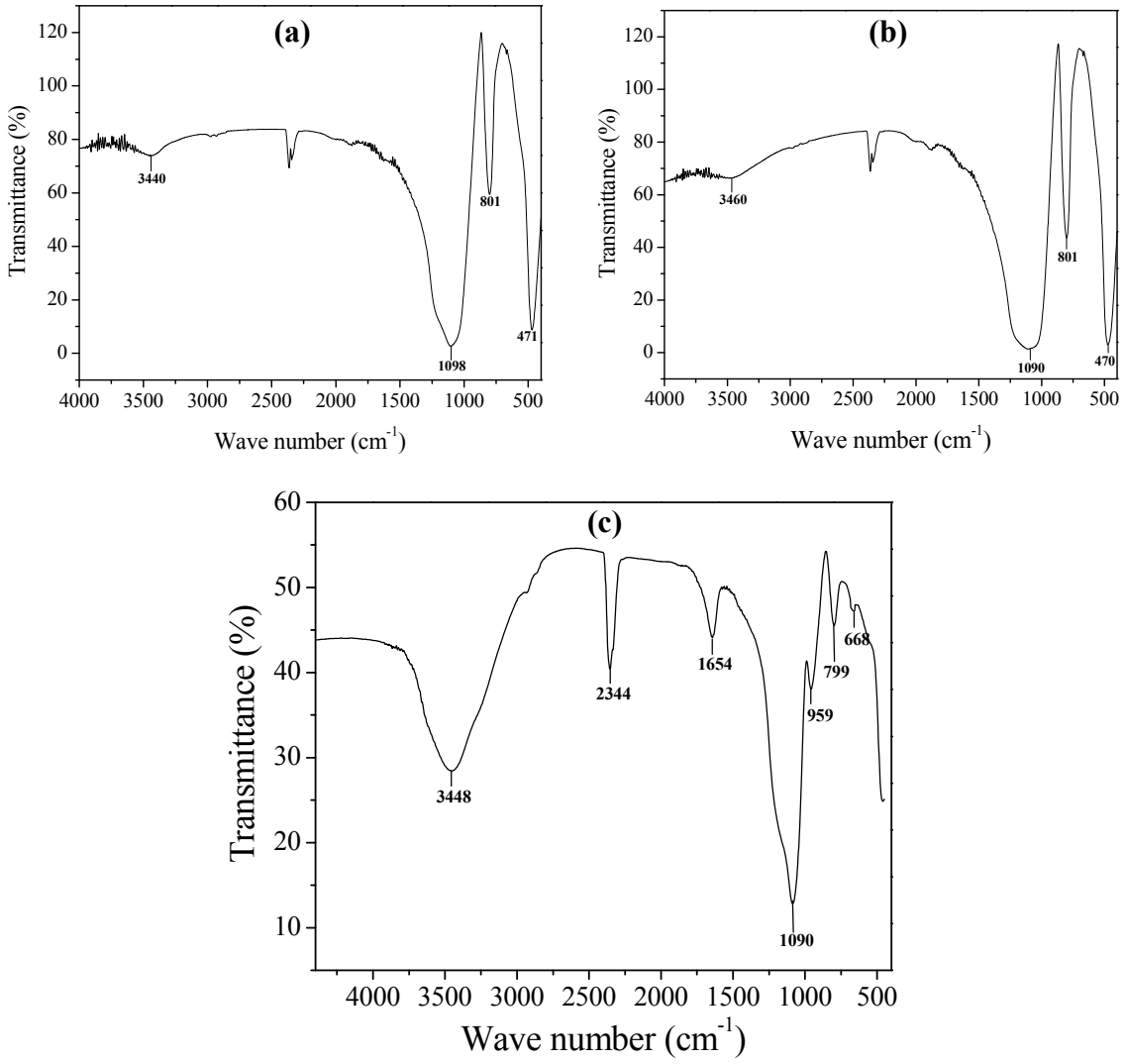

Fig. 4.4 FTIR spectra of (a) BA, (b) WA and (c) SG powders.

4.2. Bioactivity of Silica-based Ceramics Prepared by Powder Compaction Method

4.2.1. Introduction

Amorphous silica ceramics were prepared by powder pressing method using brown ash, white ash and silica gel powders. Powders were characterized for their particle size distributions. They were compacted through uniaxial pressing to cylindrical disk shapes. Pellets were sintered at different temperatures. Sintered pellets were characterized for their phase composition using XRD and FTIR. Effects of sintering on densification, microstructural changes and mechanical properties were evaluated. Finally, bioactivity and biodegradability properties of silica ceramics were investigated and co-related with other properties.

4.2.2. Results and Discussion

4.2.2.1 Particle Size Distribution of Silica Precursors

Fig. 4.5 shows the particle size distribution of BA, WA, and SG powders. Unimodal and narrow particle size distribution with an average particle size (d_{50}) of 183 and 150 μm were found for WA and BA powders, respectively. In the case of SG powder, it is composed of variable particle sizes ranging from 2-40 μm. These powers were compacted uniaxially to pellet shapes. Green pellets were sintered at temperatures ranging from 700 to 1400 ^{o}C for 2 h for different silica varieties.

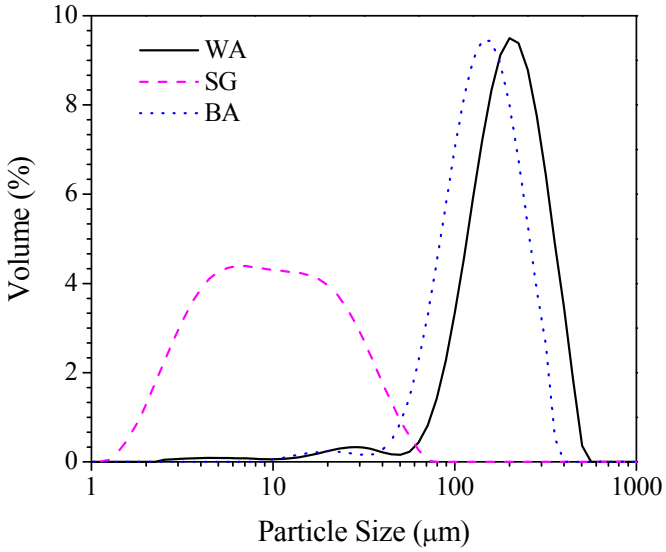

Fig. 4.5 Particle size distribution of BA, WA, and SG powders.

4.2.2.2 Phase Analysis

Effect of sintering on amorphous phase retention and crystalline phase formation of different silica specimen were investigated. Fig. 4.6 shows the XRD patterns of BA, WA and SG specimen heat treated at two different temperatures corresponding to amorphous phase retention and crystallization respectively. BA was amorphous up to 900 ^{o}C and it transformed into crystalline silica at 1000 ^{o}C. XRD patterns of SG and WA were very similar to BA patterns. It was found that WA and SG transformed into crystalline phases from amorphous states at 1300 and 1200 ^{o}C, respectively. The results indicate that crystallization temperature was different for different types of silica.

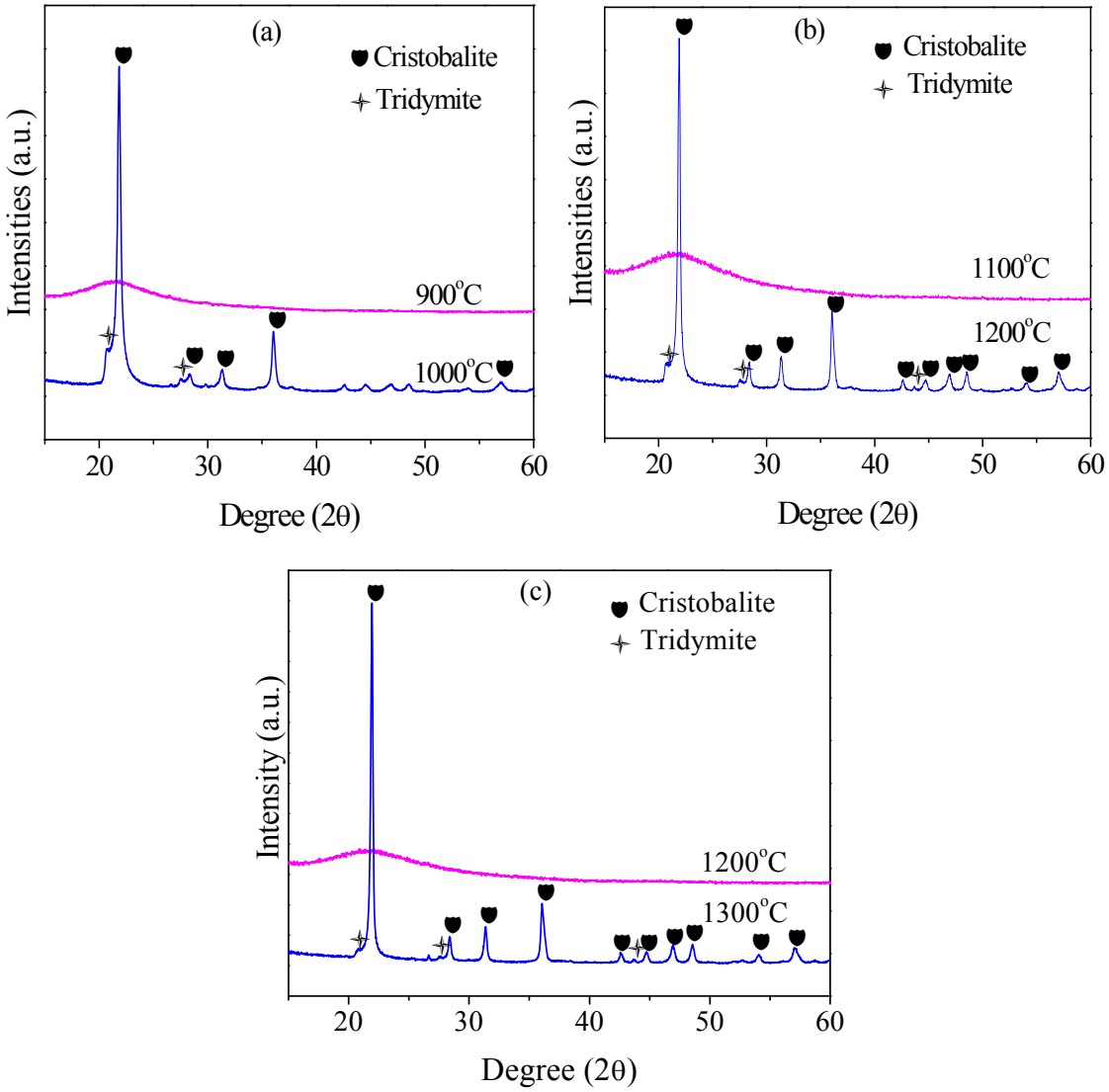

Fig. 4.6 Amorphous and crystalline XRD patterns of sintered specimen made of (a) BA, (b) SG, and (c) WA. Sintering temperature and crystalline phases are indicated.

The crystallization temperature in BA was lowest among three, due to the presence of highest amount of impurities (~4 wt.%) in it. The chemical compositions of powders have been presented in Section 4.1.2.2. Briefly, WA contains nearly pure SiO_2 (99.87 wt.%), SG ~ 99.78 wt.% and BA contains ~96 wt.% silica. The crystallization temperature of WA was highest among all due to its lowest impurity content (~0.13 wt.%). The crystallization temperature for SG was intermediate between WA and BA. It is reported that impurities and water vapor play a role in the phase transformation of SiO_2 [4]. Alkalis like K_2O and Na_2O accelerate the transformation of amorphous SiO_2 to cristobalite or tridymite in RHA [5]. Similar accelerated transformation behaviour has been established for silica ceramics.

It is well established that RHA constitutes amorphous silica. To investigate the structural features of this amorphous material, Rietveld structure refinement was performed on each material. Fig. 4.7 shows the typical Rietveld plots after final refinement for BA pellets sintered at 900 and 1000 ^oC. Refinement R-factors and Goodness-of-fit (σ) are shown in the figure. For amorphous pattern refinement, silica glass (cubic, space group $P2_13$) and low cristobalite (tetragonal, space group $P4_12_12$) were fitted in separate refinements. It was interesting to note that fitting with low cristobalite yielded lower R-factor and better σ compared to silica glass. So, the amorphous silica in ash may be considered structurally more similar to low cristobalite. Many authors also proposed similar low cristobalite structure for amorphous silica in ash [6, 7].

For crystalline specimen BA-1000 ^oC, a three-phase refinement was carried out considering low cristobalite ($P4_12_12$), tridymite ($P6_3/mmc$), and low quartz (trigonal, $P2_33_4$). Rietveld quantitative estimation shows about 62 wt.% low cristobalite, 30 wt.% tridymite, and 8 wt.% quartz. Since amorphous ash is more similar to low cristobalite, the formation of low cristobalite from amorphous material is justified. The specimen was heated at 1000 ^oC, which is the thermodynamic stability range for tridymite. For that reason, tridymite phase also crystallizes during heat treatment. The phase-transform anomaly in silica is a well-known phenomenon. Some amount of quartz also crystallizes may be due to this anomaly. Similar phase-formation behavior was also found in the case of SG and WA specimens.

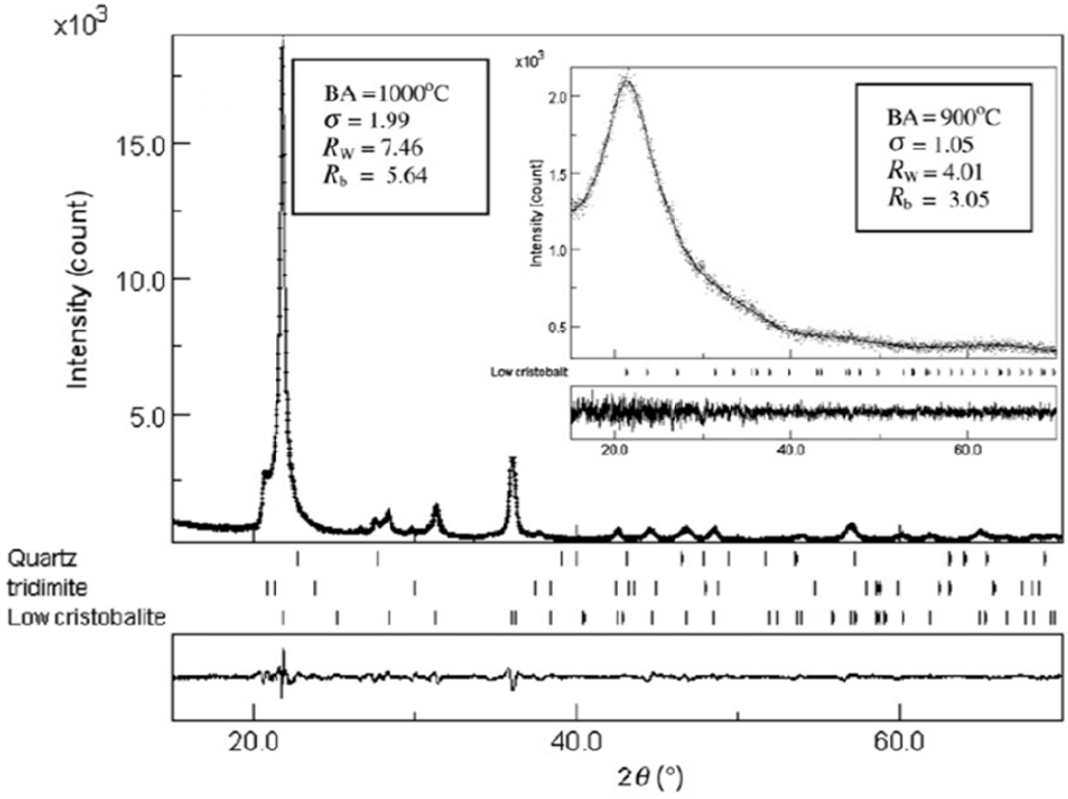

Fig. 4.7 Rietveld refinement output for quantitative phase estimation of BA.

4.2.2.3 FTIR Analysis

The presence of water vapor has been considered to play a role in the phase transformation of SiO_2. FTIR analysis was performed to study the crystallization behavior and nature of bound water in the silica specimen. Fig. 4.8 shows the IR spectra of three specimens at their amorphous state and after crystallization. In all silica specimens, the broad band around 3410-3470 cm^{-1} is due to the stretching vibration of the O-H bond from the silanol groups (Si-OH) and the HO-H vibration of adsorbed water molecules. The small band at 1635 cm^{-1} is attributed to the bending H-OH bond of adsorbed water molecules. These bands were present even in sintered samples because water molecules were unable to escape from the silica matrix [8]. The band at 1100 cm^{-1} is due to the Si-O-Si asymmetric stretching vibration, while the band at 800 cm^{-1} has been assigned to a network Si-O-Si symmetric bond stretching vibration [9]. The band at 477 cm^{-1} is associated with a network O-Si-O bond bending modes [10]. In the case of crystalline SiO_2 (BA-1000 ^oC, SG-1200 ^oC, and WA-1300 ^oC), the new band at 622 cm^{-1}

is attributed to the polymerized structure of framework crystalline silica [10, 11]. This is described as structure-dependent Si-O-Si symmetrical stretching vibrations [11] of cristobalite phase. This characteristics band of cristobalite has also been reported by Ying et al. [12].

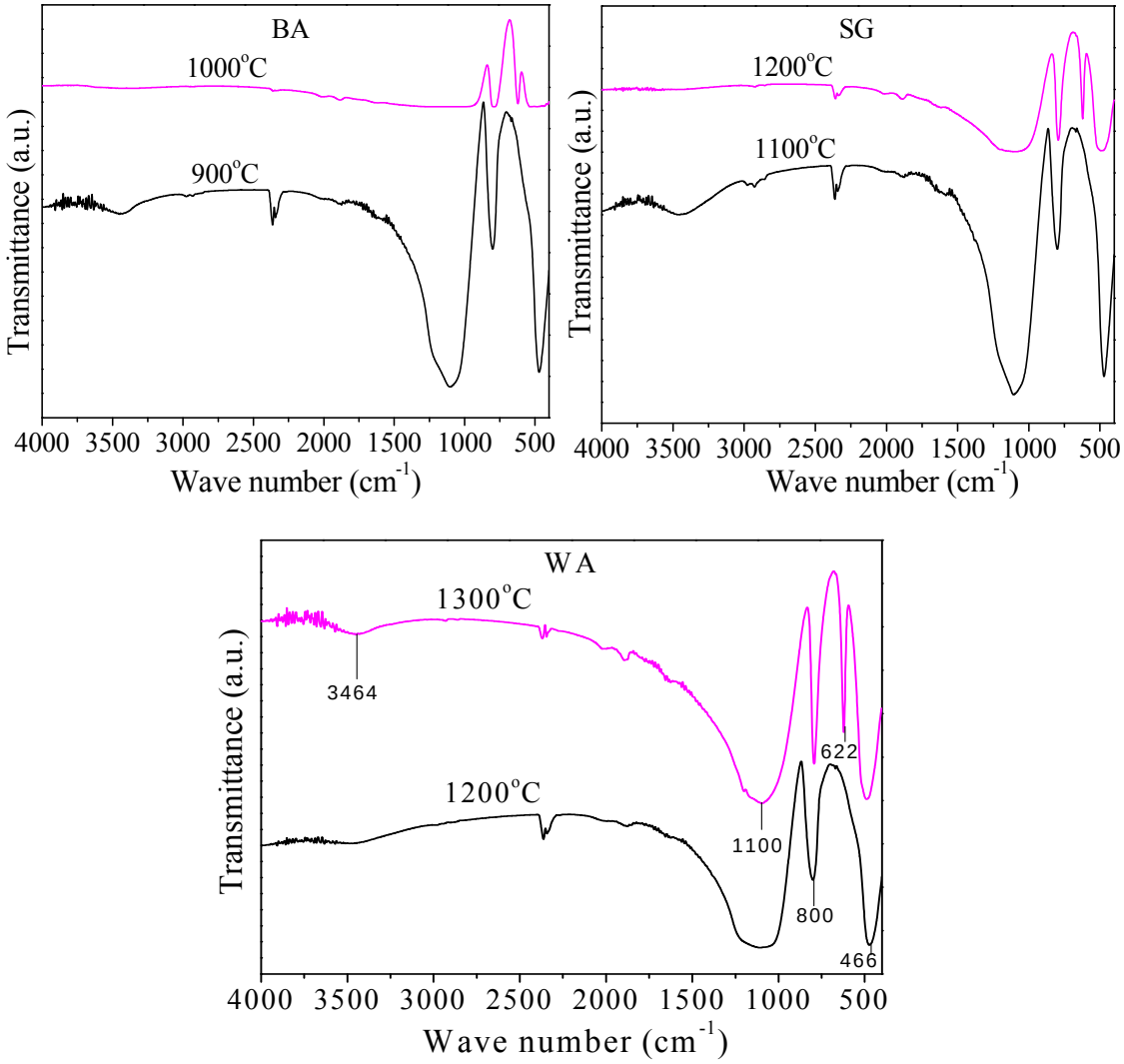

Fig. 4.8 FTIR spectra of BA, SG, and WA specimens. Sintering temperature is presented with each spectra.

4.2.2.4 Density and Apparent Porosity

Fig. 4.9 shows the bulk density and apparent porosity in terms of water absorption of different sintered specimens. Bulk density of BA increases slowly up to 800 °C followed by a rapid increase up to 1000 °C. Above 1000 °C, the densification rate was very slow and it shows approximately 20% water absorption. Densification rate of WA was slow up

to 1000 °C followed by an increased rate up to 1300 °C, with water absorption of approximately 1%. However, the densification rate of SG was rapid in the range of 700-900 °C, moderate in the range 900-1200 °C and slow above 1200 °C, with approximately 1% water absorption. Results show that the SG and WA can be sintered to nearly fully dense at 1200 and 1300 °C respectively. SG was easiest to sinter among all the silica.

The most important driving force for sintering is the curvature of the particle surface. Finer the particles, higher will be the curvature and better will be the sinterability. SG has much finer particle size (5-11 μm) than the other two ashes (~183 μm for WA and ~150 μm for BA). For that reason, SG has highest sinterability. However, the green density of SG (~ 0.87 gm.cc^{-1}) was lowest among all. Green density for WA and BA was ~1.09 and ~1.19 gm.cc^{-1} respectively. Finer particles are more prone to agglomeration, so the green density of SG is lower than others with coarser particles.

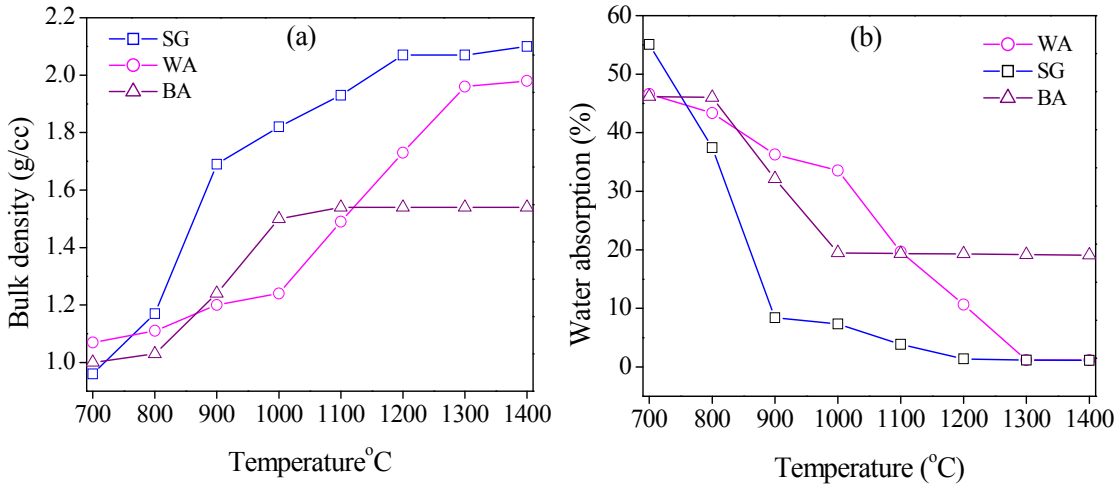

Fig. 4.9 Variation of (a) bulk density and (b) water absorption of specimen with sintering temperature.

Initial slow densification of BA and WA may be due to the particle rearrangement. Intermediate increased densification, as well as the initial densification of SG, is due to the viscous flow of amorphous material into the pores. Sintering process in amorphous material refers to viscous sintering where matter transport occurs predominantly by viscous flow [13]. Viscosity decreases with increasing sintering temperatures as well as with increasing impurities. For this reason, densification increased with increasing sintering temperature. The rapid densification stage in BA

starts from 800 ^{o}C compared to that of WA at 1000 ^{o}C. The possible reason may be the decreased viscosity of BA as it contains nearly 4 wt% impurities. The initial increased densification of SG may be due to its decreased viscosity as the material is gel. There was a marked change in the densification slope at 900 ^{o}C in SG. This may be due to the differential densification behavior of bimodal particle size distribution in SG, where finer particles and associated small pores favor rapid sintering.

The final stage of densification where there was very slow increase in bulk density started from 1000, 1200, and 1300 ^{o}C for BA, SG, and WA, respectively. The rate of densification and pore removal was very slow in BA above 1000 ^{o}C may be due to the transformation of amorphous materials into crystalline phase. It has been stated in Section 4.2.2.2, that crystallization of BA takes place at 1000 ^{o}C. The crystalline phase has considerably lower amount of defects than amorphous phase and thus densification decreased. The density of BA was lowest among all due to the early crystallization in the body. Densification of SG and WA were virtually stopped above 1200 and 1300 ^{o}C, respectively, due to the same crystallization phenomenon. Crystalline silica has about 49% co-valent bond which does not permit its easy densification. These are the typical examples of viscous sintering with crystallization [13]. From the results, it may be concluded that the most favorable processing strategy for amorphous silica is the achievement of full density prior to crystallization.

4.2.2.5 Mechanical Property and Microstructure

Fig. 4.10 shows the compressive strength of BA, WA, and SG with different sintering temperatures. The strength increases with sintering temperature, mainly due to the increase in bulk density for all ceramics. However, there was an anomaly; that is the fall in strength for each ceramic at a specific sintering temperature. These specific sintering temperatures were 1200, 1300, and 1400 ^{o}C for SG, WA, and BA, respectively. To investigate the reason for this strength anomaly, the microstructural investigation was performed on sintered pellets. Fig. 4.11, Fig. 4.12 and Fig. 4.13 shows the surface microstructure of the three ceramics that were sintered at specific temperatures where anomaly takes place. All ceramics show the formation of crack.

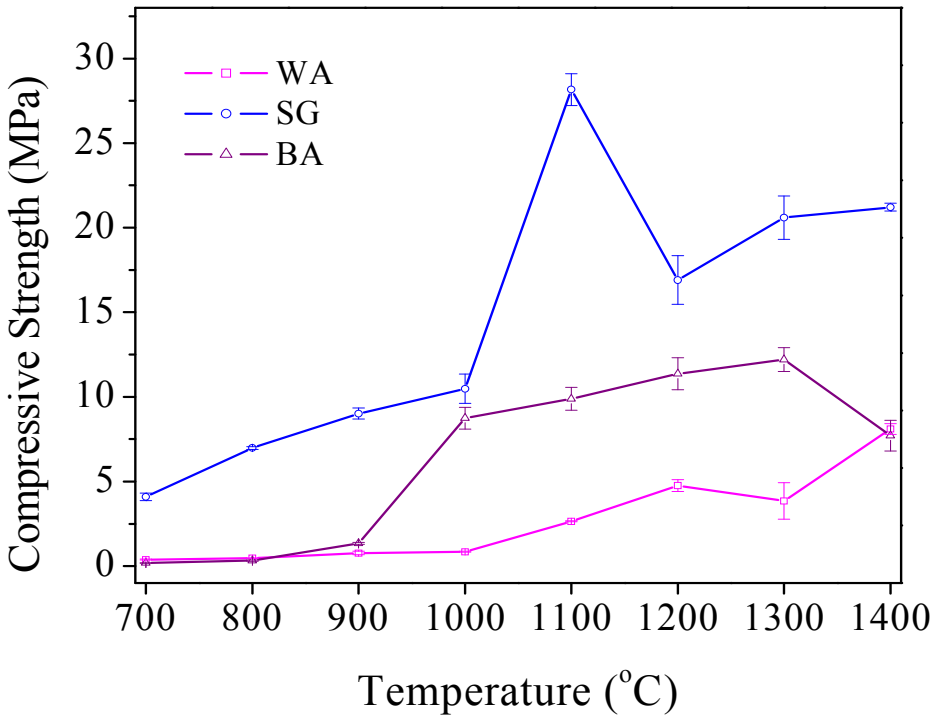

Fig. 4.10 Variation of compressive strength with sintering temperature.

For SG and WA ceramics, the strength anomaly temperatures were their crystallization temperatures, as described earlier. The crystalline phases were mainly cristobalite and the crack formation was due to the volume change associated with β- to α-cristobalite phase transition, which occurred in the temperature range of 200-270 °C during the cooling of sintered specimens. Mechanical strength of these ceramics decreased due to this cracks. In case of SG and WA ceramics, strength increased after sintering above 1200 and 1300 °C respectively. This increased in strength is due to the increased densification with temperature. Strength development behavior of BA ceramics shows some differences from the other two ceramics as shown in Fig. 4.10. As described above, the crystallization in BA takes place at 1000 °C. However, the strength of the ceramics increased at that temperature. This phenomenon is contradictory to that in SG and WA ceramics. At 1000 °C, the BA body contains ~ 20% porosity. The porous structure may accommodate the volume change due to β- to α-cristobalite transformation. So the increased strength at 1000 °C may be due to increased densification as there was approximately 14% decrease in water absorption compared with 900 °C specimen. There

was very slow strength development from 1000 to 1300 ^{o}C due to slow densification. The decrease in strength at 1400 ^{o}C may be due to the formation of increased amount of cristobalite and prominence of crack, as shown in Fig. 4.11. Similar types of cracks were generated in 1200 and 1300 ^{o}C sintered SG and WA specimens respectively (Fig. 4.12 and Fig. 4.13).

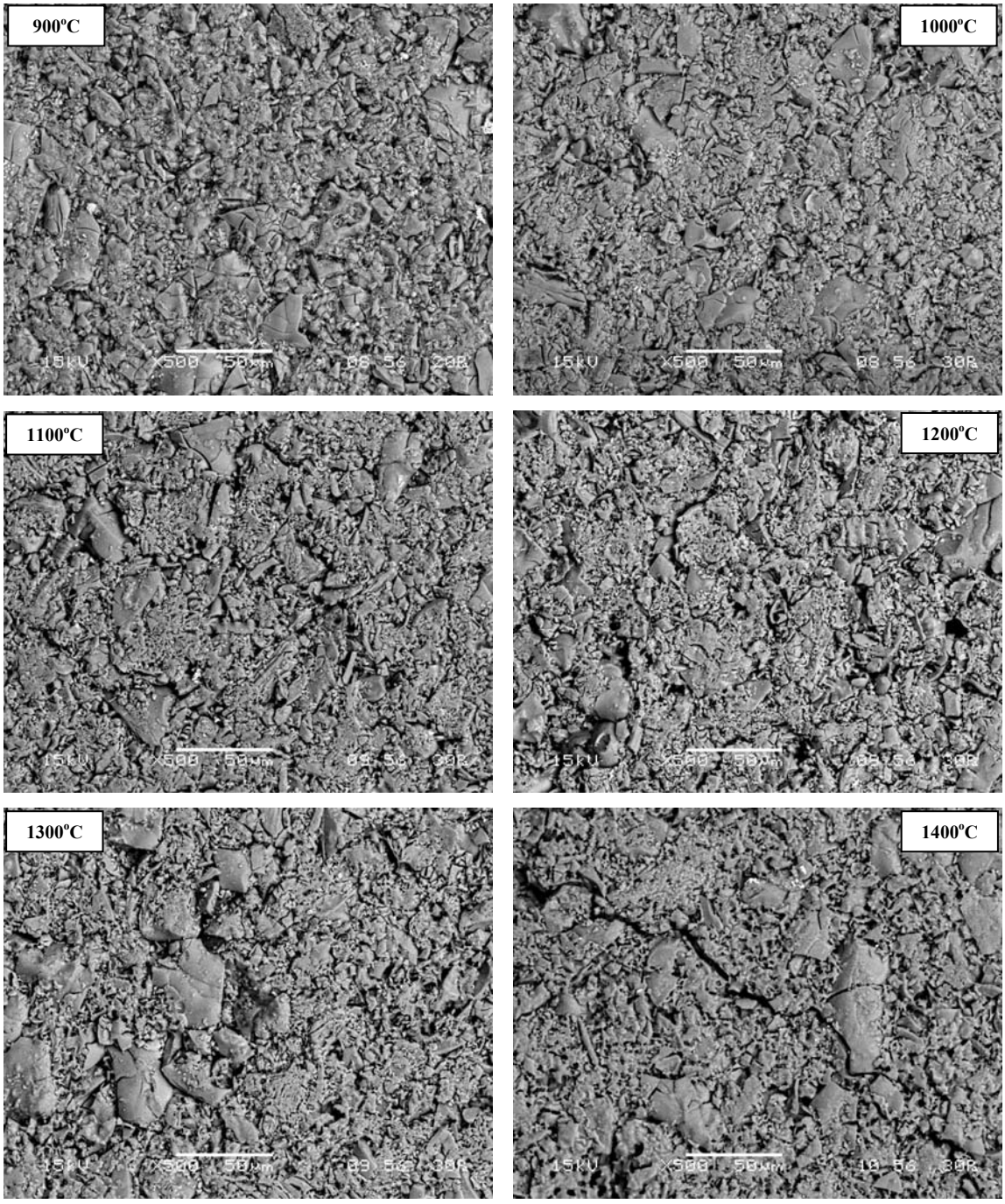

Fig. 4.11 Surface microstructure of BA specimen sintered at different temperatures.

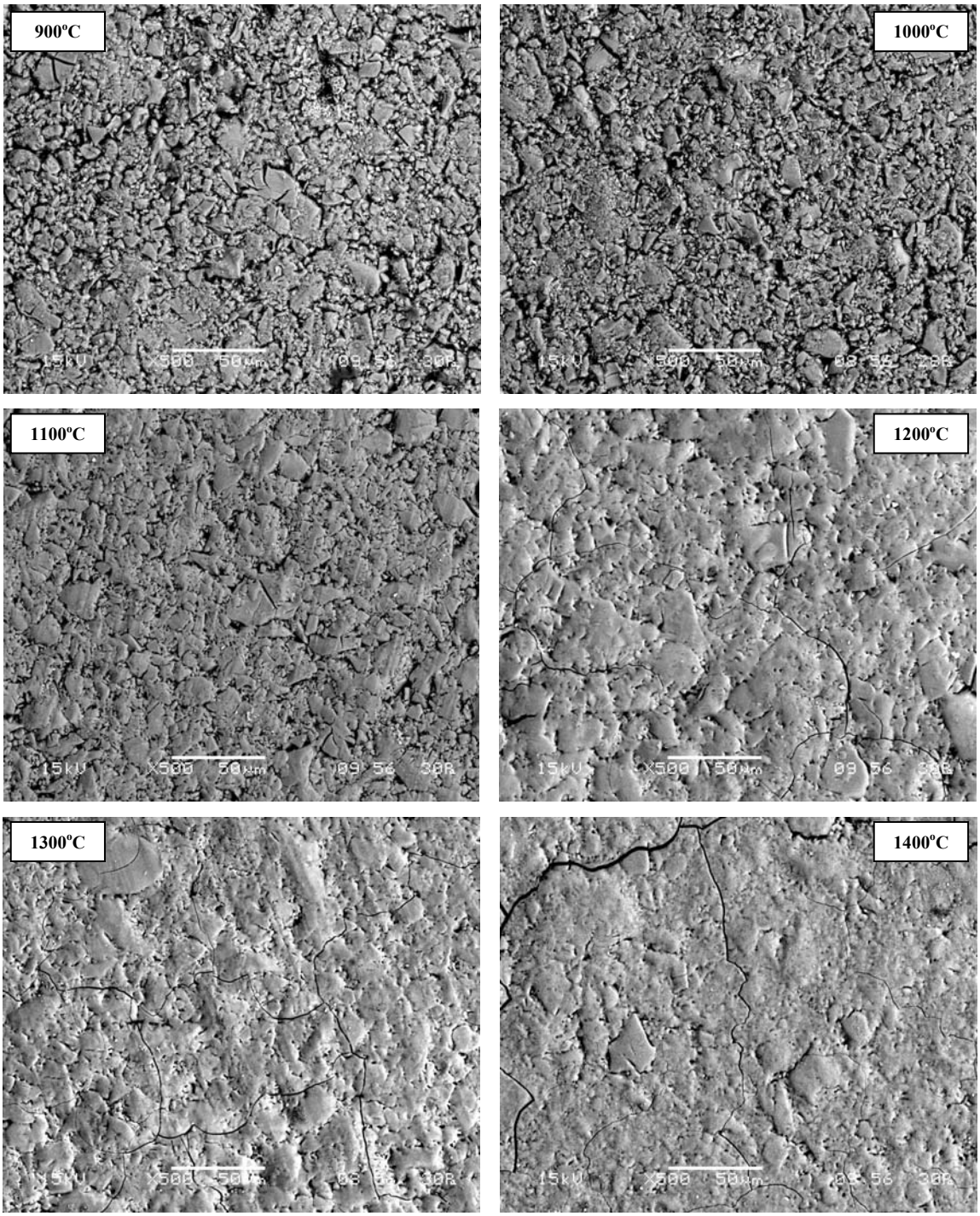

Fig. 4.12 Surface microstructure of SG specimen sintered at different temperatures.

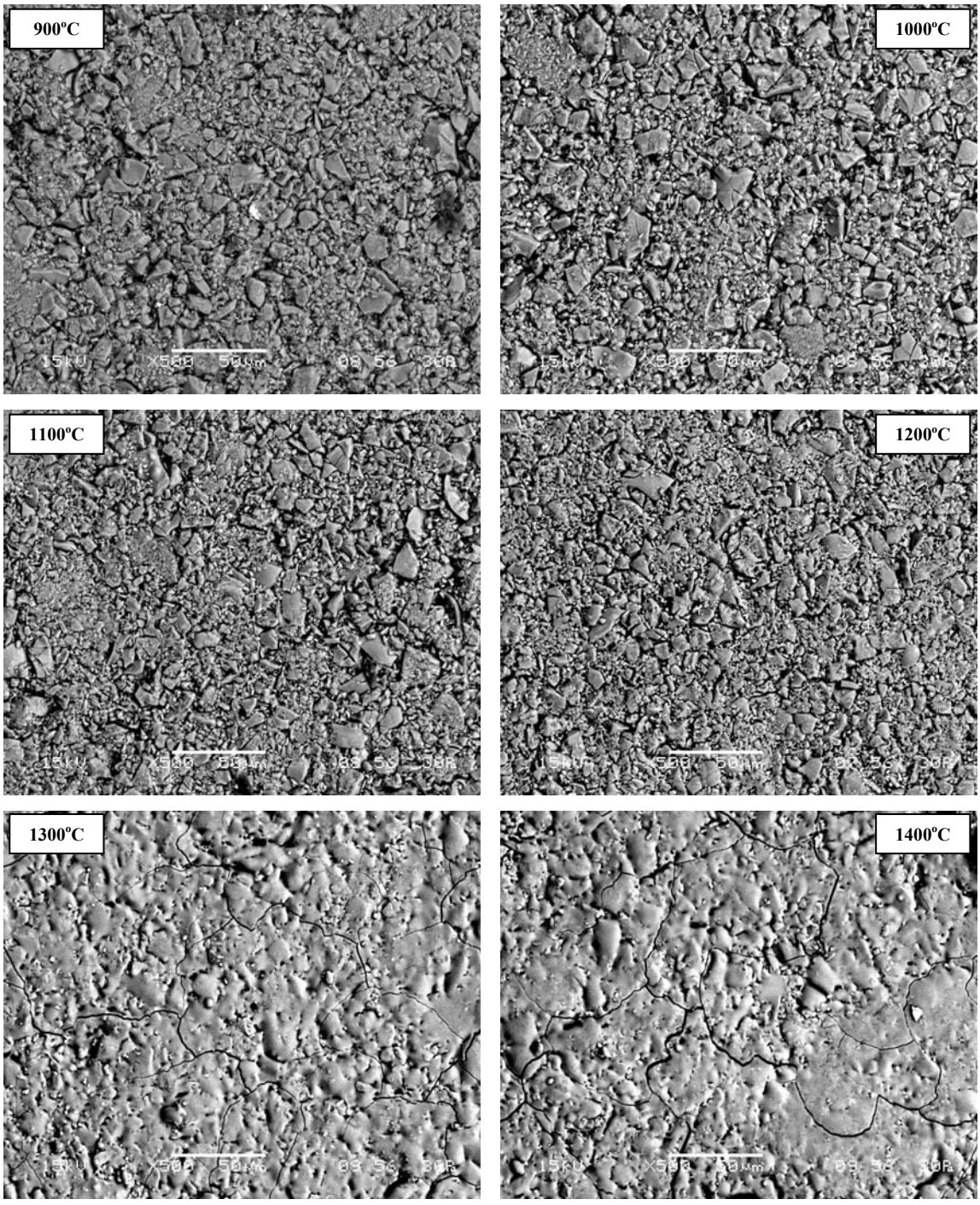

Fig. 4.13 Surface microstructure of WA specimen sintered at different temperatures.

4.2.2.6 *In vitro* Bioactivity

4.2.2.6.1 Phase Analysis

Fig. 4.14 shows the X-ray diffraction patterns of amorphous BA, SG and WA ceramic surfaces after SBF immersion for 7, 14 and 21 days. Amorphous ceramics used were sintered at 900, 1100 and 1200 ^{o}C for BA, SG and WA respectively. 7 days BA specimen shows calcium hydrogen phosphate hydrate; $Ca_8(HPO_4)_2(PO_4)_4\ (H_2O)_5$ phase (Fig. 4.14 (a)). Whereas, 14 and 21 days BA specimen show HAp; $Ca_{10}(PO_4)_6(OH)_2$ phase on their surfaces. SG specimen shows similar behavior of hydrated calcium phosphate precipitation in 7 days and conversion of phosphate phase into HAp in 14 days and above (Fig. 4.14(b)). In case of WA (Fig. 4.14 (c)), hydrated calcium phosphate phase appears only in 14 days and HAp appeared in 21 days. The results indicate that BA and SG ceramics are more bioactive than WA ceramics.

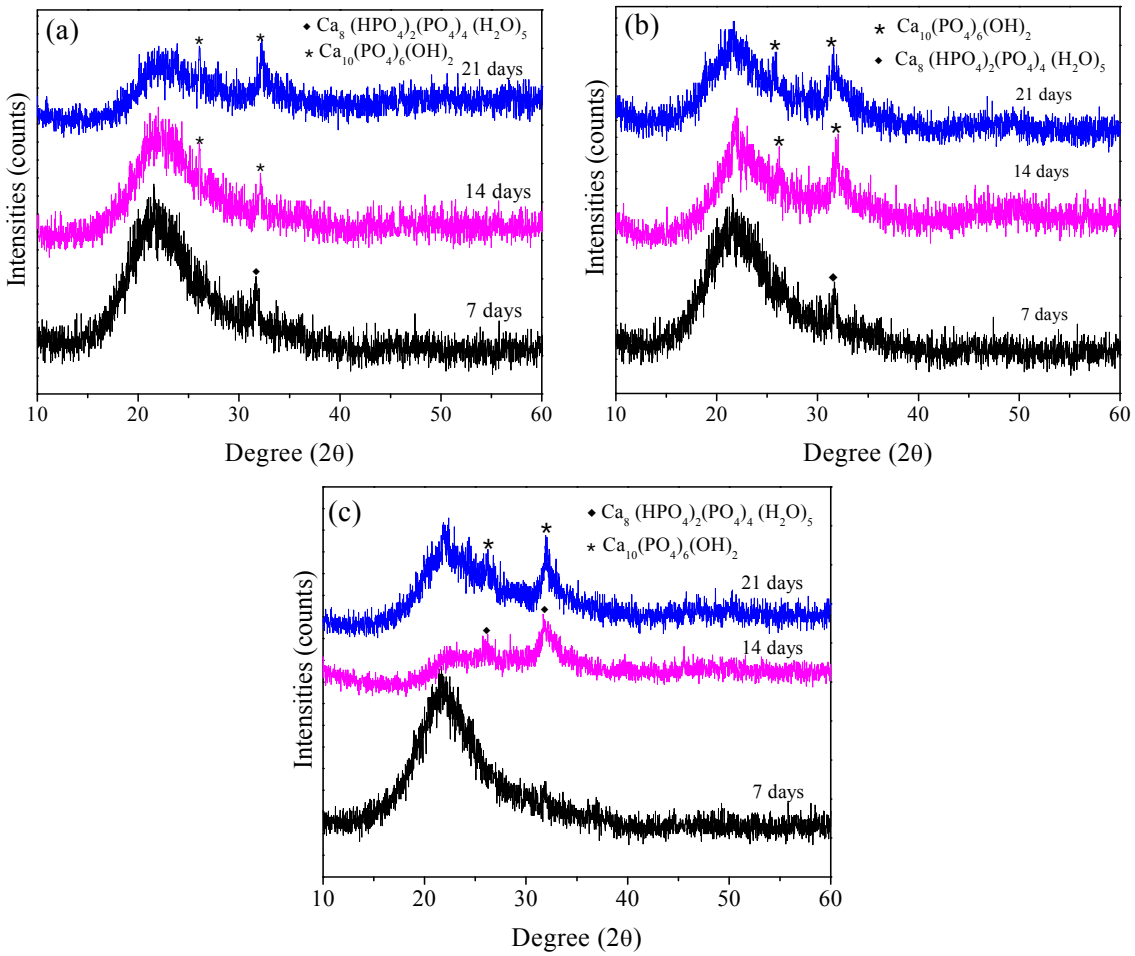

Fig. 4.14 XRD patterns of the silica ceramics after SBF incubation for different days; (a) BA (sintered at 900 ^{o}C), (b) SG (sintered at 1100 ^{o}C) and (c) WA (sintered at 1200 ^{o}C).

The mechanisms of apatite formation in silica-based bioceramics are more or less similar with minor differences to that of glass and glass-ceramics [14, 15]. The accepted mechanism for glass is the dissolution of Na^{+} and Ca^{+2} ions from glassy matrix by exchange with protons from the solution. Whereas, the mechanism for amorphous silica is believed to be the formation of Si-OH functional group on the surface due to the hydration and dissolution of silica network. Hydrolysis of silica network leads to the release of soluble $Si(OH)_4$ into the body fluid. Simultaneously, Si-OH groups are formed at the solid-fluid interface. This group provides favorable sites for apatite nucleation [16]. Once nucleated, the apatite can grow spontaneously as the body fluid is highly supersaturated with respect to apatite under normal condition. The mechanism of apatite formation on silica ceramics has been shown schematically in Fig. 4.15 following the model proposed by Vallet-Regi et al [17].

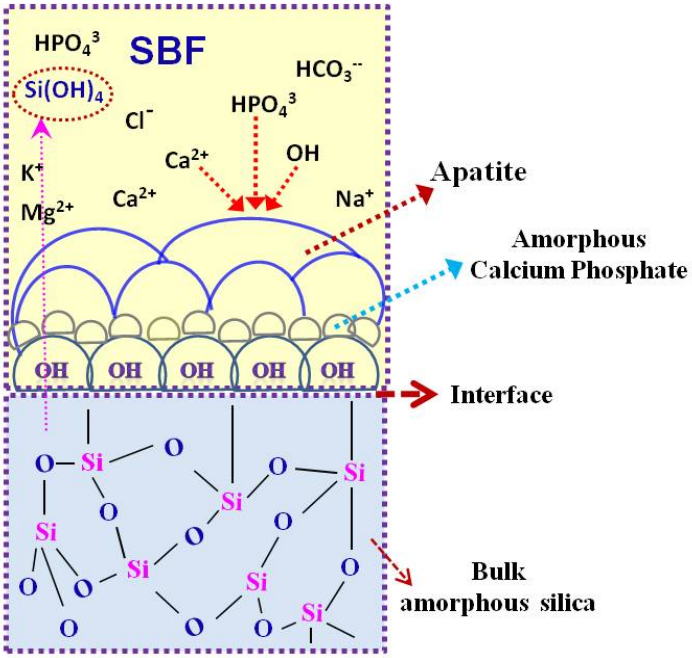

Fig. 4.15 Schematic diagram representing the events take place at the interface between amorphous silica ceramics and SBF [17].

The greater bioactivity of BA and SG may be correlated with their easy hydrolysis. BA has about 4% impurities cations like Ca^{+2} and K^{+}, which act as network modifiers in amorphous silica. In case of SG, the hydrolysis may be easier due to its inherent gel history. Gel material has surface silanol groups, which cannot be removed completely by heat treatment of gel below 1200 ^{o}C [18]. SG has been sintered at 1100 ^{o}C.

So the surface silanol group may be present in sintered SG specimen, which facilitates its hydrolysis. Slow response of WA may be due to its very low impurity content and high temperature heat treatment (1200 ^{o}C) of the ceramics.

4.2.2.6.2 Microstructural Analysis

Fig. 4.16 shows the microstructure and energy dispersive spectroscopy of the BA, SG and WA ceramics surface after immersion in SBF for 14 and 21 days. Deposited HAp layer shows typical cauliflower like microstructure in all cases. All 21 days specimens (Fig. 4.16 (b, d & f)) show higher surface area coverage with HAp compared to 14 days (Fig. 4.16 (a, c & e)). EDS spectra shows lower amount of Si in 21 days specimen compared to that in 14 days specimen for all cases. This is due to the deposition of higher amount of HAp in 21 days. EDS spectra for all also show the presence of Na, Mg and Cl, because these ions were present in the body fluid.

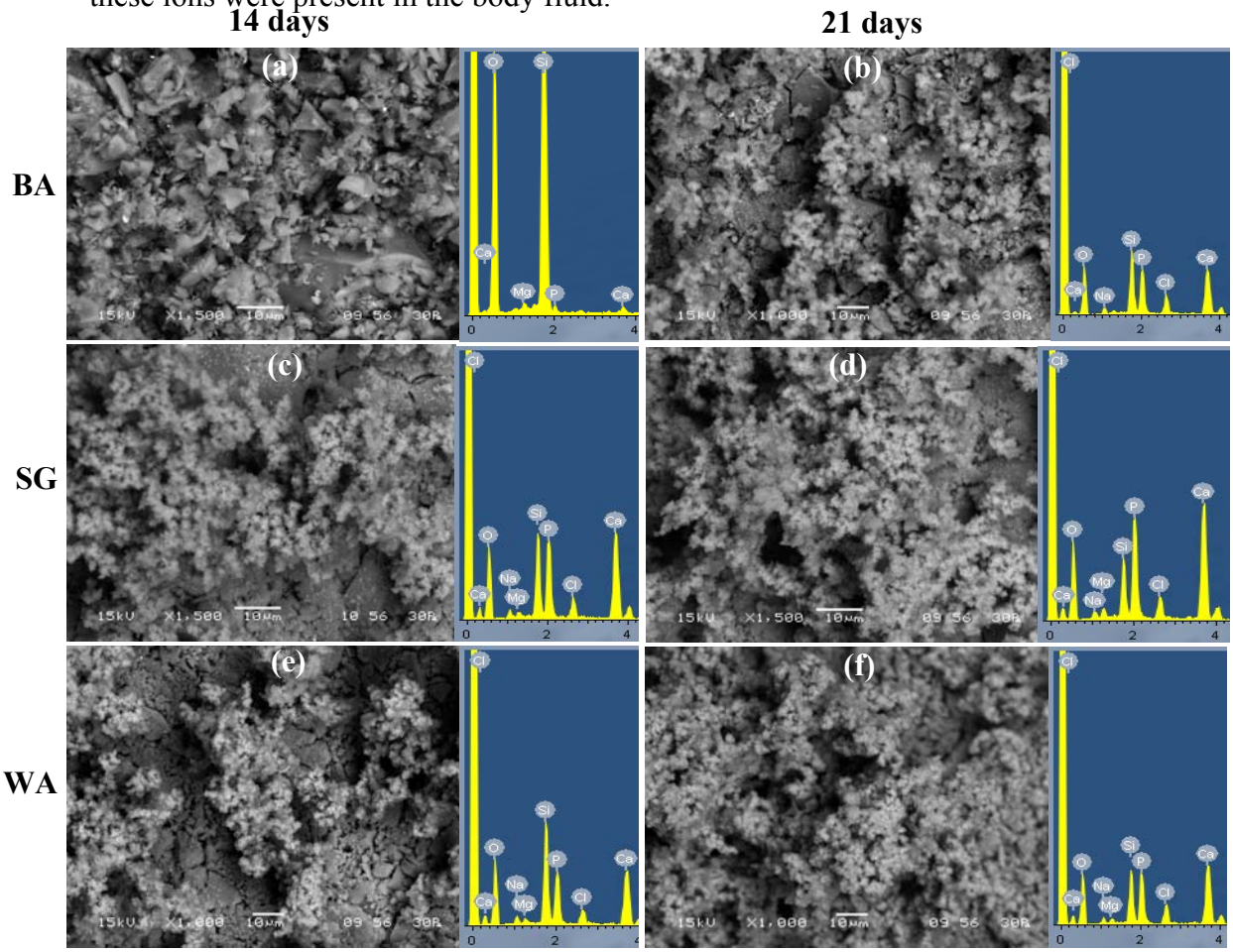

Fig. 4.16 SEM images and EDS spectra of BA (a-b), SG (c-d) and WA (e-f) surfaces after incubation in SBF for 14 and 21 days respectively.

4.2.2.7 *In vitro* Biodegradability

Degradation of bioceramics in body fluid is another important characteristic for its practical clinical applications. Fig. 4.17 (a) and (b) shows the change in Si concentration and pH in TRIS buffer solution respectively with incubation time. Si concentration increases as well as pH decreases with increasing time. It is known that silica dissolves into body fluids as silicic acid. For that reason, pH decreases. Silica network dissolution was rapid up to about 6 hours. After which, the rate decreased due to the saturation of medium with respect to silicic acid. BA ceramics shows a faster dissolution than other two ceramics due to its higher impurity content as stated earlier. Presence of other cations inside silica network facilitates the hydrolysis of silica. Network modifier cations dissolve quickly and thus open up silica network for its dissolution. Silica dissolution of WA was lowest due to its lower impurity content.

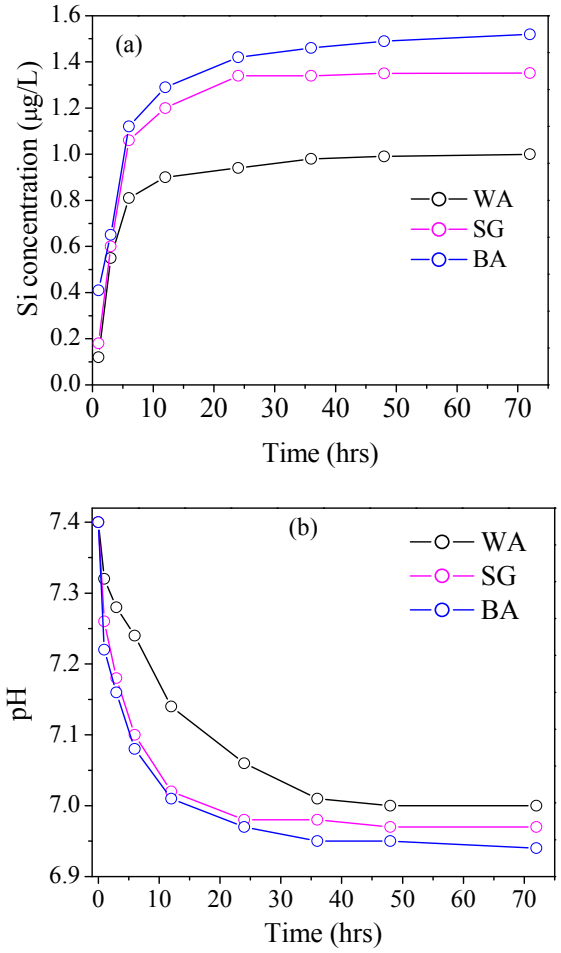

Fig. 4.17 (a) Change of silicon concentration and (b) pH in TRIS medium with incubation time.

4.2.3. Summary

In summary, amorphous silica ceramics were prepared using rice husk ash as a raw material. The effects of sintering temperature on the phase formation of silica and mechanical properties of the ceramics were investigated. During sintering, amorphous silica transformed mainly into cristobalite phase at 1000, 1200, and 1300 ^{o}C, respectively, for BA, SG, and WA ceramics. The phase transformation temperatures were different due to their differences in impurity content. The lowest temperature for BA was due to its highest impurity content. Densification rate of all specimens decreased above crystallization temperature. An anomaly in the increase in strength with sintering temperature was found, showing a fall in strength as and when amorphous silica transformed to cristobalite. Microstructural investigation revealed that the fall in strength was due to the crack formation by the high-low displacive phase transformation of cristobalite.

In vitro bioactivity test showed the formation of apatite layer on silica specimen surface. Biodegradability test showed a substantial dissolution of silica network within six hours. The rate of silica network dissolution and apatite phase formation was dependent on impurity cation content in amorphous silica which was inherited from husk composition. Among all these silica ceramics, SG showed highest mechanical strength along with good *in vitro* bioactivity and biodegradability characteristics. All these results suggest that the rice husk ash and/or silica gel prepared from rice husk are promising low cost raw material for the preparation of bioactive amorphous silica ceramics.

4.3. Silica-based Scaffold Prepared by Sponge Replication Technique

4.3.1. Introduction

Highly porous amorphous silica scaffolds were prepared using brown ash, white ash and silica gel powders through polymer sponge replication technique. Before slurry preparation, each powder was characterized for its particle size distribution. Zeta-potential and sedimentation behaviour of powders were also measured. Slurries with 40 wt.% solid loading were prepared using PVA binder in aqueous solution. Rheological properties of slurries were evaluated before impregnating it into sponge template. Impregnated sponge cubes were dried at room temperature and sintered at different temperatures. Sintered reticulated porous ceramics (RPCs) were characterized for their porosity, mechanical properties and bioactivity.

4.3.2. Results and Discussion

4.3.2.1 Particle Size Distribution

Fig. 4.18 shows the particle size distribution of BA, WA, and SG powders which was used for scaffold preparation. Powders show unimodal particle size distribution with an average size (d_{50}) of 13, 11 and 8 μm for BA, WA and SG respectively. These powders were used to make slurry for sponge impregnation.

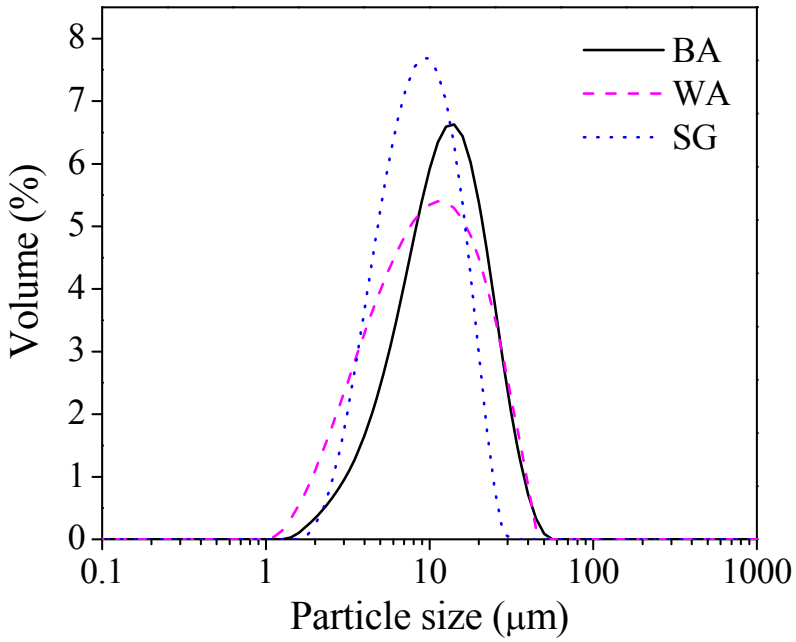

Fig. 4.18 Particle size distribution of different silica powders.

4.3.2.2 Zeta-potential

Zeta (ζ)-potential becomes important for understanding the dispersability of ceramic particles in water medium. The change of ζ-potential with pH is presented in Fig. 4. 19. All particles develop negative surface charges in the pH range >2 to 12. The isoelectric point is around pH 2. This behaviour is in accord with that reported by Sacks [19] for silica suspensions. When silica powder is dispersed in water, the surface layer of silica is hydrated to form silanols (Si-OH). Since silanols are relatively acidic, they undergo base reaction upon increasing pH resulting in the development of negative surface charges as per reaction:

$$Si\text{-}OH + OH^- \text{---------} Si\text{-}O^- + H_2O \qquad (4.1)$$

On increasing pH, the particles develop higher surface charges due to the formation of more $Si\text{-}O^-$ groups and hence, ζ-potential increases.

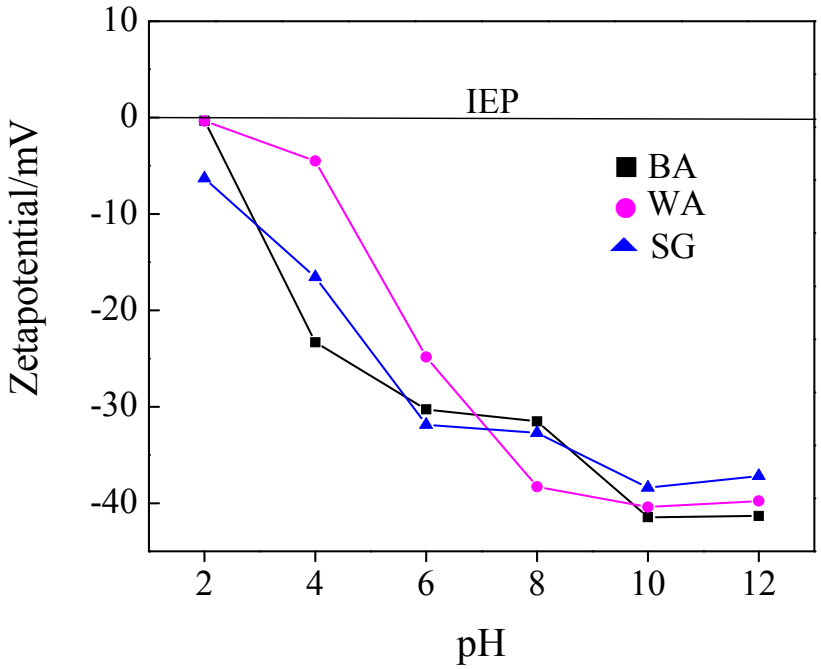

Fig. 4.19 Zeta potential of different silica powders with respect to pH.

4.3.2.3 Sedimentation Behaviour

The sedimentation behaviour of different powders as a function of pH is plotted in Fig. 4.20. Sedimentation height of each suspension decreased with increasing pH. The dispersion is more stabilized against sedimentation with increase in pH. Stabilization occurred due to the increase in electrical double layer thickness of particles with

increasing pH. Near pH 2, the sedimentation amount of BA was higher than others. This may be due to the presence of cationic impurities in BA [20]. The cationic impurities have significant impact on the coagulation behaviour of silica [21]. Sedimentation heights of all were minimum around pH 10. This is due to the maximum ζ-potential around pH 10 as shown in Fig. 4.19. Thus, high stabilization of silica dispersion around pH 10 is attributed to the increased ζ-potential. All the slurries for sponge impregnation were prepared at pH 10.

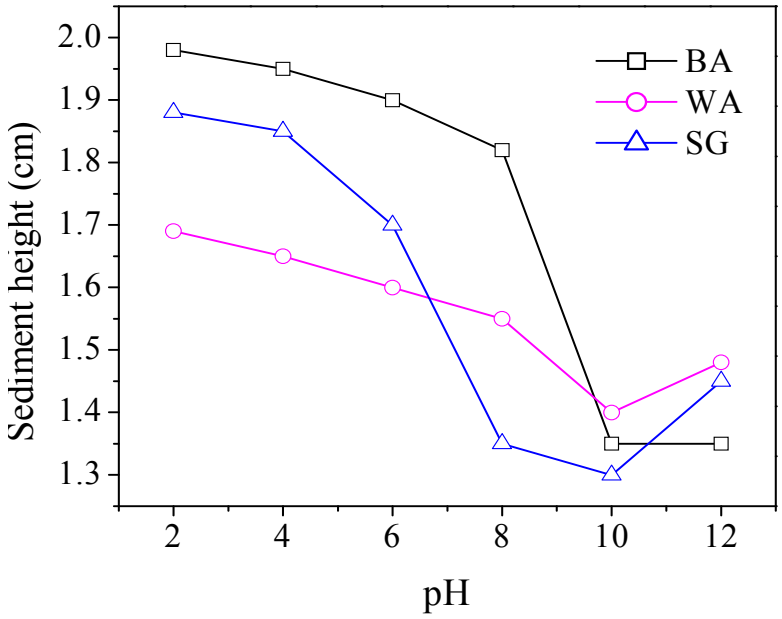

Fig. 4.20 Sedimentation heights as a function of pH for silica powders.

4.3.2.4 Slurry Rheology

Slurry rheology is very important for easy filling into pores of template and its retention inside the pores. Fig. 4.21 shows the response of slurry viscosity and shear stress with changes of shear rate. In each case, viscosity decreased with increasing shear rate and vice versa as shown in Fig. 4.21 (a). The slurries exhibit a thixotropic behaviour as evidenced by a hysteresis between the ascending and descending curves. Fig. 4.21 (b) illustrates these shear thinning behaviour [22] of the slurries. The slurry used for polymeric sponge impregnation should be fluid enough to enter, fill and coat the sponge webs and then must be thick enough to be retained inside. This kind of characteristics is provided by the thixotropic slurry. So, these slurries were used for impregnating the

sponge cubes. Fig. 4.22 shows the BA-slurry impregnated dry sponge cube and Fig. 4.23 shows SG-slurry impregnated green and fired cube.

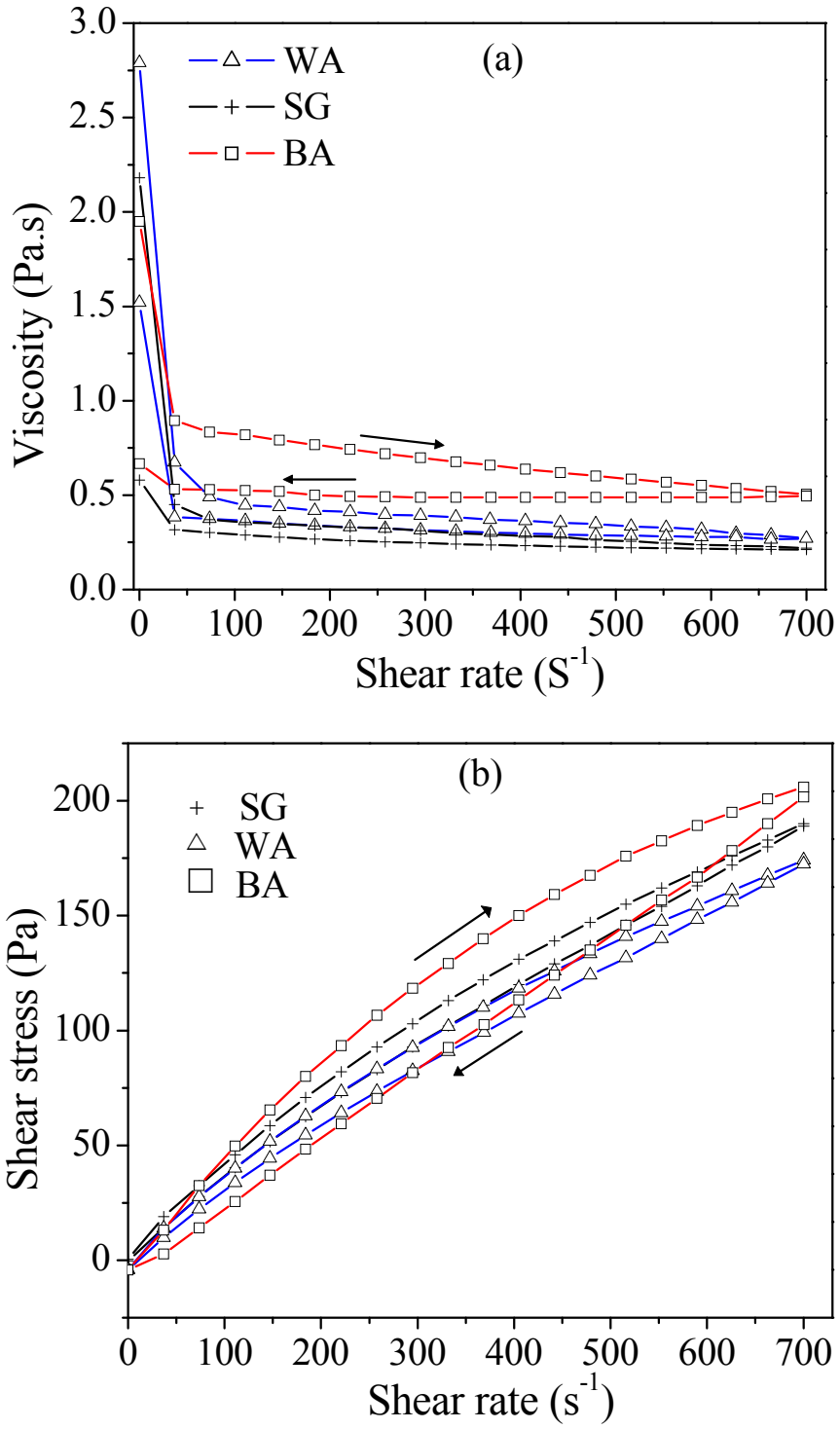

Fig. 4.21 Rheological behaviors of different silica slurries; (a) shear rate vs. viscosity (b) shear rate vs. shear stress.

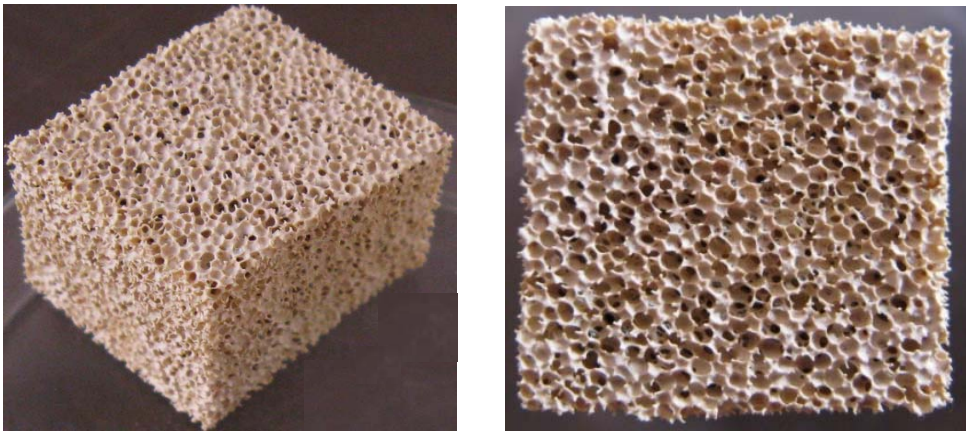

Fig. 4.22 BA-slurry impregnated dry sponge cubes.

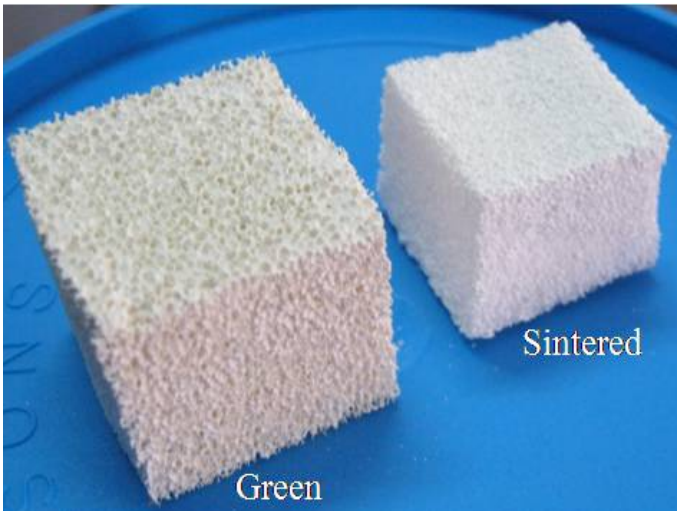

Fig. 4.23 SG-slurry green and sintered sponge cubes.

4.3.2.5 Thermal Decomposition Behavior of Impregnated Sponge

Pyrolysis of sponge polymer material is very important during thermal processing in this method. Sufficient time should be given for the polymer burnout before the sintering of ceramics to avoid cracks. TGA was used to determine the temperature at which the complete burnout of the polyurethane foam occurred. Fig. 4.24 shows the weight change of impregnated sponge with temperature. It shows that the weight losses are complete within 550 ^{o}C. Thus, to allow ample time for the complete burnout of the polymer during thermal processing, the initial heating rate was 1 ^{o}C/min up to 600 ^{o}C with a dwell time of 2 h at 600 ^{o}C and then sintering was carried out at different temperatures.

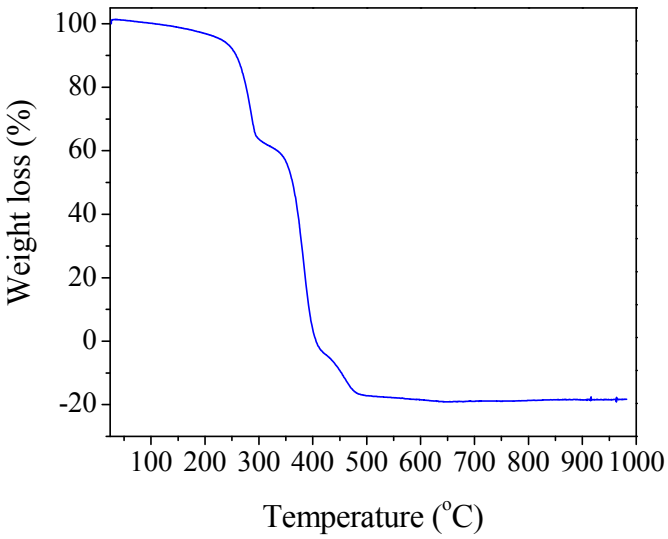

Fig. 4.24 Weight losses as a function of temperature (heating rate@10 °C/min) for impregnated sponge.

4.3.2.6 Mechanical Property

Fig. 4.25 shows the effect of sintering temperature on porosity of different RPCs. It shows that porosity decreases with increasing sintering temperature. It is quite obvious that on increasing sintering temperature, porosity decreases. The porosity of sintered body varies from 85 to 93% for BA, 86 to 90% for WA and 76 to 81% for SG based RPC. Porosity decreases due to classical sintering phenomena, which is discussed in details in section 4.2.2.4.

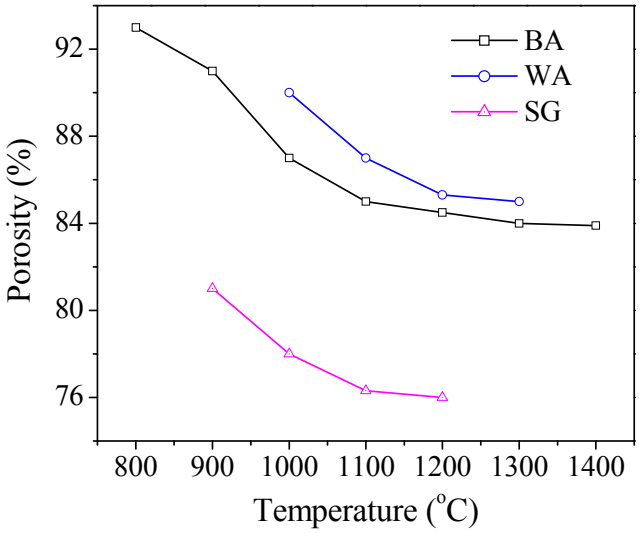

Fig. 4.25 Effect of sintering temperature on porosity of different RPCs.

Room temperature compressive strengths of specimen sintered at different temperatures are shown in Fig. 4.26. Compressive strength increased upto a specific sintering temperature for each case. These specific sintering temperatures were 1100, 1200, and 1300 ^{o}C for SG, WA, and BA respectively. At a particular temperature, strength of all silica body decreased due to the crack formation as described in section 4.2.2.5 in details. At this particular temperature, crack is formed in the body due to high-low displacive phase transformation of cristobalite during cooling of sintered body. The compressive strength of SG RPC was higher compared to other two, apparently due to its lower porosity. Details about the increased strength of SG material have been discussed in section 4.2.2.5.

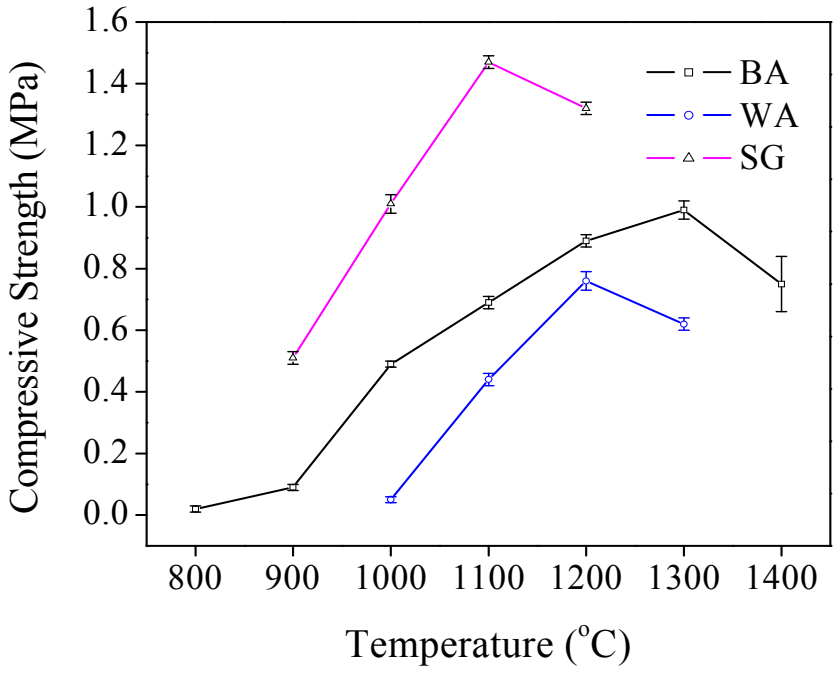

Fig. 4.26 Effect of sintering temperature on compressive strength of the RPCs.

The stress-strain behavior of porous SG ceramics (in compression) is shown in Fig. 4.27. The specimen was sintered at 1100 ^{o}C and was having 76 % porosity. It showed a compressive strength of 1.47 ± 0.1MPa. The stresses and strains were calculated from the initial cross-sectional area and length. The response showed a linear elastic behavior during the initial compression, followed by a decrease in stress, possibly due to the fracture of some struts in the solid network. The peaks and valleys in the curve may be related to progressive breaking of the solid particulate network. As the strain

increased, the additional struts were fractured. Finally, the failure occurred due to the propagation of crack. Such kind of stress-strain behaviour of RPC was also reported by Gibson et al [23] and Fu et al [24].

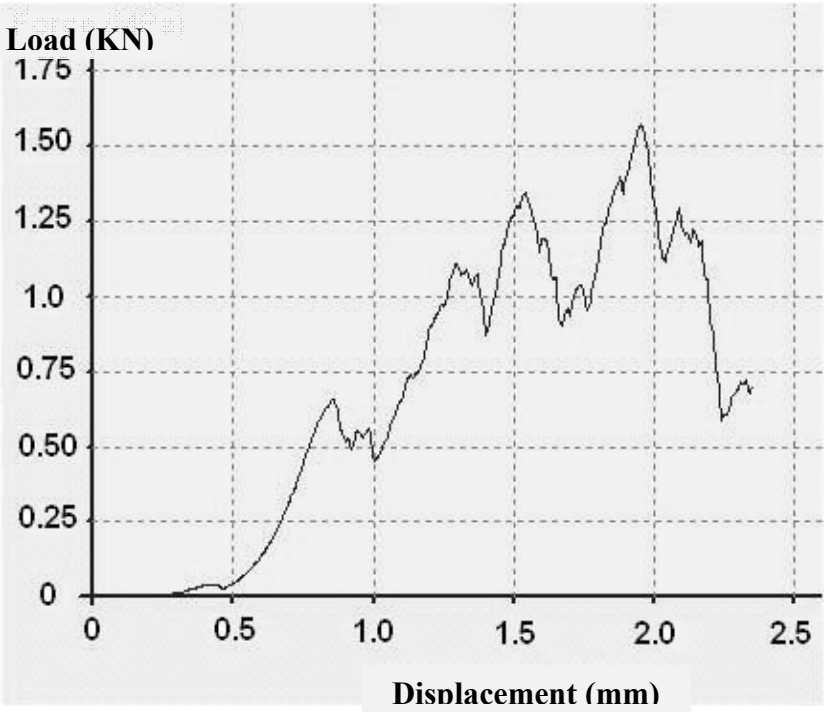

Fig. 4.27 Compressive stress-strain curve of the SG based RPC.

4.3.2.7 *In vitro* Bioactivity

4.3.2.7.1 Phase Analysis

SG scaffold, sintered at 1100 ^{o}C was used for bioactivity test as the scaffold showed best mechanical strength among all. Fig. 4.28 shows the X-ray diffraction patterns of SG scaffold surface with and without SBF incubation. The halo, centered at ~22^{o} (2θ) was due to the nature of amorphous silica based material (Fig. 4.28 (a)). SBF incubated specimen (Fig. 4.28 (b)) shows two extra peaks at 26 and 32^{o} (2θ). These peaks were identified to match with hydroxycarbonate apatite; HCA, $Ca_{10}(PO_4)_3(CO_3)_3(OH)_2$ phase. HCA was formed in the specimen after incubation in SBF for 8 weeks.

The mechanism of apatite formation in amorphous silica is believed to be the formation of Si-OH functional group on the surface due to the hydration and dissolution of silica network. Hydrolysis of silica network leads to the release of soluble $Si(OH)_4$ into

the body fluid. Simultaneously, Si-OH groups are formed at the solid-fluid interface. This group provides favorable sites for apatite nucleation and the phenomena have been discussed in earlier section 4.2.2.6.

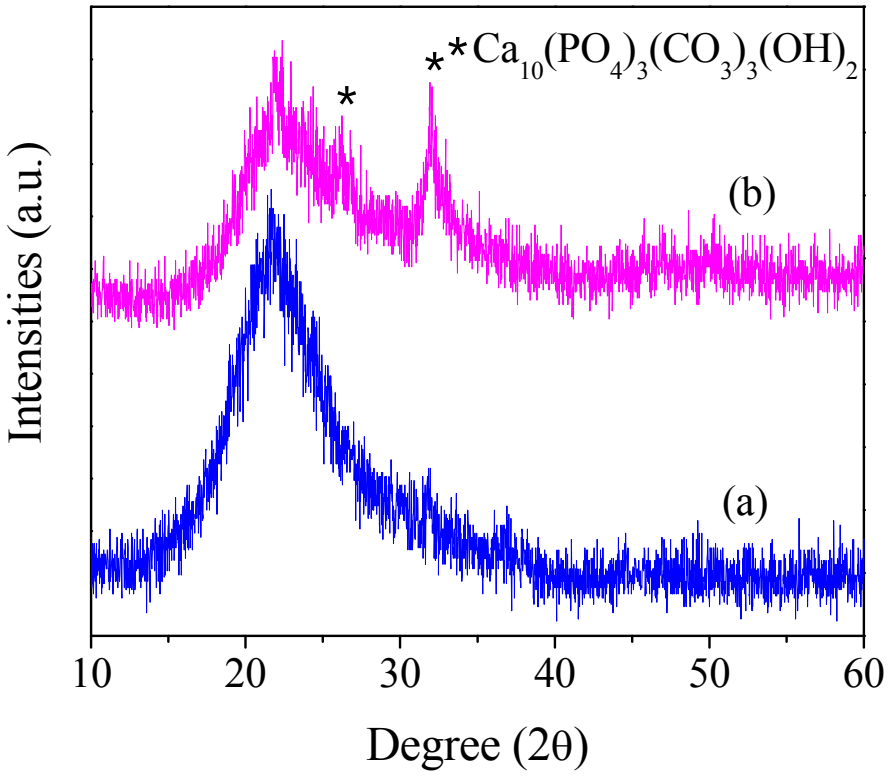

Fig. 4.28 XRD patterns of SG scaffold (a) without and (b) with SBF treatment.

4.3.2.7.2 Microstructural Analysis

Fig. 4.29 shows the microstructure and EDS spectra of SG scaffold after incubation in SBF for 8 weeks. The microstructure (Fig. 4.29 (a)) of the SG scaffold shows open and interconnected pores with well thickened struts. Carbonated hydroxyl apatite grows over the strut boundary and also on the concave surface of the scaffold (Fig. 4.29 (b)). The deposited apatite morphology shows sponge-wig type structure (Fig. 4.26 (c, d and e)). Corresponding EDS confirmed the deposition is carbonated hydroxyapatite. EDS also shows the presence of Na, Mg and Cl, because these ions were present in the body fluid.

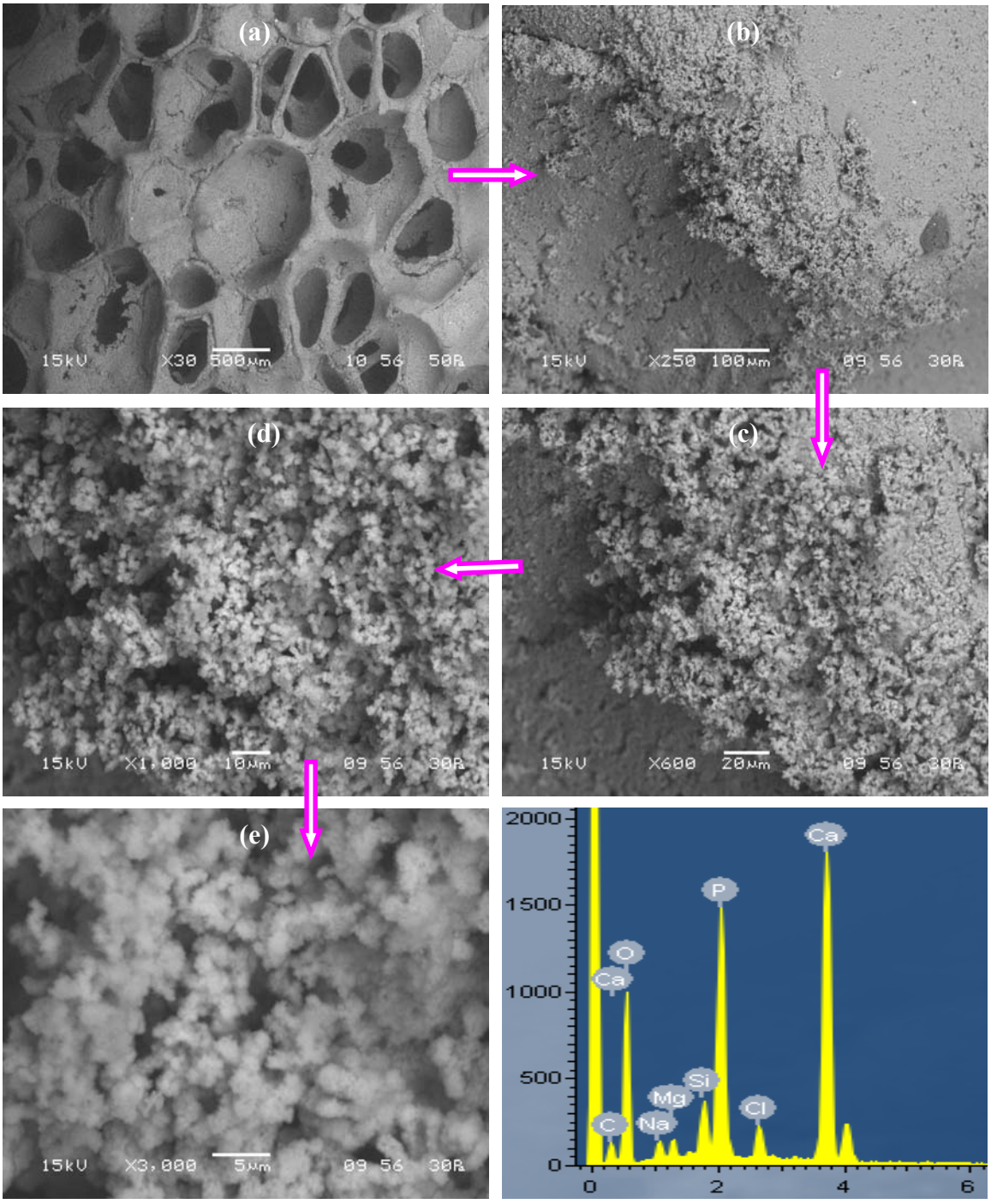

Fig. 4.29 SEM micrographs and EDS graph of SG scaffold with (a) open and inter connected pores and (b, c, d, e) deposited carbonated HAp on strut boundary with sponge-wig like structure.

4.3.3. Summary

Amorphous silica based scaffold was prepared using rice husk ash and silica gel powder. Scaffolds were fabricated by slurry impregnation process using polymeric sponge as the replica. The aqueous slurry with 40 wt.% solid loading showed a thixotropic behaviour in presence of PVA binder. The sintering temperature showed a strong effect on the porosity and mechanical strength development of scaffolds. The strength of scaffold decreased above a sintering temperature where the amorphous silica transformed into cristobalite. The SG scaffold, with a porosity of 76.0 %, showed good mechanical strength of 1.47 ± 0.1MPa. *In vitro* bioactivity test in SBF showed the formation of apatite layer on silica scaffold surface. All these results suggest that the rice husk ash is a promising low cost raw material for the preparation of amorphous silica scaffold.

4.4. Porous Silica Ceramics Prepared by Gelcasting

4.4.1. Introduction

Silica gel powder was prepared utilizing rice husk ash produced as a waste in boiler heating plant of a local rice mill. The gel powder was used to fabricate porous ceramics through gelcasting technique. Slurry for gel casting was prepared with 42 vol.% solid loading in Acrylamide (AM) monomer and Methylene-Bisacrylamide (MBAM) cross-linker premix solution. Gelation time of the slurry was optimized by using different ratio of MBAM:AM premix solutions. Gel powder dispersed in premix solution was characterized for its zeta-potential and sedimentation behaviour. Rheological property of the slurry was studied. Gelcasting process was carried out at room temperature and cylindrical shapes of specimens were gelcasted without any damage of their shapes. Different complex shapes were machined out from green body. Thermal decomposition and sintering behaviour of the specimen were studied. Sintered shapes were analyzed for their phase formation, porosity, mechanical strength and bioactivity.

4.4.2. Results and Discussion

4.4.2.1 Zeta-potential

Before slurry preparation, zeta-potential (ζ) of SG powder has been re-checked in the presence of the monomer: cross-linker. Fig. 4.30 shows the particle size distribution of SG powder which was used for gel-casting study. Unimodal and narrow particle size distribution with an average particle size of 9 μm was found for SG powder.

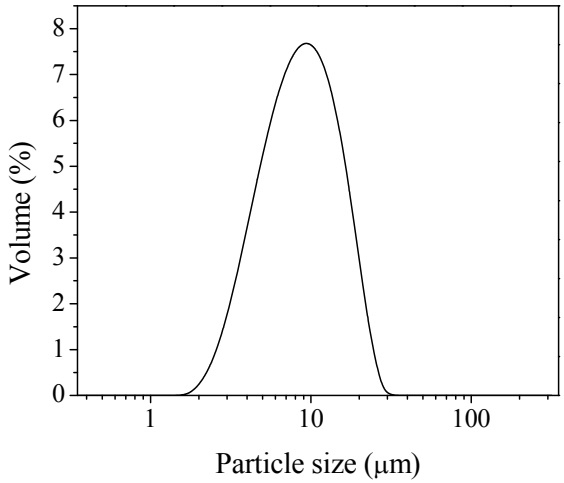

Fig. 4.30 Particle size distribution of silica gel powder.

ζ-potential of SG was measured by dispersing it in 1:30 premix solution. 1:30 premix solution was used for this measurement because this ratio of the monomer:cross-linker has been reported as optimum for many gelcasting system [25, 26]. The change of ζ-potential with pH is presented in Fig. 4.31. SG particles develop negative surface charges in the pH range >2 to 12 as described above. Maximum negative ζ-potential was obtained at pH 10. Results revealed that ζ-potential of SG show no changes in premix solution as compared to water suspension. As stated earlier, the surface layer of silica is hydrated to form silanols (Si-OH). Since, silanols are relatively acidic; it reacts with OH^- to form Si-O^- negative surface charges. This increased surface charge will help to stabilize the slurry with higher solid loading.

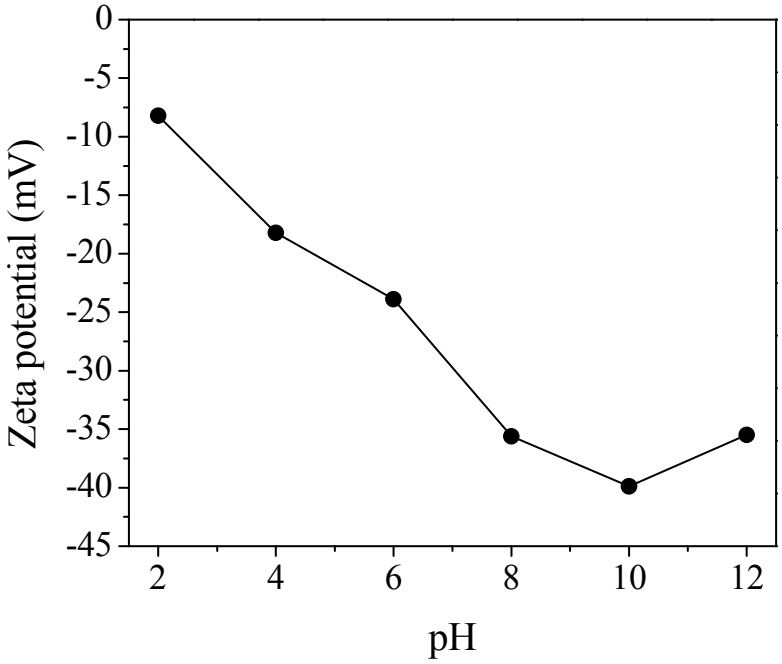

Fig. 4.31 Zeta potential of silica gel powder with pH measured in 1:30 premix solution.

4.4.2.2 Sedimentation

The sedimentation behaviour of SG particle was measured using a 20 wt.% solid loading in 1:30 premix solution. Fig. 4.32 shows the sedimentation heights measured as a function of pH. The height decreases with increasing pH up to around 10 and then slightly increases at pH 12. As described in section 4.3.2.3, the variation in sedimentation with pH is due to the different extents of agglomeration. Agglomeration decreases due to

the increase in electrical double layer thickness of particles with increasing pH. Sedimentation height was minimum around pH 10; this is due to the maximum ζ-potential, as shown in Fig. 4.31. So, SG slurry should be prepared at pH 10.

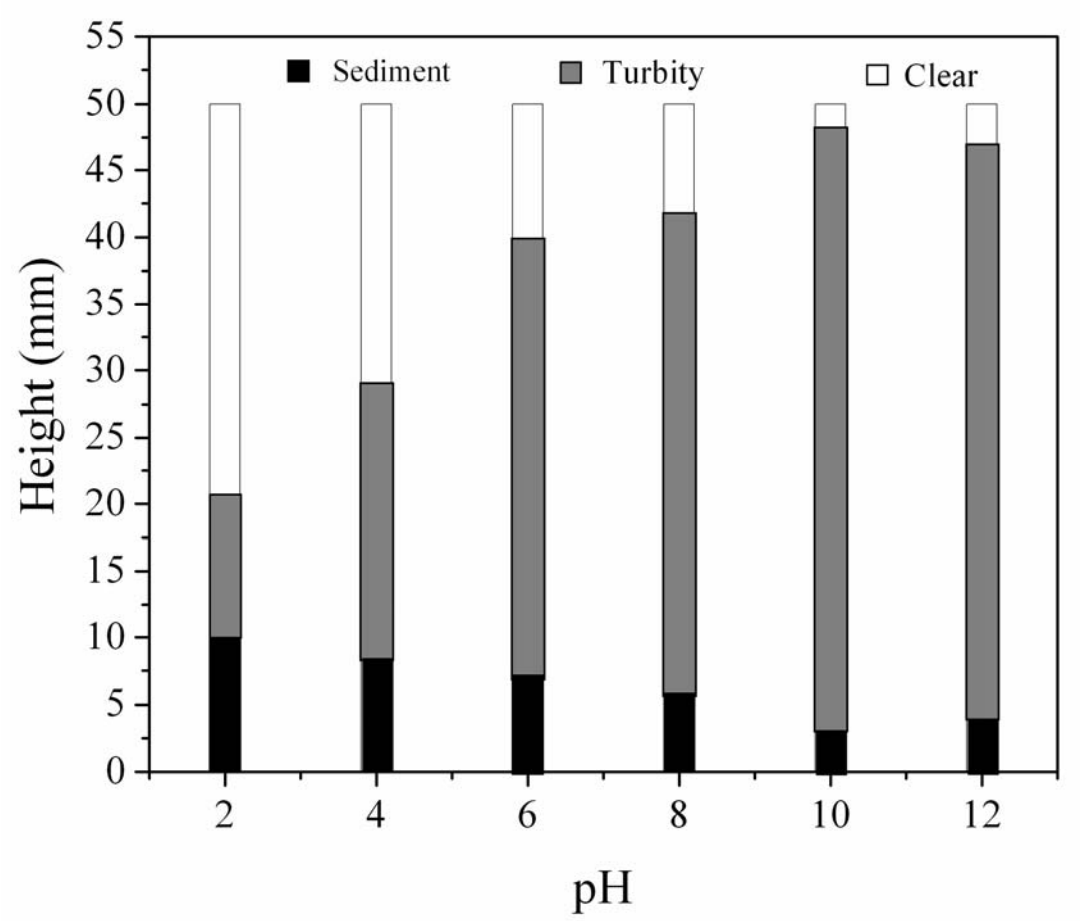

Fig. 4.32 Sedimentation behaviour measured after 72 h of SG particles at different pH when dispersed in 1:30 premix solution.

4.4.2.3 Gelation Time

The gelation process is one of the key steps of gelcasting. The gelation rate depends on polymerization rate of the organic monomer in the suspension. Generally, polymerization rate is related to the amount of initiator, concentration of monomer and temperature. Fig. 4.33 shows the variation of gelation time with initiator concentration for different monomer system. Gelling time of each monomer system (15 wt.% of powder) decreases with increasing initiator concentration. 1:6 ratio monomer system takes too little time for gelation compared to the other monomer system. 1:70 monomer system takes

comparatively longer time for gelation. Gelation time of 1:30 and 1:50 monomer system remains intermediate between the two extreme cases.

It is known that gelation time reduces rapidly with the increase in the initiator concentration. Initiator provides free radical to boost the polymerization reaction. A mixture of mono- and bifunctional unsaturated monomers polymerize in the presence of free radicals to form a network polymer. Initially, the initiator forms free radicals, and then it reacts with the monomer and forms free radicals of the monomer as well as initiates polymerization and boost the reaction. A catalyst may enhance the polymerization rate. In this study, the amount of catalyst (0.15 wt.% on powder basis) was fixed for all monomer system.

Fig. 4.33 also shows that a particular initiator concentration, gelation time decreases rapidly with the increase in the amount of cross linker (MBAM) in monomer system. Because, the radical attack is easier for more uncovered carbon atom of MBAM (which has at least two double bonds); than for AM (has a single double bond). Thus, the premix solution with 1:30 ratio of MBAM:AM was preferred for the gelcasting process.

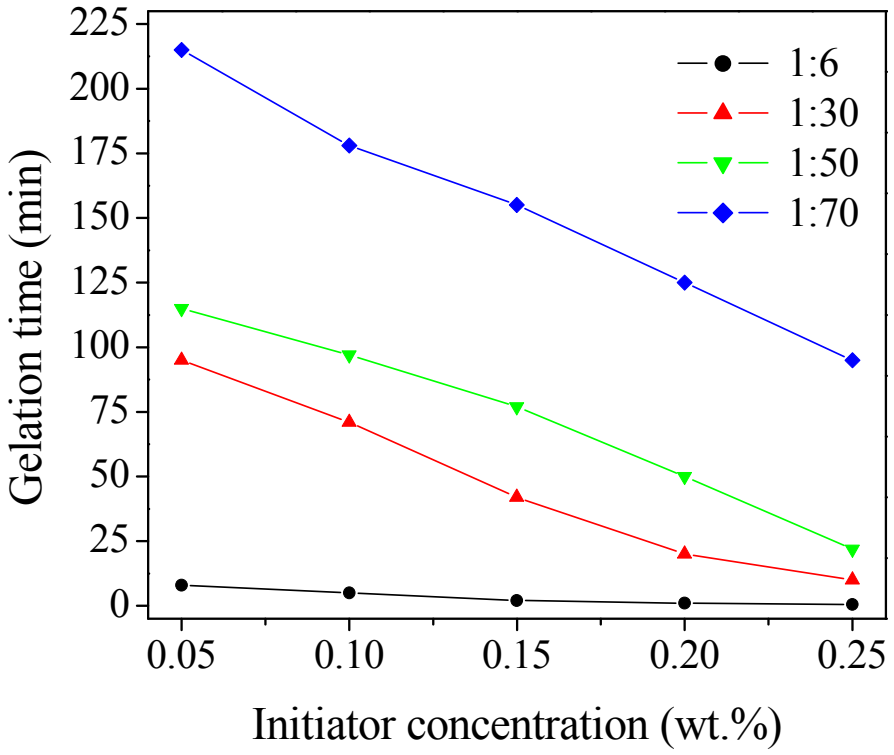

Fig. 4.33 Variation of gelation time with initiator concentration (slurry with 42 vol.% solid loading).

4.4.2.4 Slurry Rheology

Slurry with high solid loading and excellent fluidity is essential for gel casting process. Fig. 4.34 shows the optimized SG slurry that was used for gel casting. The slurry was prepared at pH 10 with 42 vol.% solid content in 1:30 premix solution. The rheological behaviour of the slurry is shown in Fig. 4.35. It is suggested that the slurry must have the thixotropic or shear thinning behaviour. The slurry exhibits such kind of thixotropic behaviour as evidenced by a hysteresis between the ascending and descending curves in Fig. 4.35.

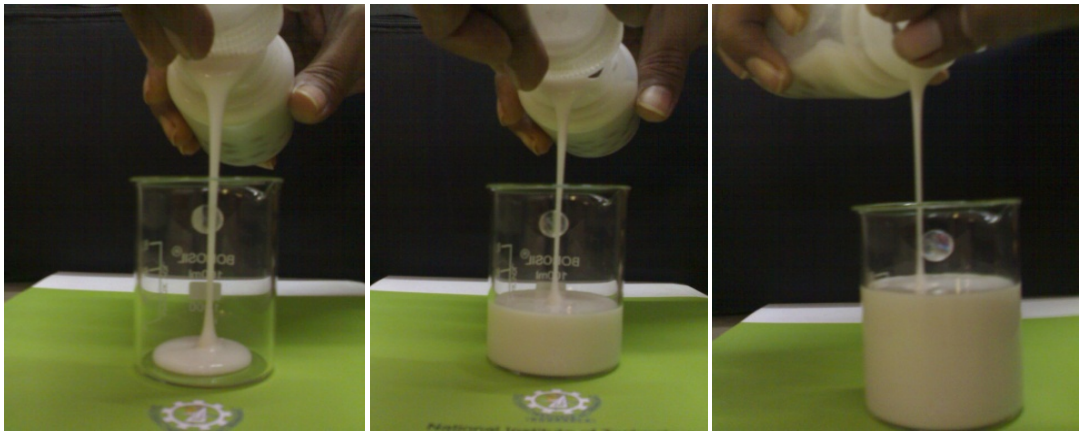

Fig. 4.34 Optimized silica gel slurry after preparation.

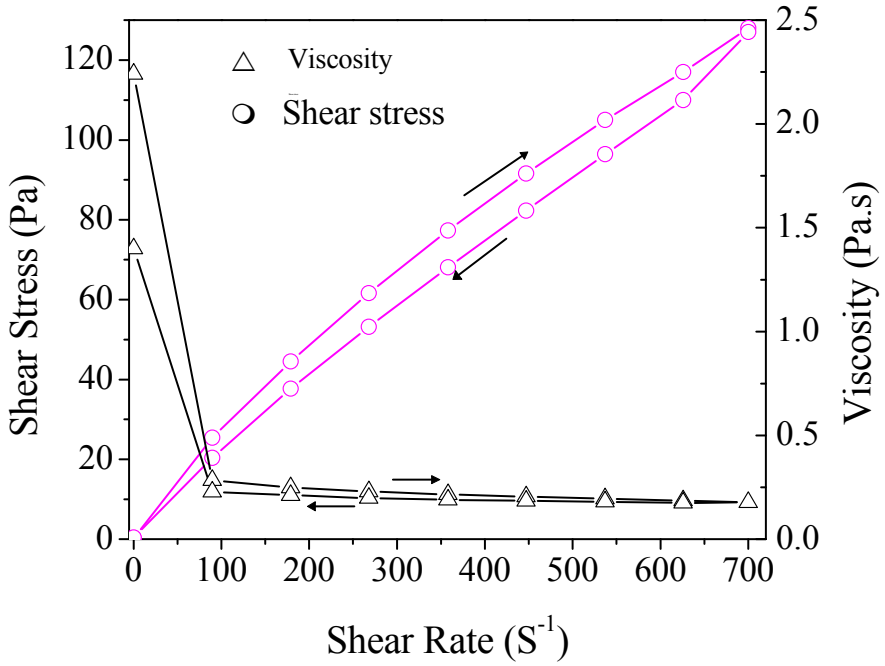

Fig. 4.35 Rheological behavior of the optimized slurry.

4.4.2.5 Thermal Decomposition Behaviour of gelcasted Body

Before a ceramic part can be sintered, the organic aids that are incorporated in the body during fabrication must be removed. Binder burn-out of green body was studied through TGA/DSC. Fig. 4.36 shows the TGA/DSC curve of gelcast body. The TGA curve shows a steady weight loss up to the temperature of 110 °C with an endotherm at ~100 ^{o}C in DSC due to the evaporation of physisorbed water. The major weight loss was observed in the temperature range 200-600 °C. This loss can be attributed due to the burning of polymer network of gel body. Two endotherms in DSC at ~280 and ~380 ^{o}C were due to the two stage decomposition of organic precursors. The weight loss occurs from the sample even after 600 ^{o}C onwards as shown in TGA curve, may be due to the removal of chemically bonded OH^- group remaining in the gel matrix [18]. Total weight loss was about 30%, out of which, ~ 5 wt.% was in the temperature range of 30 to 110 ^{o}C and ~ 20 wt.% was in 110 to 600 ^{o}C; and the rest 5% was from 600 ^{o}C onwards. Depending on this decomposition results, the gel-casted bodies were sintered with the heating schedule; from room temperature to 600 ^{o}C at a rate 1 ^{o}C/min followed by a soaking at 600 ^{o}C for 2hrs for organic burnout. Thereafter, the samples were heated at a rate 2°C/min to final sintering temperature 900-1200 °C with a soaking time of 2 h.

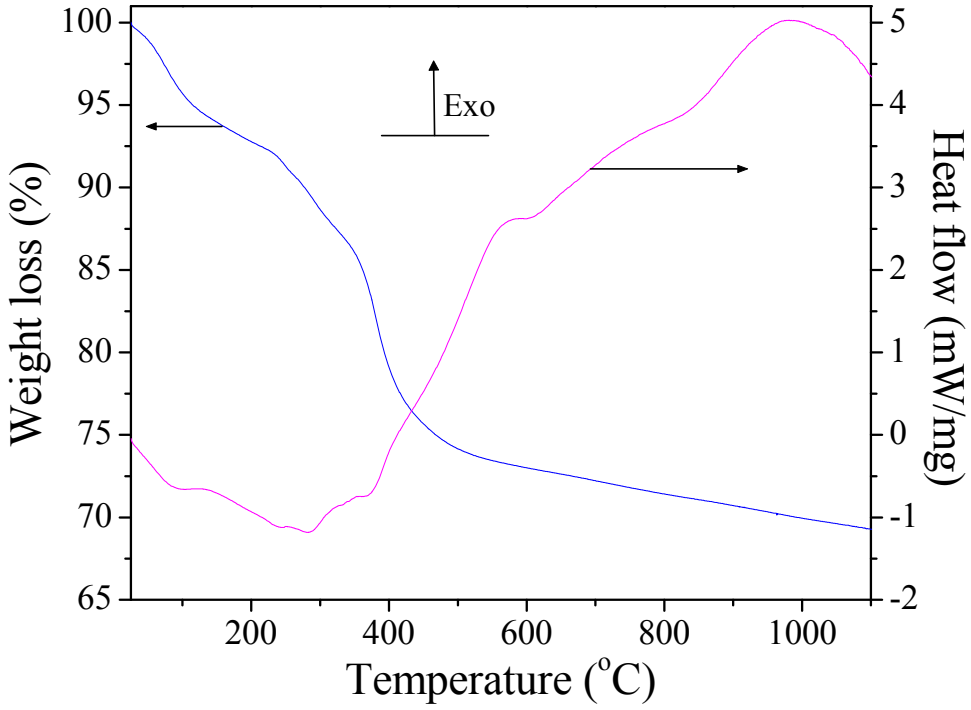

Fig. 4.36 TGA-DSC curves of gelcast body at a heating rate of 10 ^{o}C/min.

4.4.2.6 Mechanical Property

Fig. 4.37 shows the different shapes prepared by machining gel-casted SG bodies and after sintering. Fig. 4.38 shows the change of porosities and compressive strengths of specimen with sintering temperatures. The samples were sintered at temperatures ranging from 900 to 1200 ^{o}C. Porosity decreases gradually with increase in sintering temperature. It is evident that the strength increases significantly with the sintering temperature and reaches a maximum at 1100 ^{o}C showing the mechanical strength of ~ 27.5 MPa even though the body was having ~ 25% porosity. The strength decreased when the body was sintered at 1200 ^{o}C. Decreased strength above 1100 ^{o}C is due to the formation of cracks. Crack formation was due to the high to low displacive phase transformation of cristobalite and has been discussed earlier in section 4.2.2.5. Fig. 4.39 shows the XRD patterns of SG bodies sintered at 1100 and 1200 ^{o}C. As found earlier, the SG was amorphous at 1100 ^{o}C and crystalline cristobalite at 1200 ^{o}C. The details of phase transformations for amorphous silica of SG have been discussed in section 4.2.2.2. Fig. 4.40 shows the SEM microstructure of sintered specimen surfaces. 1200 ^{o}C specimen (Fig. 4.39) shows the presence of continuous cracks as stated above.

Fig. 4.37 Different sintered shapes prepared by machining gelcasted ingot.

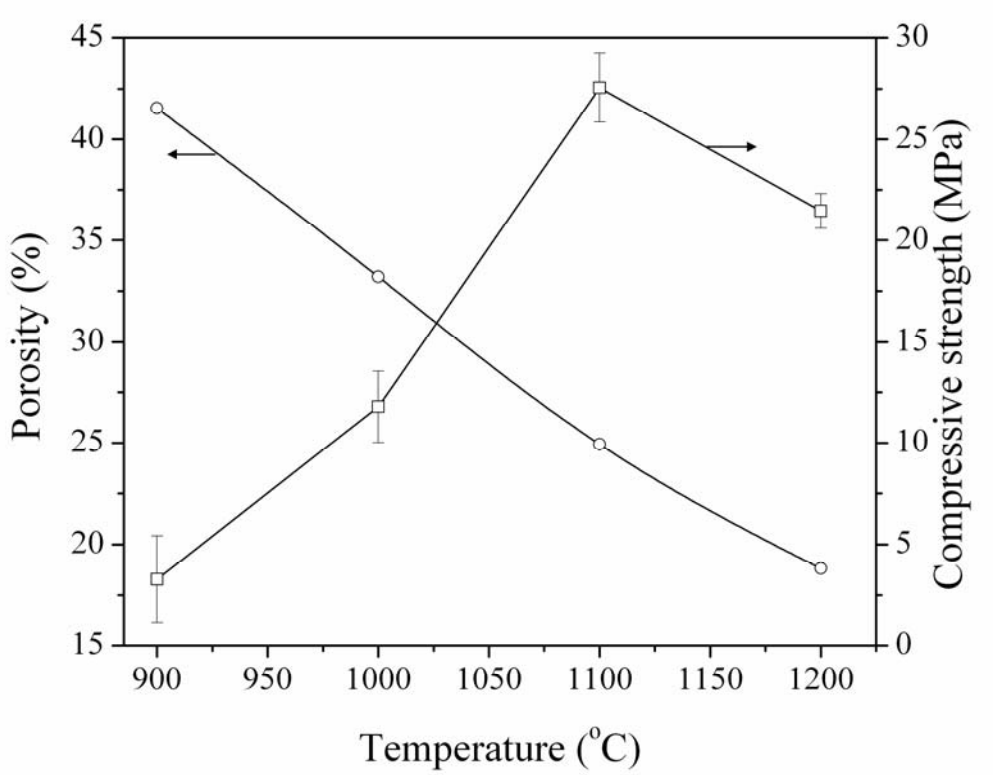

Fig. 4.38 Variation of porosity and compressive strength of gelcasted specimen with sintering temperature.

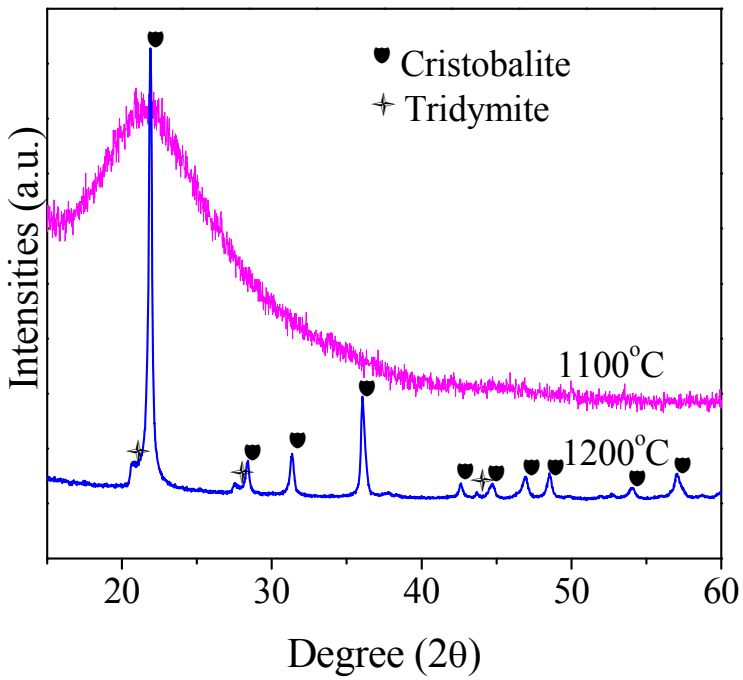

Fig. 4.39 XRD pattern of gelcasted SG-body after sintering at 1100 and 1200 °C.

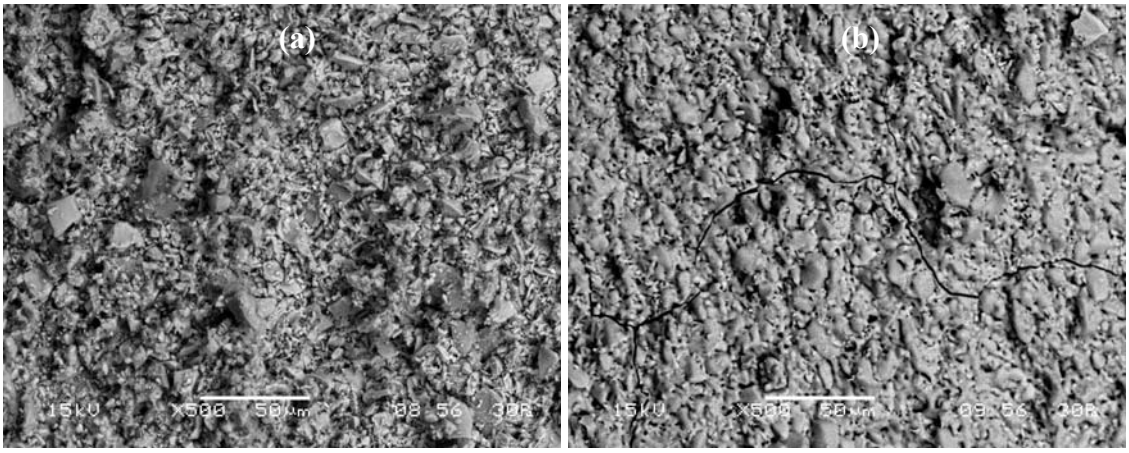

Fig. 4.40 Surface microstructure of a gelcasted SG pellet after sintering at (a) 1100, and (b) 1200 ^{o}C.

4.4.2.7 *In vitro* Bioactivity

4.4.2.7.1 Phase Analysis

Fig. 4.41 shows the X-ray diffraction patterns of sintered SG surface with and without SBF incubation. Fig. 4.41 (a) shows that the sintered SG is amorphous in nature. SBF incubated specimen (Fig. 4.41 (b)) shows extra peaks at 26 and 32^{o} (2θ). These peaks were identified to match with hydroxylcarbonate apatite; HCA, $Ca_{10}(PO_4)_3(CO_3)_3(OH)_2$ phase. This indicates, HCA was formed on the specimen surface during incubation in SBF for 4 weeks.

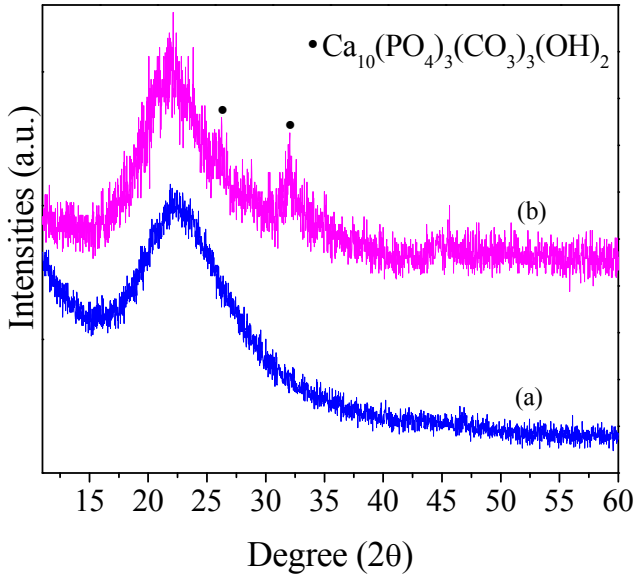

Fig. 4.41 XRD patterns of SG scaffold (a) without, and (b) with SBF incubation.

4.4.2.7.2 Microstructural Analysis

Bioactivity of gelcasted SG specimen was also evaluated by analyzing surface microstructure. Fig. 4.42 shows SEM micrographs and EDS graph of SG specimen after SBF incubation for 4 weeks. Deposited HAp has cauliflower like microstructure. EDS image shows typical Ca, P and Si, peaks along with C indicating carbonated HAp formation.

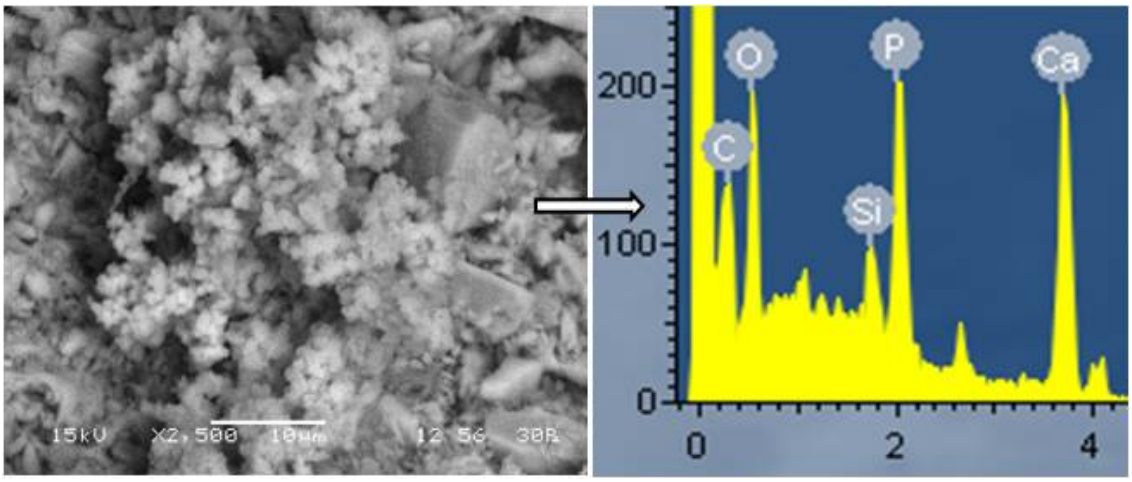

Fig. 4.42 SEM and EDS of SG surface after 28 days SBF incubation.

4.4.3. Summary

Amorphous silica-based porous bioactive ceramics was successfully prepared by gel casting method using silica gel powder derived from industrial rice husk ash. The slurry with 42 vol.% solid loading in 1:30 (MBAM:AM) monomer cross-linker solution, showed good thixotropic behaviour and generated a good casting. Casted body also showed good machinability. Sintered gel-casted body having ~25% porosity showed a mechanical strength of 27.5 ± 0.2 MPa. *In vitro* bioactivity experiment showed the formation of apatite layer on silica body. All these results suggest that the gel-casted SG-body can be used as bioceramics for different clinical applications.

4.5. Sol-gel Bioglass-Ceramics

4.5.1. Introduction

Soda-lime-silicate based glass-ceramics was synthesized through sol-gel route using RHA as silica precursor. The decomposition behavior of gel was evaluated. Gel powder was calcined to form glass-ceramics phases. Glass-ceramics powder was compacted to disk shape through uniaxial pressing. Disks were sintered at different temperatures ranging from 900 to 1050 ^{o}C. Mechanical properties of sintered specimen were measured and correlated with microstructural features. Both *in vitro* bioactivity and biodegradability of sintered material were investigated by incubating in simulated body fluid and TRIS buffer solution, respectively. Scanning electron microscopy, energy dispersive spectroscopy and X-ray diffraction were used to investigate the surface deposition after body fluid incubation.

4.5.2. Results and Discussion

4.5.2.1 Thermal Decomposition of Gel Powder

The thermal decomposition behavior of gel precursor was evaluated using TGA/DSC. Fig. 4.43 shows TGA/DSC curves of gel precursor. The decomposition may be divided into four different zones as shown in the figure. Zone I, extending up to ~150 °C, shows ~12% weight loss with a broad endothermic peak at 120 °C. Zone II (150-520 °C) shows an endothermic peak at 227 °C and a small weight loss (5%). Zone III (520-730 °C) shows a major weight loss of ~35% and four endothermic peaks at 580, 650, 690 and 720 °C respectively. There is very small or no weight loss in zone IV (730-1000 °C).

The decomposition behavior of gel precursor is used for the optimal synthesis of glass-ceramics. The gel is associated with two types of water namely physically and chemically bonded water. About 12% weight loss and associated endotherm at 120 °C (zone I, Fig. 4.43) are attributed to the loss of physically absorbed water from gel. A small weight loss in the zone II (150 to 520 °C) might be due to the loss of remaining portion of physically absorbed water. This zone shows an endothermic peak at 227 °C under which there is no weight loss. This may be due to the eutectic melting of $NaNO_3$-$Ca(NO_3)_2$ content of gel. Similar eutectic melting endotherm has been reported [27] for $NaNO_3$-$Ca(NO_3)_2$ at 232 °C. The major weight loss of 35% in zone III is due to the

decomposition of sodium and calcium nitrate as well as by the removal of chemically bonded water. The endothermic peaks at 580, 650, 690 and 720 °C may be attributed to the decomposition of $Ca(NO_3)_2$ [28] and $NaNO_3$ [29], which releases O_2, NO and N_2 gases during their decomposition. Decomposition of gel is further explained with the help of phase formation during heat treatment.

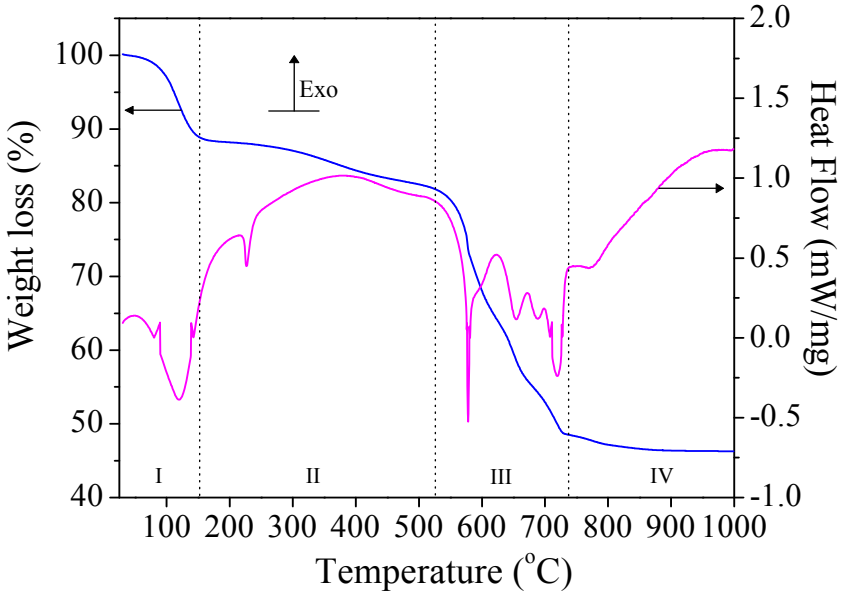

Fig. 4.43 DSC-TGA plot of soda-lime-silicate gel powder.

4.5.2.2 Phase Analysis

The phase formation behaviour during thermal decomposition and heat treatment of glass-ceramics precursors were investigated by XRD. Fig. 4.44 shows the XRD patterns of precursors after calcining at different temperatures. As prepared gel is completely amorphous (Fig. 4.44 (a)). However, $NaNO_3$ phase crystallizes upon heating the gel. Fig. 4.44 (b) shows well crystallized $NaNO_3$ phase on the specimen after heat treatment at 300 ^oC. The intensity of the $NaNO_3$ peaks decreases upon heat treatment above 500 ^oC (Fig. 4.44 (c)). Sodium calcium silicate phases were crystallized at and above 700 ^oC. Two phases; combeite-I, $Na_6Ca_3Si_6O_{18}$ (JCPDS 77-2189) and $Na_2Ca_2Si_2O_7$ (JCPDS 10-0016) are crystallized initially (Fig. 4.44 (d)). Finally, the major phase is combeite-I. Some amount of combeite-II, $Na_4Ca_4Si_6O_{18}$ was also detected in the specimen that was heat treated at 900 ^oC (Fig. 4.44 (e)).

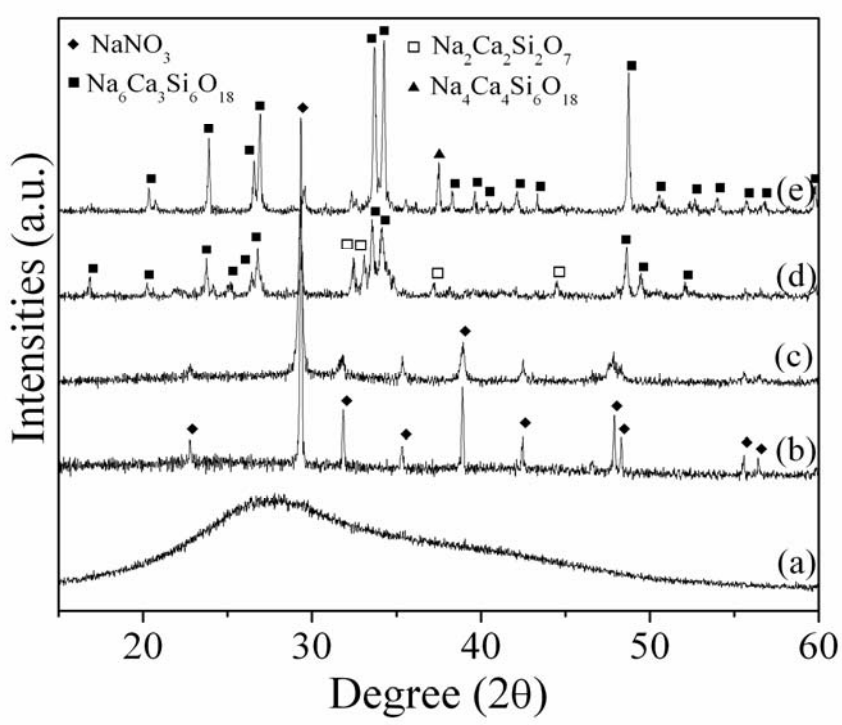

Fig. 4.44 XRD patterns of gel powder; (a) as prepared, and after calcination at (b) 300 (c) 500 (d) 700 and (e) 900 ^{o}C.

Decomposition of gel should be correlated with phase formation to optimize the processing parameters of glass-ceramics. By nature, the gel is amorphous. Gel contains a continuous network of solid and water. Upon heat treatment, crystallization of $NaNO_3$ occurs in the gel (Fig. 4.44 (b)). Similar crystallization has been reported in sol-gel glass upon heating above room temperature [30]. Then the amount of $NaNO_3$ decreases (Fig. 4.44 (c)), due to its partial decomposition at 500 ^{o}C. Dynamic decomposition of nitrates starts at around 530 ^{o}C (Fig. 4.43). Since the calcination was carried out in static condition at 500 ^{o}C for 2 h, some decomposition takes place. Nitrate decomposition completes upon calcination at 700 ^{o}C for 2 h (Fig. 4.44 (d)). Simultaneously, calcium and sodium react with silica to form different sodium calcium silicate phases. The major phase is $Na_6Ca_3Si_6O_{18}$, because, $NaO:CaO:SiO_2$ in the precursor is in ratio of 3 (Na_2O):3 (CaO):6 (SiO_2). Crystallinity of these ceramic phases increases when fired at 900 ^{o}C (Fig. 4.44 (e)) due to growth phenomena. It is evident that the crystallization of ceramic phases occurs mainly in zone IV of Fig. 4.43; in which the DSC curve shifts towards positive, that is, exothermic direction due to this crystallization.

The phase-formation behavior during sintering of glass-ceramics was also investigated. Fig. 4.45 shows the XRD patterns of pellets sintered at different temperatures along with pure and calcined gel powder. As mentioned above, as prepared gel is completely amorphous and combeite-I, and $Na_2Ca_2Si_2O_7$ are crystallized during calcinations at 700 ^oC (Fig. 4.45 (b)). Similarly, BGC900 specimen shows combeite-I and combeite- II phases (Fig. 4.45 (c)). It has been found that the combeite phase transforms into devrite; $Na_2Ca_3Si_6O_{16}$ (JCPDS 77- 0386), upon heat treatment above 900 ^oC. Semi-quantitative phase estimation shows about 58% devrite phase in BGC950 (Fig. 4.45 (d)). The devrite phase increases to74% in BGC1050 (Fig. 4.45 (f)). Remaining crystalline phases were combeite-I and II. It is to be noted that the diffraction patterns of combeite and devrite phases are very similar.

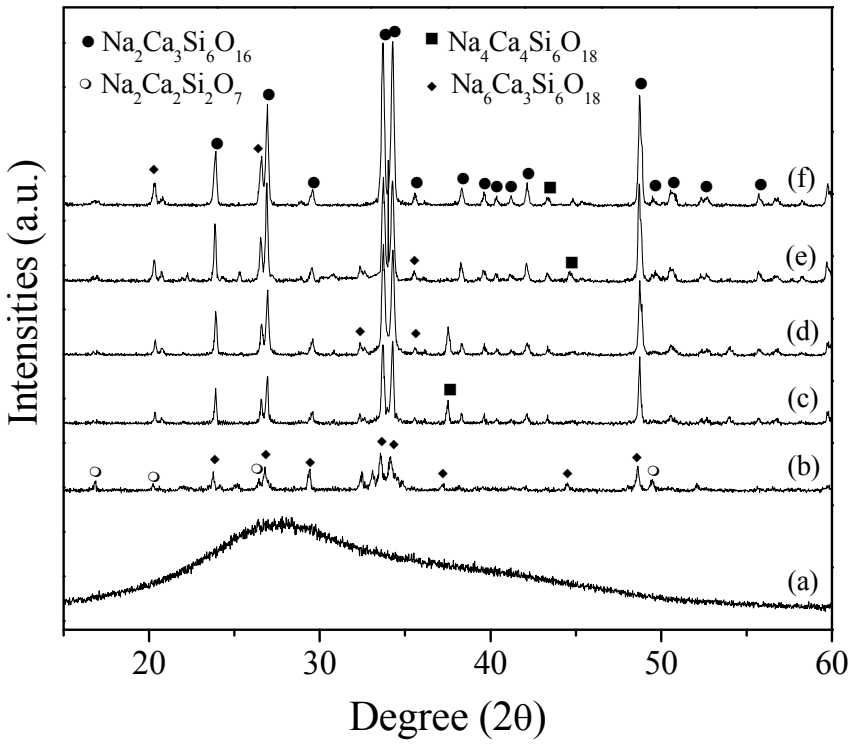

Fig. 4.45 XRD patterns of glass-ceramics; (a) as prepared (b) powder calcined at 700 ^oC, and pellet sintered at (c) 900, (d) 950, (e) 1000, (f) 1050 ^oC.

4.5.2.3 Particle Size Distribution of Glass-Ceramics Powder

After calcination, glass-ceramic powder was ground into fine particles. Fig. 4.46 shows the particle size distribution of glass-ceramic powder. A unimodal size distribution with average particle size (d_{50}) of 4.5 μm was obtained. The relatively small size of particles of

the glass-ceramic was due to its processing through sol-gel route. This powder was used for the preparation of glass-ceramic pellets through uniaxial compaction.

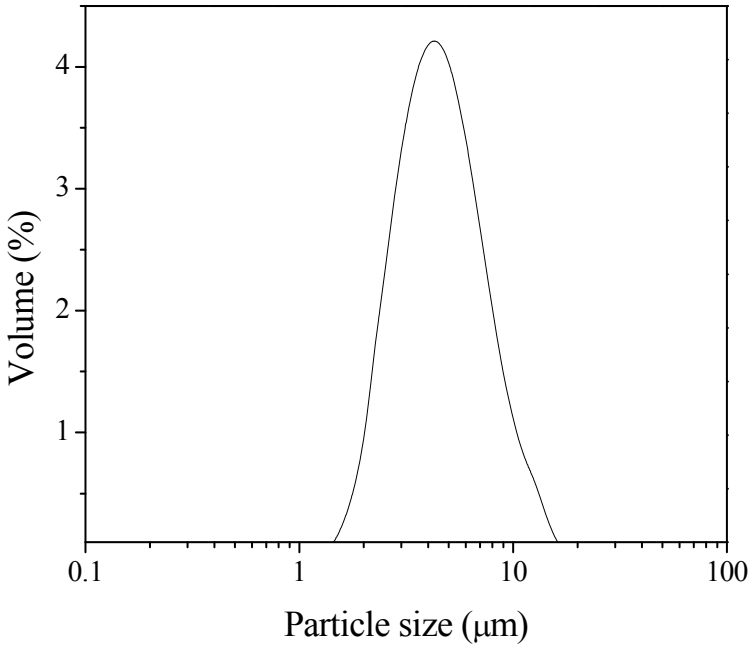

Fig. 4.46 Particle size distribution of glass-ceramics powder.

4.5.2.4 Mechanical and Microstructural Properties

Fig. 4.47 shows the bulk density, porosity and compressive strength of glass-ceramics specimen sintered at different temperatures. As expected, bulk density increases and porosity decreases with sintering temperature. Compressive strength increases with increasing sintering temperature up to 1000 ^{o}C followed by the decrease in strength at 1050 ^{o}C. Although, a substantial increase in bulk density and decrease in porosity were observed at this particular temperature. The increase in strength with sintering temperature is due to the classical sintering phenomena; where particle rearrangement, mass diffusion to pores and grain growth takes place.

To analyze the fall in strength at 1050 ^{o}C, microstructures of sintered specimens were investigated. Fig. 4.48 shows the surface microstructures of glass-ceramics sintered at different temperatures. The glass-ceramics has porous structure up to about 1000 ^{o}C. The precipitated ceramic phase shows (Fig. 4.48 (a)) acicular shapes. Fig. 4.48 (b) and(c) shows a low magnification view of porous structure.

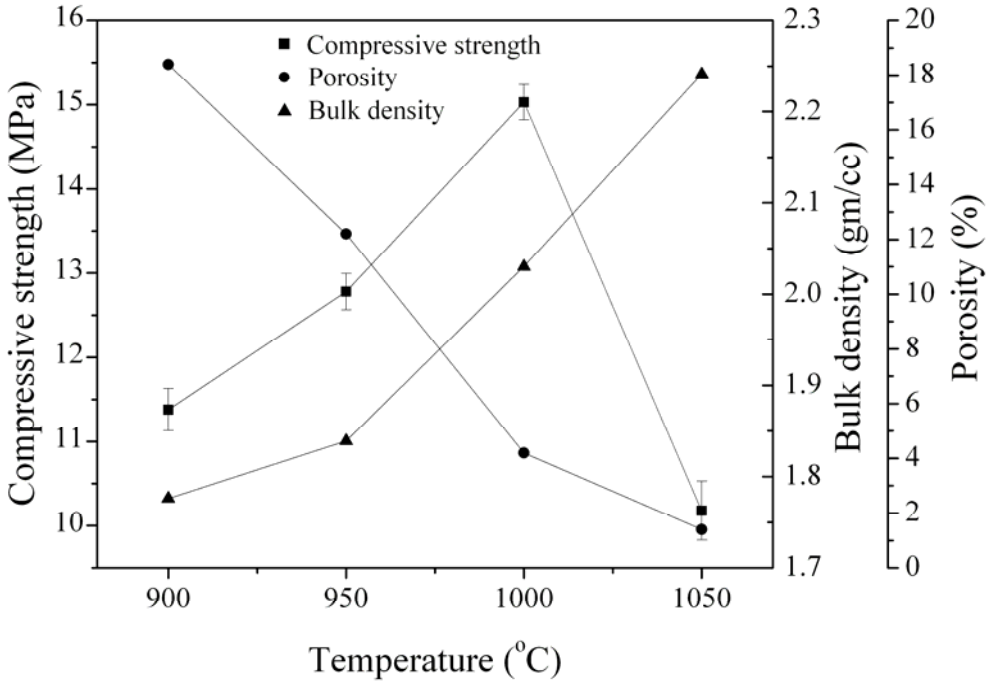

Fig. 4.47 Change of bulk density, porosity and compressive strength of glass-ceramics with sintering temperatures.

The partial melting of glass-ceramics can be observed at 1050 ^{o}C (Fig. 4.48 (d)) and it has faceted grains in monolithic pore free body. The porosity of the specimen was about 1% as shown in Fig. 4.47. Moreover, the BGC1050 microstructure shows many cracks in its surface. Formation of cracks may be due to the thermal expansion mismatch between ceramic and glassy matrix. Thus, the mechanical strength of BGC1050 was low due to the presence of cracks.

4.5.2.5 *In vitro* Bioactivity

4.5.2.5.1 Phase and Microstructural Analysis

The bioactivity of sintered (900 ^{o}C) glass-ceramics was assessed *in vitro* using SBF solution. Fig. 4.49 shows the XRD pattern of glass-ceramics surface incubated for different period of time in SBF along with untreated sample. The specimen without SBF treatment (zero days) shows typical sodium-calcium-silicate phases as described above. These crystalline phases are absent in 3-days SBF incubated specimen. 3-days specimen shows the presence of amorphous glassy phase and some amount of crystalline calcium-phosphate based phases.

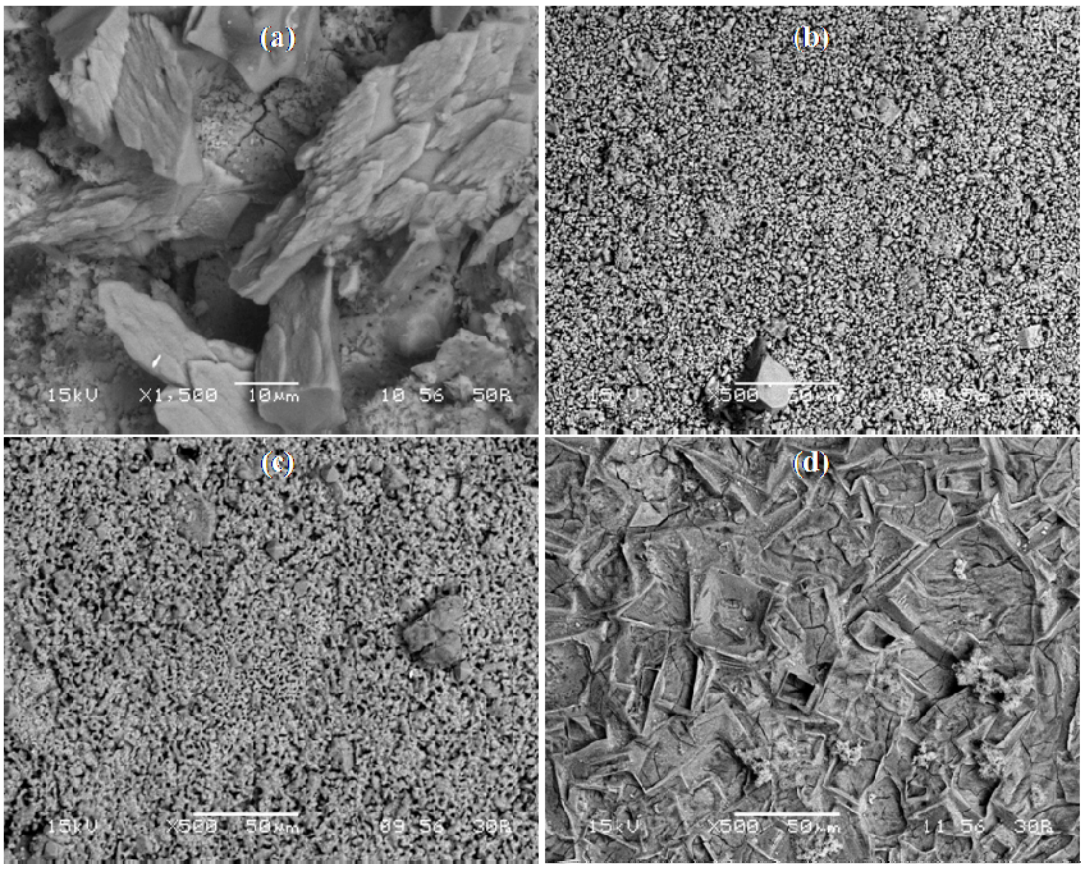

Fig. 4.48 Surface microstructures of glass-ceramics sintered at (a) 900, (b) 950, (c) 1000 and (d) 1050 ^{o}C.

Carbonated hydroxy apatite and hydrated calcium phosphate phases are identified in the specimen. The amount of these two phases increases in 14 and 21 days specimen. The amorphous glassy phase seems to increase in 14 days specimen. Formation of bone like apatite layer during bioactivity experiments was also evaluated by investigating the change of surface morphology.

Fig. 4.50 shows the surface morphology of glass-ceramics specimen; those incubated in SBF with different time periods along with EDS elemental analysis. Untreated glass-ceramics surface has acicular structured morphology (Fig. 4.50 (a)) with typical EDS spectra showing Si, Ca and Na. The surface morphology changes with incubation periods. 3-days surface shows the formation of individual apatite grains with size ~1 μm (Fig. 4.50 (b)). With increasing incubation periods, apatite grains grow into spherical shapes with an average diameter of ~1.5 μm size in 14-days (Fig. 4.50 (c)). 21-days surface (Fig. 4.50 (d)) shows ~ 5 μm size clusters with cauliflower like morphlogy

covering entire surface. The EDS spectra of these grain/clusters show the presence of P and C in addition to Na, Ca and Si; which indicates the formation of carbonated calcium phosphate hydrated phases.

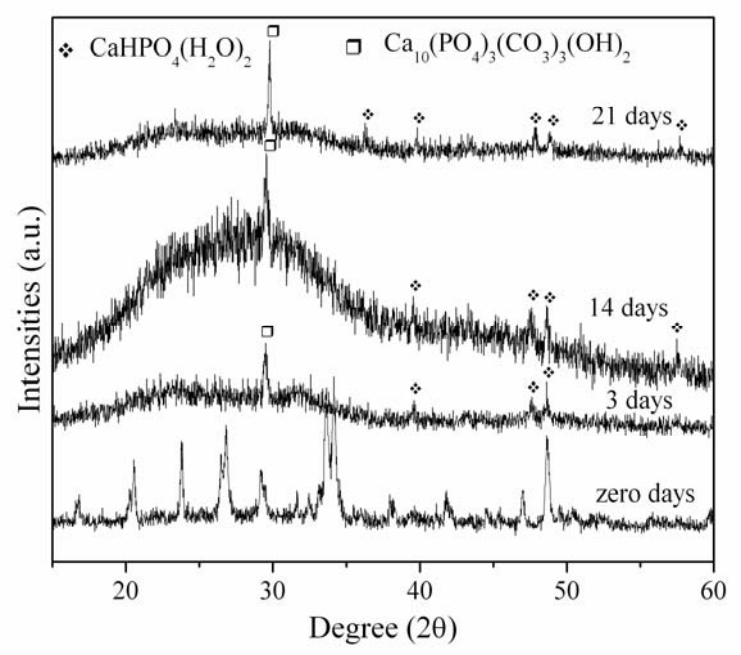

Fig. 4.49 XRD patterns of glass-ceramic surface after incubation in SBF for different time periods.

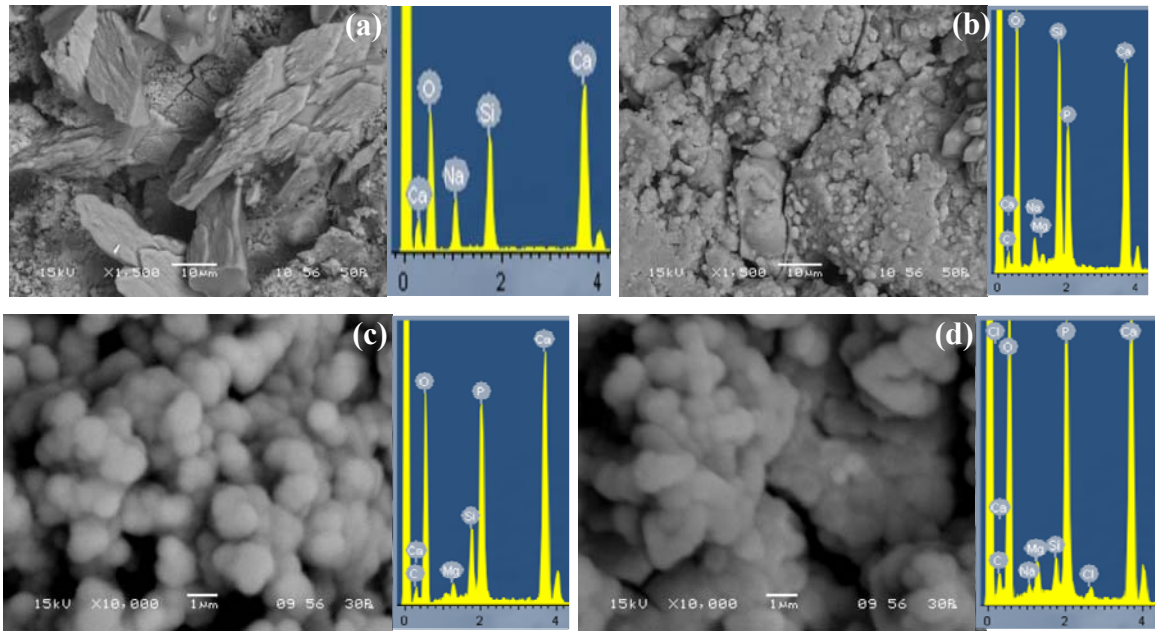

Fig. 4.50 SEM image and EDS spectra of glass-ceramics; (a) as prepared, and after incubation in SBF for (b) 3 (c) 14, and (d) 21 days.

The *in vitro* bioactivity was evaluated by checking the ability of bone like apatite phase formation on the surface of material in simulated body fluid. The glass-ceramics showed a good bioactivity *in vitro*. Hydrated calcium phosphate phase was formed within 3-days of incubation (Fig. 4.49). Sodium-calcium-silicate phases of glass-ceramics were completely dissolved in SBF within 3 days, due to the release of Na^+ and Ca^{2+} ions into the solution. Dissolution of surface ions leaves a glassy matrix on the surface. Glassy matrix increased in 14 days specimen; might be due to some structural changes in the matrix.

The apatite formation upon bioglass-ceramics is speculated to proceed by the following mechanism [31]: the glass-ceramic releases Ca^{2+}, Na^+ ions from its network via an exchange with the H^+ and H_3O^+ ions in SBF to form Si–OH groups on the surface. The Si–OH groups formed induce apatite nucleation through the formation of amorphous calcium silicate and calcium phosphate. Once nucleated, the apatite grows spontaneously as the body fluid is highly supersaturated with respect to apatite under normal condition. Released Ca^{2+}, Na^+ ions of glass-ceramics also accelerate apatite nucleation by increasing the ionic activity product of apatite in the fluid. It may be concluded that the glass-ceramics prepared in the present investigation, show a good bioactivity in 3 days and comparable to that of apatite-wollastonite (A-W) glass-ceramics [32, 33]. Good bioactivity of the glass-ceramics is due to its sol–gel origin during synthesis which provide abundant amount of Si-OH functional group on their surfaces [34] for apatite nucleation.

Acicular morphology of glass-ceramics is due to the precipitation of ceramics in glassy matrix (Fig.4.50 (a)). XRD analysis reveals that, ceramic dissolves in SBF within 3-days of incubation. The surface morphology also supports this as there are no acicular grains in 3-days surface (Fig. 4.50 (b)). Calcium hydrated phosphate phases are detected in 3, 14 and 21 days specimen. So, the grains and clusters shown by these surfaces (Fig. 4.50 (b-d)) are attributed to the formation of phosphate phases. Similar changes in apatite morphologies have been reported for sol-gel derived glasses and glass-ceramics [35].

4.5.2.5.2 Effect of Sintering on Bioactivity

Effect of sintering temperature on bioactivity of BGC was assessed *in vitro* using SBF solution. Fig. 4.51 shows the XRD pattern of different sintered glass-ceramic surface with those incubated for 3-days in SBF along with untreated sample. The specimen, without SBF treatment (zero days) shows typical sodium-calcium-silicate phase as described above. As observed previously, these crystalline phases are almost absent in BGC900 (Fig. 4.51 (b)). This is due to the dissolution of crystalline phases in SBF. Carbonated hydroxy apatite ($Ca_{10}(PO_4)_3(CO_3)_3(OH)_2$) and hydrated calcium phosphate ($CaHPO_4(H_2O)_2$) phases could be identified in the specimen. Crystalline peak of glass-ceramics sintered at higher temperature seems to be less affected by SBF incubation. These crystalline phases may be less soluble in SBF when sintered at higher temperature.

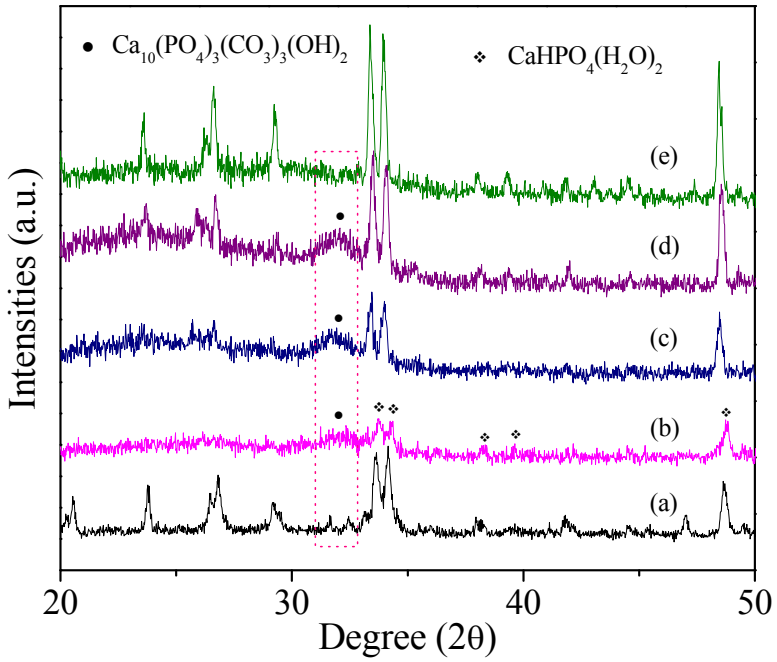

Fig. 4.51 XRD patterns of glass-ceramics specimen, (a) sintered at 900 ^{o}C; and the patterns after 3-days SBF incubation of specimen those sintered at (b) 900, (c) 950, (d) 1000, and (e) 1050 ^{o}C.

Fig. 4.52 shows the surface morphology and EDS graph of different sintered specimen which were incubated in SBF for 3days. EDS graphs show the presence of P and C in addition to Na, Ca and Si. This indicates the formation of carbonated calcium phosphate hydrate phases as described above. The spectra shows that the relative intensities of P and Ca compared to Si decrease with increasing sintering temperature. That is the apatite deposition decreases and it was lowest in BGC1050. The results show

that the apatite formation decreases in the order BGC900>BGC950>BGC1000>BGCl050. Heating of the glass-ceramics can modulate its structure and thus have an influence on apatite formation. Higher the sintering temperature, the material will have more crystalline phases and less glassy matrix. XRD analysis also showed the change in the types of crystalline phases with increasing temperature, which may influence the dissolution characteristics of glass-ceramics.

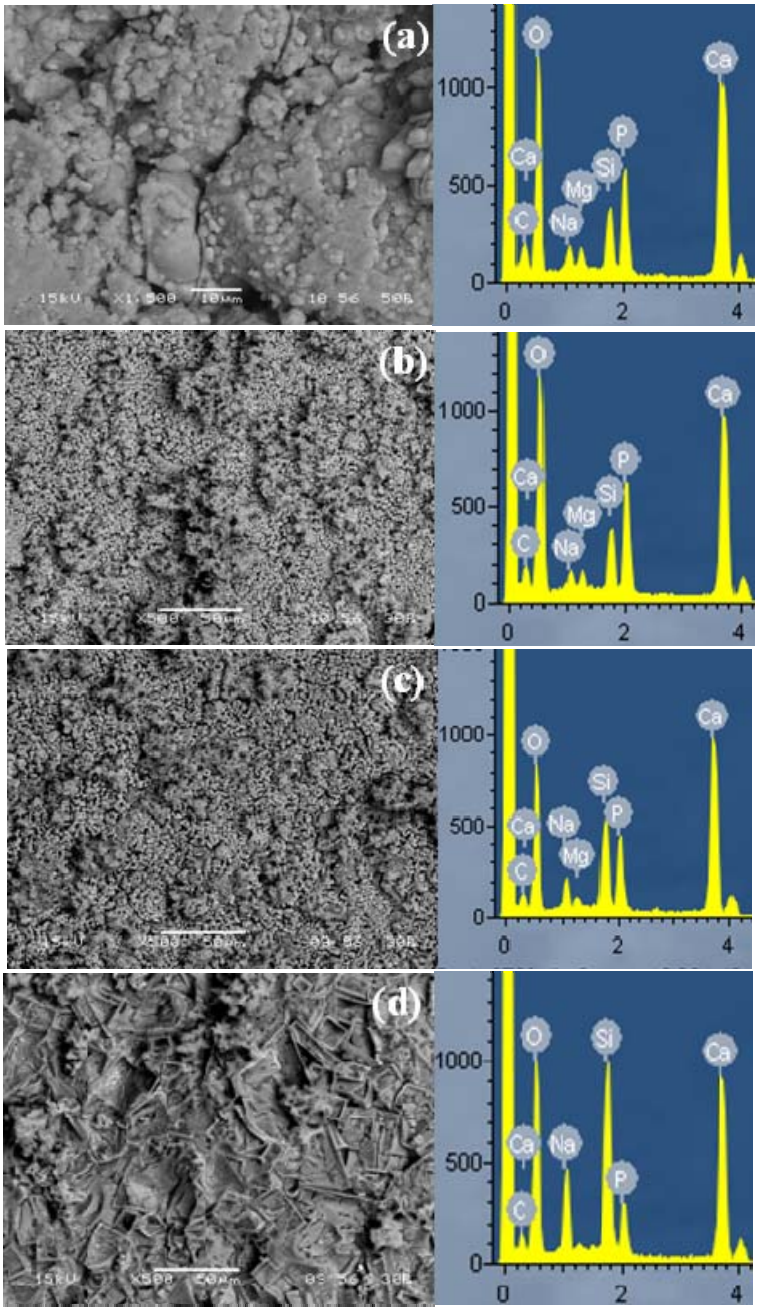

Fig. 4.52 SEM image and EDS spectra of 3-days SBF incubated glass-ceramic specimen sintered at (a) 900, (b) 950 (c) 1000, and (d) 1050 ^{o}C respectively.

4.5.2.6 *In vitro* Biodegradability

Biodegradability characteristic of bioceramics in body fluid is another important aspect of bioactivity for its practical clinical applications. Fig. 4.53 (a) and (b) shows the change in pH of TRIS buffer solution and water absorption capacity respectively with incubation time. Both water absorption capacity and pH of TRIS medium increased with increasing time. Both the phenomena were rapid up to about 1 day, moderate up to about 2 days and slow thereafter. The increment of pH and water absorption was highest for BGC900, intermediate for BGC1000 and lowest for BGC1050, respectively. This indicates that the biodegradability also decreases with increasing sintering temperature.

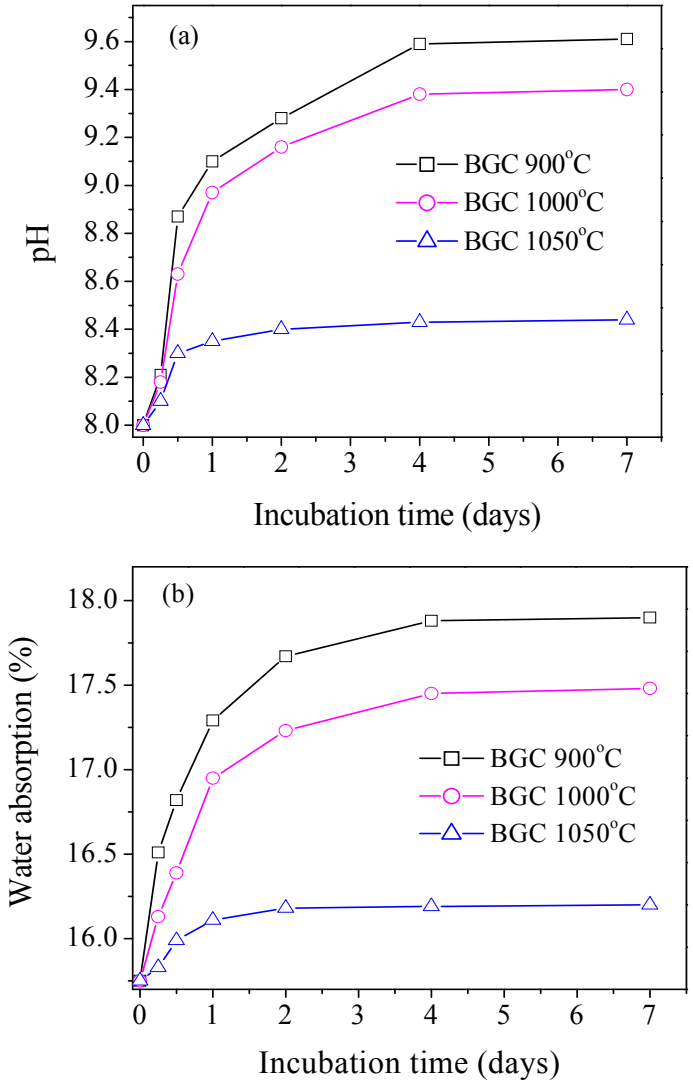

Fig. 4.53 Dissolution kinetics of glass-ceramic sintered at different temperatures; (a) Change in pH of TRIS medium, and (b) water absorption capacity of specimen with incubation period.

The dissolution of glass-ceramics depends on the presence of Ca^{2+} and Na^{+} within it [36, 37]. During dissolution, these ions were leached out from the glass-ceramic matrix, hence the pH of the medium increased. To compensate the leached out material of glass-ceramic, equivalent amount of water molecule diffused into the specimen and filled the void space created by the leached material; hence water absorption increased [38]. The rate of dissolution as well as the pH increment decreased after about 2 to 4 days due to the decrease in surface Ca^{2+} and Na^{+} ionic concentration.

It may be concluded that the biodegradability order is BGC900 > BGC1000 > BGCl050. Higher the sintering temperature, more will be the crystalinity of the material. That is the material will have more crystalline phase rather than glassy amorphous phase. It is known that biodegradability of amorphous material is higher than crystalline material. In addition, apparent porosity decreases with increasing sintering temperature as shown in Fig. 4.47. So, higher the sintered temperature, less permeable is the glass-ceramic to SBF solution and less will be the effective contact area between solid and liquid for dissolution.

4.5.2.7 Physical Model

Based on the study, a physical model similar to that proposed by Kokubo [39] may be used to explain these results. Fig. 4.54 shows the schematic model for bioactivity of glass-ceramics, which was presented by Kokubo et al for Na_2O-SiO_2 glass [40]. As per the model, ceramic combeite phases are considered to be embedded in glassy matrix and Ca, Na and silicate ions are dissolved from both the combite and the glassy matrix. pH of the medium increases due to high basicity of Na^{+} ion. The rate of dissolution as well as pH increment decreases after 3 to 4 days due to the decrease in the dissolving ions at the surface. The model also proposed that the dissolution of Ca^{2+} ion increases the degree of super saturation of surrounding fluid with respect to apatite and the dissolution of silicate ions provides favorable sites for nucleation of the apatite on the surface of glass-ceramic.

The present sol-gel glass-ceramic material shows good bioactivity and bio-dissolution within 3 days. It is well established that sol-gel bioglasses have higher bioactivity than melt driven bioglasses [41]. This is because the sol-gel processing has the advantage with respect to the control of material's surface chemistry which directly

relates to the bioactivity [42]. The major differences in surface chemistry between gel- and melt driven-glasses are [42]: (i) Gel-glass has a larger volume fraction of nanometre porosity on the surface; (ii) Gel-glass has a larger concentration of silanols on the surface; and (iii) Gel-glass has metastable three-membered and four-membered siloxane rings on the surface. All these surface chemistry render the gel driven glass or glass-ceramics a better bioactive material than conventional melt driven glass-ceramics. Results also show that, rice husk ash can successfully be used to synthesize a bioactive sol-gel glass-ceramics.

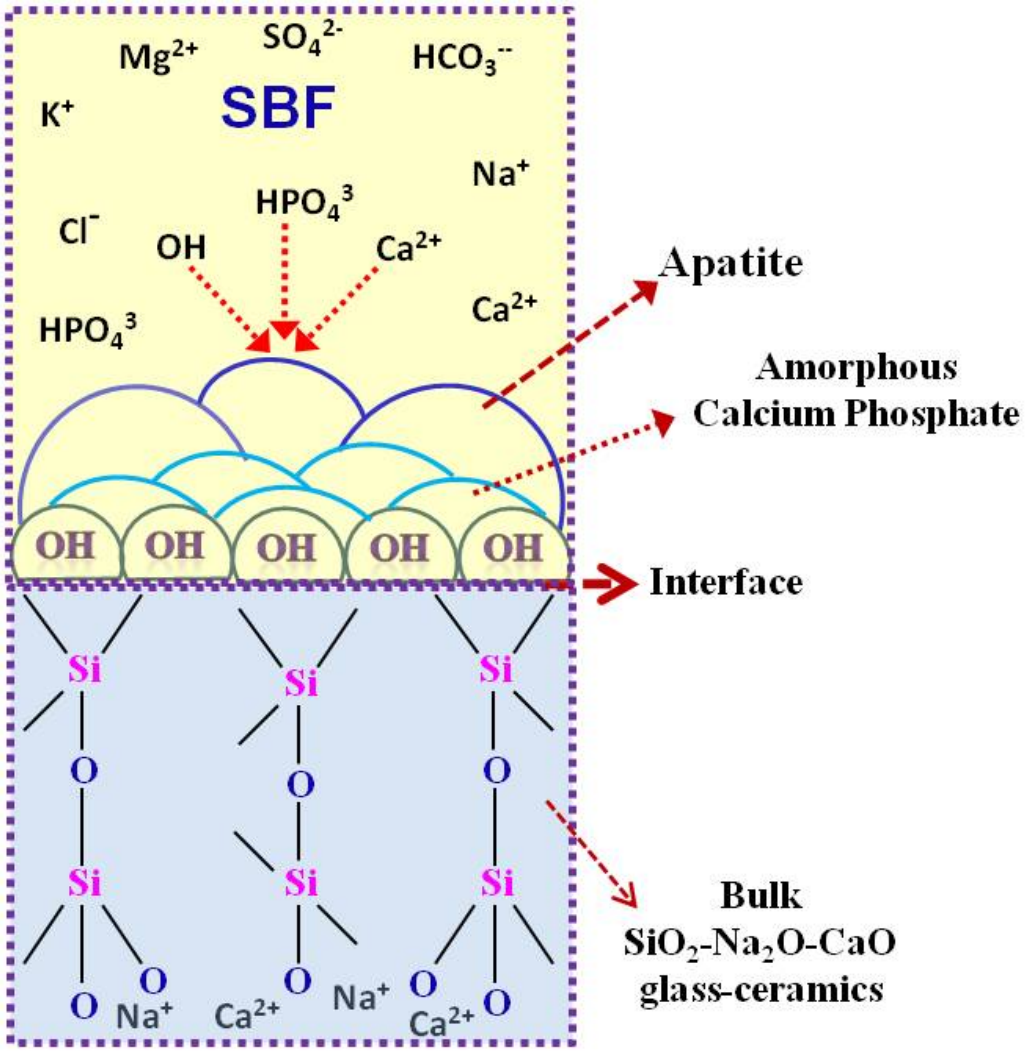

Fig. 4.54 Schematic diagram representing the events that takes place at the interface between bioglass-ceramics and the SBF. [T. Kokubo, Biomater 12 (1991) 155]

4.5.3. Summary

Soda-lime-silica based bioglass-ceramic was synthesized via sol-gel route utilizing sodium silicate, derived from rice husk ash. Gel powder was calcined at 700 ^{o}C for 2 h to get a reactive glass-ceramic powder. The calcined powder mainly contains combeite-I ($Na_6Ca_3Si_6O_{18}$) crystalline phase dispersed in amorphous glass matrix. Glass-ceramic specimens were sintered at different temperatures and better mechanical property was obtained with 1000 ^{o}C sintered glass-ceramics. Sintered pellets were tested for bio-activity and biodegradability. Crystalline combeite phase of the glass-ceramics was found to dissolve easily in SBF and TRIS buffer solution. Carbonated hydroxyapatite was formed on the surface of the glass-ceramics within 3 days of incubation in SBF. On increasing sintering temperature, both bioactivity and biodegradability of BGC specimens decreased. Finally, it may be concluded that rice husk ash may be a low cost raw material for the preparation of bioglass-ceramic materials through simple sol-gel route. The bioglass-ceramics should be heat treated at 1000 ^{o}C, to get better mechanical strength.

4.6. Silica Aerogel prepared by Ambient Pressure drying

4.6.1. Introduction

Silica aerogel was prepared from rice husk ash by sol-gel process followed by ambient pressure drying. Silica was extracted from ash as sodium silicate by boiling it in sodium hydroxide solution. Sodium silicate was neutralized with nitric acid to form silica gel. To prepare aerogel, first the pore water of the gel was exchanged by ethanol and then surface modification was done by aging alcogel in tetraethylorthosilicate (TEOS)/ethanol solution. Before drying, TEOS/ethanol solvent was exchanged with *n*-heptane. The nature of surface modification and thermal stability of the aerogel was studied by FTIR and DSC/TGA respectively. *In vitro* bioactivity of the aerogel was carried out by soaking in simulated body fluid. Surface deposition behaviour was characterized by X-ray diffraction, scanning electron microscopy and energy dispersive spectroscopy.

4.6.2. Results and Discussion

4.6.2.1 Ambient Pressure Drying Mechanism

The strength and stiffness of the wet silica gel was enhanced by aging it in TEOS/ethanol solution. Prior to this aging, the gel was thoroughly washed with ethanol. The strength and stiffness of gel may also increase by ethanol washing due to dissolution of silica from the particles and re-precipitation into the necks between the particles [43, 44]. However, it has been reported that the increase in strength and stiffness by such washing was not sufficient to avoid shrinkage during drying and hence, further aging in TEOS solution was necessary [45]. TEOS aging causes silica to precipitate from the aging solution onto the silica network. Precipitation of silica results in an increase in the density of the wet gel and corresponding strengthening and stiffening of the gel network [45]. During aging, hydrolysis of TEOS and condensation of silica gel occurs. The two reactions are stated below as reaction (4.2) and (4.3), respectively. Residual pore water and water by-product of condensation reaction (4.3) may be responsible for hydrolysis of TEOS. TEOS can also take part in condensation reaction with Si-OH group of gel structure (reaction- 4.4);

Hydrolysis :

$Si(OC_2H_5)_4 + 4H_2O \longrightarrow Si(OH)_4 + 4C_2H_5OH$ (4.2)

Condensation :

$Si(OH)_4 + (OH)_4Si \longrightarrow (OH)_3Si–O–Si(OH)_3 + H_2O$ (4.3)

$\equiv Si(OC_2H_5) + HO–Si\equiv \longrightarrow \equiv Si–O–Si\equiv + C_2H_5–OH$ (4.4)

After surface modification, TEOS/alcohol solution was replaced by *n*-heptane to prohibit crack formation during drying of the gel. Capillary stresses and associated drying shrinkage of gel were reduced due to the low surface tension of *n*-heptane.

4.6.2.2 Aerogel and its Characterization

The silica aerogel prepared from rice husk ash was a light, semi-translucent porous solid with an appearance as shown in Fig. 4.55. Bulk density and apparent porosity of the aerogel were 0.67 $g.cm^{-3}$ and 80% respectively.

Fig. 4.55 Photographs of silica aerogel (a) strengthened by TEOS, (b) dried monolithic translucent piece.

SEM and EDS micrographs of the dried aerogel specimen are shown in Fig. 4.56. The aerogel exhibits a sponge-like highly porous microstructure. The corresponding EDS spectra shows Si, O and very small amount of Na. Na was present in the gel matrix as sodium silicate solution was used for the preparation of aerogel.

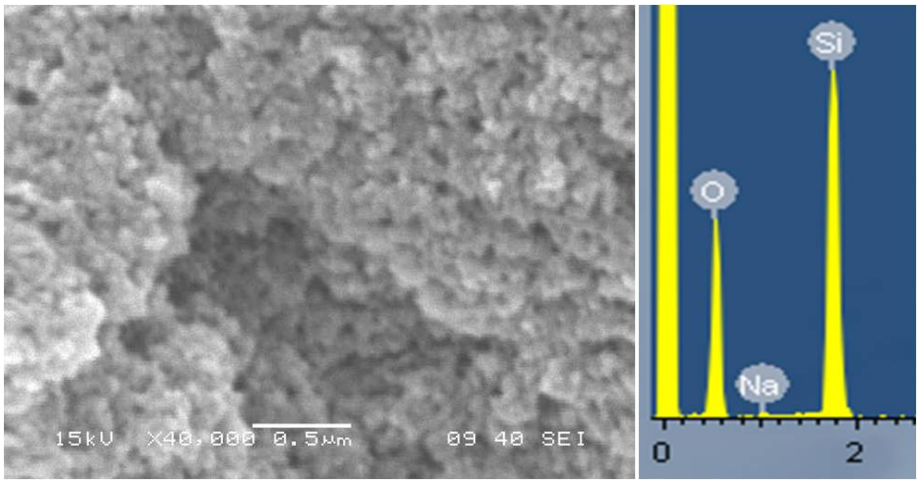

Fig. 4.56 SEM and EDS photographs of silica aerogel.

***Thermal Behaviour of Aerogel*:**

Fig. 4.57 shows the DSC/TGA curves of silica aerogel. A similar result of the weight loss for aerogel was observed by Folgar et al [46]. There is a sharp weight loss up to a temperature of 150 ^{o}C due to the evaporation of residual water from the aerogel. Further, the significant weight loss observed in the temperature range of 300-700 ^{o}C can be attributed to the progressive poly-condensation and dehydration of aerogel as stated above.

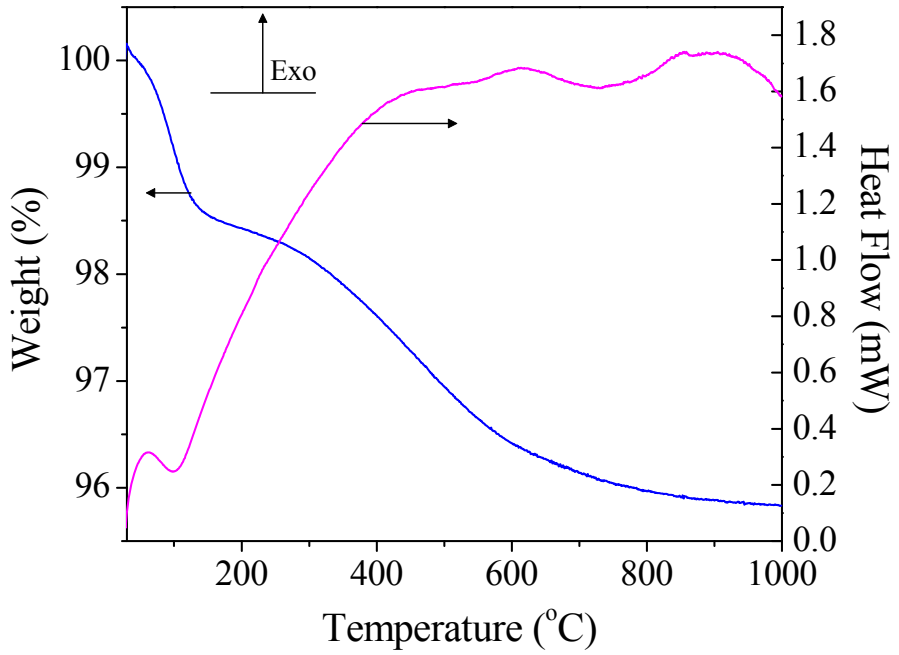

Fig. 4.57 DSC/TGA curves of air-dried silica aerogel.

***FTIR Analysis*:**

Fig. 4.58 shows FTIR spectra of the aerogel heated at different temperatures. There are characteristic bands of silica aerogel at ~ 1098, ~ 804 and ~ 471 cm^{-1}. The ~ 1098 cm^{-1} which is associated with the Si-O-Si asymmetric bond stretching vibration [47]; while, the band at ~ 804 cm^{-1} is assigned to a network Si-O-Si symmetric bond stretching vibration. The bands at ~ 471 cm^{-1} are associated with a network Si-O-Si bond bending vibration. The bands at ~ 960 cm^{-1} are associated with stretching mode Si-OH typical of gel structure. The intensity of this band decreased with increasing temperature due to polycondensation and dehydroxylation of gel [48]. The bands at ~ 3440 and ~ 1630 cm^{-1} are associated with the -OH absorption band which is caused by physically adsorbed water [49]. The intensity of these bands decreased with increasing temperature. The small absorption peaks at ~ 2927 and ~ 2856 cm^{-1} may be associated with $-OC_2H_5$ terminal group [50]. These peaks were absent in the aerogel which were heat treated above 400 ^oC.

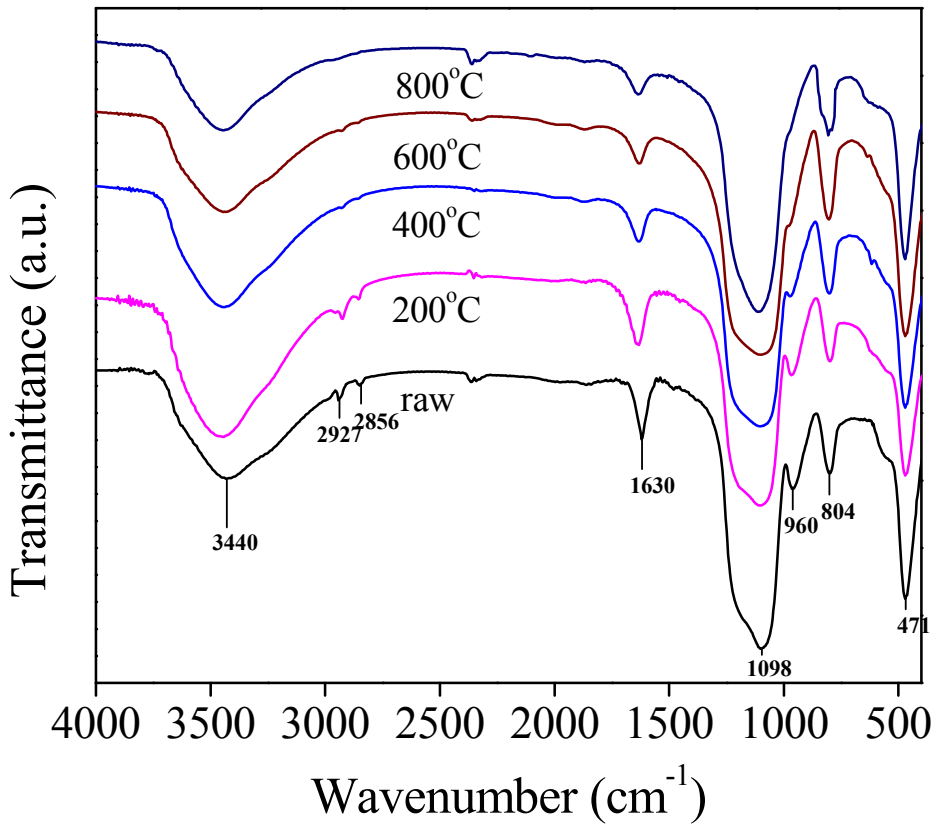

Fig. 4.58 FTIR spectra of silica aerogel after heating at different temperatures.

***Surface Area and Pore Size Distribution*:**

Fig. 4.59 shows the nitrogen adsorption-desorption isotherm of silica aerogel. BET surface area and total pore volume of the aerogel were 273 $m^2.g^{-1}$ and 3.1 $cm^3.g^{-1}$ respectively. The aerogel exhibited type-IV adsorption isotherm, which indicates the presence of mesopores [49]. Pore size distribution of the aerogel is shown in Fig. 4.60. The pores were in the range of 10-40 nm, i.e. in the mesoporous range.

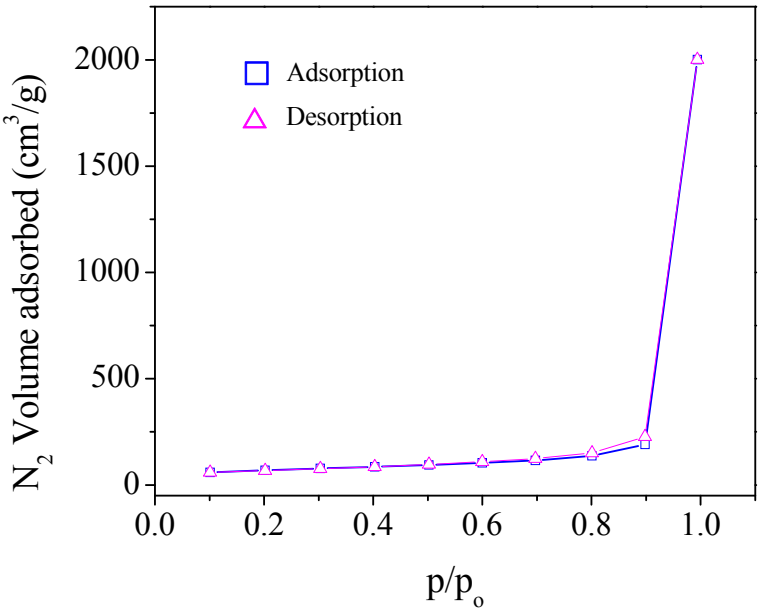

Fig. 4.59 Nitrogen adsorption-desorption isotherm of silica aerogel.

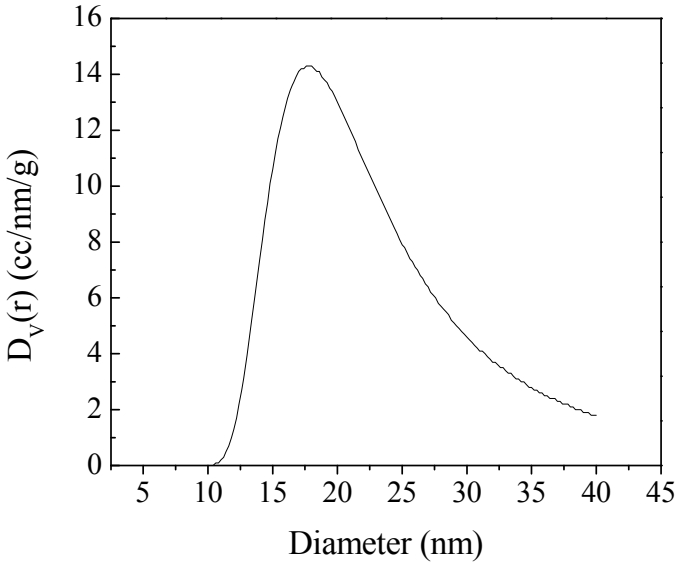

Fig. 4.60 Pore size distribution of silica aerogel.

4.6.2.3 *In vitro* Bioactivity

Fig. 4.61 represents SEM images and EDS spectra of aerogel surface after incubation in SBF for 7, 14 and 21 days. Apatite layer formed on the surface of aerogel specimen (Fig. 4.61 (a)). As the incubation days increases, the deposition of sponge-wig shaped hydroxyapatite (HAp) layer on the surface increased and the entire surface was almost covered in 21 days (Fig. 4.61 (c)). The corresponding EDS spectra for each micrograph show the intensities for Si, Ca and P along with C, which confirmed the carbonated hydroxyapatite deposition over aerogel. As incubation periods increased, intensities of both P and Ca increased due to more apatite formation with time. EDS also shows the presence of Na, Mg and Cl, because these ions were present in the body fluid.

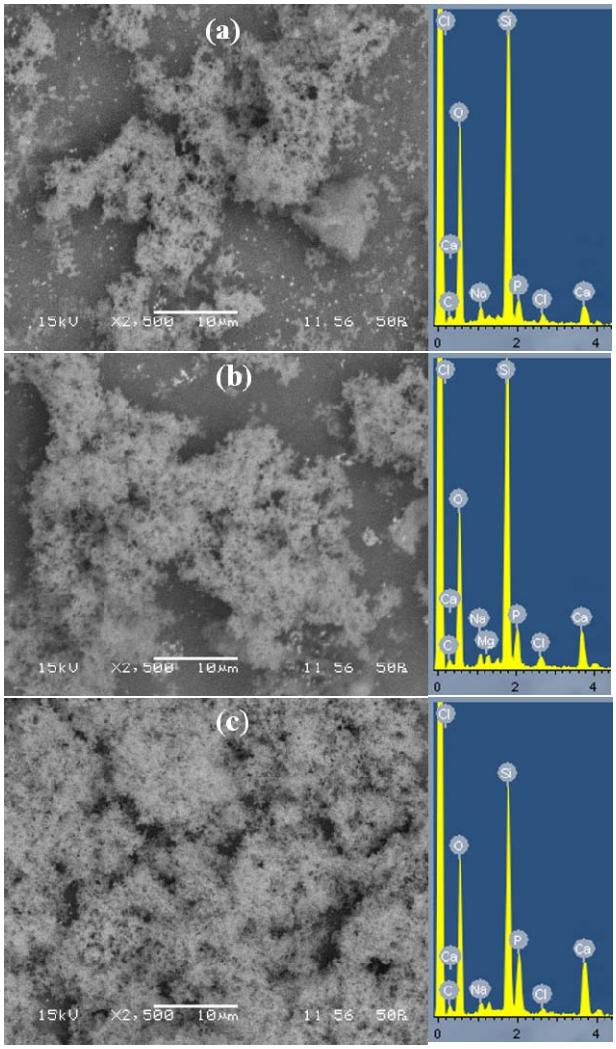

Fig. 4.61 SEM images and EDS spectra of aerogel after incubation in SBF for (a) 7 (b) 14 and (c) 21 days.

Fig. 4.62 displays the XRD pattern of the aerogel specimens without and with soaking in SBF for 21 days. The characteristic diffraction peaks of HAp were identified and were very similar to that reported pattern [51]. This confirms the bioactivity of the aerogel.

The mechanism for apatite nucleation and growth on the surface of silica aerogel is believed to be the formation of Si-OH functional group on the surface due to the hydration and dissolution of silica network. Hydrolysis of silica network leads to the release of soluble $Si(OH)_4$ into the body fluid. Simultaneously, Si-OH groups are formed at the solid-fluid interface. This group provides favorable sites for apatite nucleation [16]. Once nucleated, the apatite can grow spontaneously as the body fluid is highly supersaturated with respect to apatite under normal condition. Presence of large volume of porosity and high surface area of aerogel accelerate the formation of silanols and apatite in it.

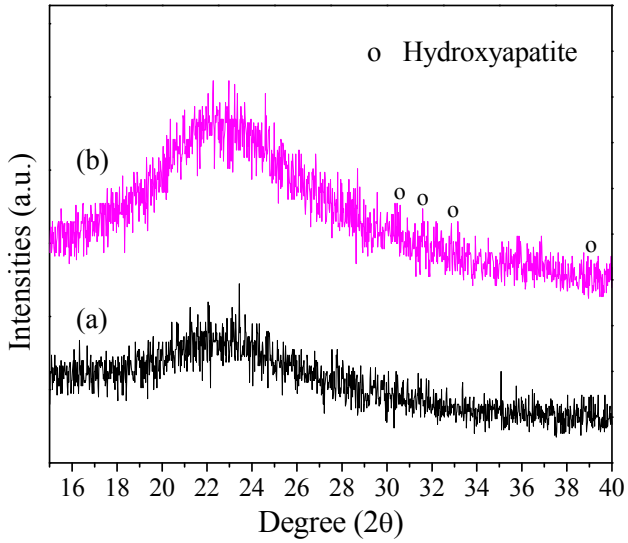

Fig. 4.62 XRD pattern of aerogel specimen (a) without, and (b) after 21-days incubation in SBF.

4.6.2.4 *In vitro* Biodegradability Study

Degradation of biomaterials in body fluid is another important characteristic. Biodegradability of aerogel specimen was carried out in TRIS medium. Fig. 4.63 shows the change in Si concentration and pH in TRIS buffer solution with incubation time during dissolution experiment. Si concentration increases as well as pH decreases with increasing time. Silica dissolves into body fluids as silicic acid. For that reason, pH decreases. Silica network dissolution was rapid up to about 6 h after which the rate

decreased due to the saturation of medium with respect to silicic acid. The rate of Si dissolution from the gel matrix was higher than the other silica ceramics which were studied in earlier section. This is due to the presence of nanometer range pores within the gel matrix with higher surface area. From the dissolution test, it may be concluded that the silica aerogel prepared using RHA as silica source and through ambient pressure drying method is degradable in biological environment.

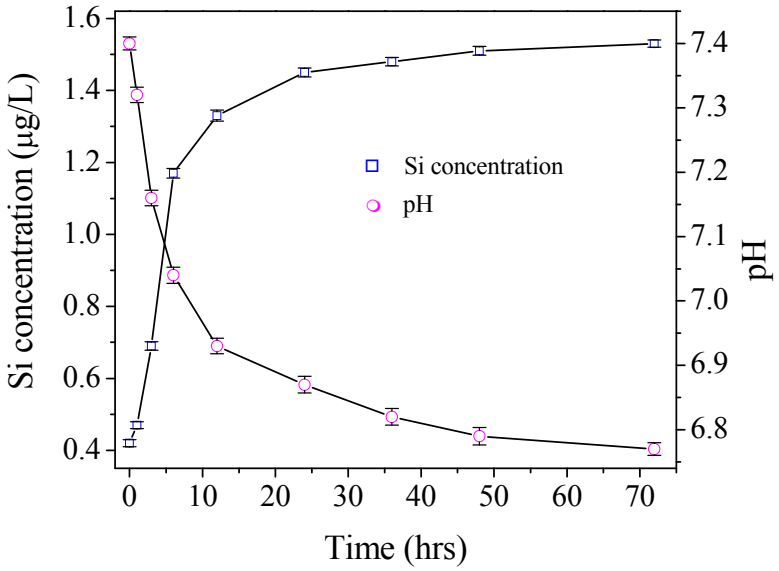

Fig. 4.63 Change of silicon concentration and pH in TRIS medium with incubation time for aerogel during biodegradation.

4.6.3. Summary

Using the sol-gel route and ambient pressure drying technique, it was possible to obtain the monolithic silica aerogel with low density (0.67 $g.cm^{-3}$), high porosity (80%) and a specific surface area of 273 $m^2 g^{-1}$. The process of aerogel production from rice husk ash by ambient pressure drying method is very important from the industrial point of view and it will significantly widen the commercial exploitation of the silica aerogel. The aerogel was tested for its bio-activity and degradability. Carbonated HAp was formed on aerogel surface within 7 days of incubation in SBF. Biodegradability of aerogel in TRIS buffer solution showed quick release of silicic acid. Quick dissolution of silica could be the reason for quick deposition of HAp during SBF incubation. Hence, the aerogel can be used as novel low cost biomaterial for different clinical applications like; biosensor, drug delivery, and protein encapsulations etc.

References

[1] W. Panpa, S. Jinawath, Appl. Catalysis B: Environ. 90 (2009) 389.

[2] J. H. Anderson, G. A. Parks, J. Phy. Chem. (1968) 3662.

[3] D. W. Sindorf , G. E. Maciel, J. Am. Chem. Soc. 103 (1981) 4263.

[4] W.A. Deer, R.A. Howie, J. Zussmaan, Rock Forming Minerals, Longmans, London (1963).

[5] W. Panpa, S. Jinawath, Appl. Catal.B: Environ. 90 (2009) 389.

[6] T-H. Liou, Mater. Sci. Eng. 364A (2004) 313.

[7] S. Chandrasekhar, K.G. Satyanarayana, P.N. Pramada, P. Raghavan, T.N. Gupta, J. Mater. Sci. 38 (2003) 3159.

[8] F. Adam, J-H. Chua, J. Colloid Interface Sci. 280 (2004) 55.

[9] X A. Bertoluzza, C. Fagnano, M.A. Morelli, J. Non-Cryst. Solids 48 (1982) 117.

[10] K.S. Finnie, J.G. Thompson, R.L. Withers, J. Phys. Chem. Solids 55 (1994) 23.

[11] I.P. Swainson, M.T. Dove, D.C. Palmer, Phys. Chem. Miner. 30 (2003) 353.

[12] J.Y. Ying, J.B. Benziger, Nanostruct. Mater. 1 (1992) 149.

[13] M.N. Rahaman, Ceramic Processing and Sintering. CRC Press (2^{nd} Edition) Taylor & Francis Group (2003).

[14] T. Kokubo, H. Kushitani, S. Sakka, T. Kitsugi, T. Yamamuro, J. Biomed. Mater. Res. 24 (1990) 721.

[15] D. Arcos, D.C. Greenspan, M. Vallet-Regi, J.Biomed.Mater.Res. 65A (2003) 344.

[16] A.V. Lluch, G. Ferrer, M. Pradas, Polymer 50 (2009) 2874.

[17] D. Arcos, I. Izquierdo-Barba, M. Vallet-Regi, J. Mater Sci:Mater Medecine 20 (2009) 447.

[18] L.T. Zhuravlev, Colloids and Surf. (A) 173 (2000) 1.

[19] M.D. Sacks, Am. Ceram. Soc. Bull. 63 (1984) 1510.

[20] Q.Z. Chen, I.D. Thompson, A.R. Boccaccini, Biomater. 27 (2006) 2414.

[21] H.Y. Zhao, J. Long, J.H. Masliyah, Z. Xu, Ind. Eng. Chem. Res. 45(2) (2006) 7482.

[22] M.J. Crimp, R.E. Johnson, J.W. Halloran, D.L. Feke, Colloidal behavior of silicon carbide and silicon nitride, Wiley, New York (1986).

[23] L.J. Giibson, M.F. Ashby, Cellular solids: structure and properties. 2nd ed. Pergamon, Oxford (1999).

[24] Q. Fu, M.N. Rahaman, B.S. Bal, R.F. Brown, D.E. Day, Acta Biomater. 4 (2008) 1854.

[25] H. Yichen, W. Zhongjian, L. Jianying, J. Non-Cryst. Solids 354 (2008) 1285.

[26] D. Kong, H. Yang, S. Wei, D. Li, J. Wang, Cerm. Intl. 33 (2007) 133.

[27] E.A. Dancy, P. Nguyen-Duy, Thermo. Acta 42 (1980) 59.

[28] C. Ettarh, A.K. Galwey, Thermochimica Acta 288 (1996) 203–219.

[29] Y. Hoshino, T. Utsunomiya, O. Abe, Bull. Chem. Soc. Jpn 54 (1981) 1385.

[30] J. Phalippou, M. Prassas, J. Zarzycki, J. Non-Cryst. Solids 48 (1982) 17.

[31] O. Peital, E.D. Zanotto, L.L. Hench, J. Non-Cryst. Solids 292 (2001) 115.

[32] T. Kokubo, H. Takadama, Biomater 27 (2006) 2907.

[33] T. Kokubo, Biomater 12 (1991) 155.

[34] T. Kokubo, S. Ito, T. Huang, T. Hayashi, S. Sakka, T. Kitsugi, J. Biomed. Mater. Res. 24 (1990) 331.

[35] M. Mami, A. Lucas-Girot, H. Oudadesse, R. Dorbez-Sridi, F. Mezahi, E. Dietrich, Appl. Surf. Sci. 254 (2008) 7386.

[36] M.G. Cerruti, D. Greenspan, K. Powers, Biomater 26 (2005) 4903.

[37] D.A. Cortes, A. Medina, J.C. Escobedo, S. Escobedo, M.A. Lopez, J. Biomed. Mater. Res. A 70 (2004) 341.

[38] B.C. Bunker, J. Non-Cryst. Solids 179 (1994) 300.

[39] T. Kokubo, Biomater 12 (1991) 155.

[40] T. Kokubo, Materials Science and Engineering C 25 (2005) 97.

[41] L.L. Hench, R.J. Splinter, W.C. Allen, T.K. Greenlee, J. Biomed. Mater. Res. 5 (1972) 117.

[42] W. Cao, L.L. Hench, Ceram. Int. 22 (1996) 493.

[43] S. Haereid, E. Nilsen, V. Ranum, M. A. Einarsrud, J. Sol-Gel Sci.Tech. 8 (1997) 153.

[44] S. Haereid, J. Anderson, M. A. Einarsrud, D. W. Hua, D. M. Smith, J. Non-Cryst. Solids 185 (1995) 221.

[45] S. Haereid, E. Nilsen, M. A. Einarsrud, J. Non-Cryst. Solids, 204 (1996) 228.

[46] C. Folgar, D. Folz, C. Suchicital, D. Clarck, J. Non-Cryst. Solids 353 (2007) 1483.

[47] A. E. Ahmed, F. Adam, Micropor. Mesopor. Mater. 103 (2007), 284.

[48] Bertoluzza, C. Fagnano, M. A. Morelli, V. Gottardi, M. Guglielmi, J. Non-Cryst. Solids 48 (1982) 117.

[49] F. Shi, L. Wang, J. Liu, Mater. Lett. 60 (2006) 3718.

[50] H. Yokogawa, M. Yokoyama, J. Non-Cryst. Solids 186 (1995) 23.

[51] J.A. Toledo-Fernandez, R. Mendoza-Serna, V. Morales, N. Rosa-Fox, M. Pinero, A. Santos, L. Esquivias, J Mater Sci: Mater. Med. 19 (2008) 2207.

Chapter 5

Epilogue

5.1 Conclusions

(a) Amorphous silica precursor powders of 96, 99.79, and 99.87% purity were successfully prepared from waste material rice husk or rice husk ash through different processing route.

(b) Amorphous silica was found to transform into cristobalite phase upon heat treatment in the range 1000 to 1300 ^{o}C. The crystallization temperature was highly dependent on impurity content in the order higher the impurities lower the transformation temperature.

(c) The mechanical strength of sintered amorphous silica body was found to decrease as and when silica transformed from amorphous to crystalline. Decreased strength was due to the crack formation in sintered body by high to low displacive phase transformation of cristobalite.

(d) Amorphous silica ceramics were found to be bioactive *in vitro*. The bioactivity decreased with increase in sintering temperature as well as decreasing impurity content.

(e) Similarly, all ceramics showed a good biodegradability, which decreased with increase in sintering temperature as well as decreasing impurity content.

(f) Amorphous silica-based bioactive ceramics were successfully fabricated through conventional pressing, polymeric sponge replication and gelcasting method.

(g) Ceramics made of silica gel powder showed better mechanical strength than others.

(h) Ceramics fabricated through (i) conventional pressing had a dense body (less than 5% porosity), (ii) sponge replication had 80 % porosity (~ 550 μm pore size) and (iii) gelcasting had ~ 25% porosity.

(i) Amorphous silica ceramics made through gelcasting of silica gel powder showed better mechanical strength than other fabrication methods.

(j) SiO_2-Na_2O-CaO based bioglass-ceramics was prepared successfully by sol-gel technique using rice husk ash as silica source. Glass-ceramics showed best bioactivity among all silica-based ceramics studied. The material showed HAp formation within 3-days of SBF incubation.

(k) Bioactive silica aerogel was prepared through cost effective ambient pressure drying technique using rice husk ash as silica source. Mesoporous (85% porosity, ~ 20 nm pore size), translucent, monolithic aerogel was successfully fabricated. A good *in vitro* bioactivity and biodegradability characteristics was observed in the aerogel, which promises for its drug delivery applications.

5.2 Scope for Future Work

- *In vivo* bioactivity characterization, cytotoxicity characterization of all three types of amorphous silica-based ceramics.
- Preparation of scaffold through polymeric sponge replication method using bioglass-ceramics powder synthesized using RHA and its in vivo characterization.
- Preparation and characterization of encapsulated monolithic silica aerogel beads- for drug delivery application.
- Commercializing the above biomaterials.

Publications Resulting from the Ph. D. Work

1) **J.P. Nayak**, J. Bera, "Preparation of silica aerogel form rice husk ash by ambient pressure drying process using rice husk ash as raw material"; **Transaction of Indian Ceramic Society**, 68 (**2009**) 1-4.
2) **J.P. Nayak**, J. Bera, "Effect of sintering temperature on phase-formation behavior and mechanical properties of silica ceramics prepared from rice husk ash"; **Phase Transitions**, 82 (**2009**) 879-888.
3) **J.P. Nayak**, S. Kumar, J. Bera, "Sol-gel synthesis of bioglass-ceramics using rice husk ash as a source for silica and its characterization"; **Journal of Non-Crystalline Solids**, 356 (**2010**) 1447-1451.
4) **J.P. Nayak**, J. Bera, "Effect of sintering temperature on mechanical behaviour and bioactivity of sol-gel synthesized bioglass-ceramics using rice husk ash as a silica source", **Applied Surface Science**, 257 **(2010)** 458-462.
5) **J.P. Nayak**, J. Bera, "*In vitro* bioactivity of amorphous silica ceramics derived from rice husk ash", **Silicon**, DOI 10.1007/s12633-010-9058-3.
6) **J.P. Nayak**, J. Bera, "*In vitro* characterization of mesoporous silica aerogel monoliths prepared by ambient pressure drying process using rice husk ash", (**under review-J of Non-Crystalline Solids**).
7) **J.P. Nayak**, J. Bera, "Mechanical and *in vitro* performance of amorphous silica based scaffolds prepared by polymer sponge replication technique", (**under review-J of Porous Materials**).
8) **J.P. Nayak**, J. Bera, "Mechanical properties of amorphous Silica-based Ceramics fabricated through gelcasting method"; (**to be communicated**).

Publications not Related to the Ph. D. Work

1) J.P. Nayak, J. Bera; "A simple method for production of humidity indicating silica gel from rice husk ash"; **J. of Metals, Materials and Minerals**; 19 (**2009**) 15-19.
2) J.P. Nayak, J. Bera; "Preparation of an efficient humidity indicating silica gel from rice husk ash"; (**under review-Bulletin of Materials Science**).

Curriculum Vitae

Jyoti Prakash Nayak
S/O Mr. Aruna Kumar Nayak
Village & PO-Bancho, Dist-Keonjhar, Odisha-758022
Phone No: +91 6612464208, +91 9437655102
E-mail: Jyotiprakash_nitrkl@rediffmail.com

Date of Birth: 02.06.1975

Education: Ph. D. (Submitting), M. Tech. (Chemical Engg.), B.E. (Chemical Engg.)

Research Interest: Rice Husk, Amorphous Nano Silica, Sol-Gel, Gelcasting, Porous Ceramics, Bioceramics,

Technical Exposure: Publication: **9**, Conference: **07**

Work Experience: (i) A Dissertation submitted in partial fulfillment of the requirements for the degree of Master of Technology "*Effect of Fluidizing velocity in Tapered Fluidized Bed*".

(ii) Teaching faculty in Chemical Engineering Department, GIET Gunupur, Odisha.

Publications:

1) J.P. Nayak, J. Bera; "A simple method for production of humidity indicating silica gel from rice husk ash"; *J. of Metals, Materials and Minerals*; 19 (2009) 15-19.
2) J.P. Nayak, J. Bera; "Preparation of silica aerogel form rice husk ash by ambient pressure drying process using rice husk ash as raw material"; *Trans. Ind. Ceram. Soc.*; 68 (2009) 1-4.
3) J.P. Nayak, J. Bera; "Effect of sintering temperature on phase-formation behavior and mechanical properties of silica ceramics prepared from rice husk ash"; *Phase Transitions*; 82 (2009) 879-888.
4) J.P. Nayak, S. Kumar, J. Bera; "Sol-gel synthesis of bioglass-ceramics using rice husk ash as a source for silica and its characterization"; *J. Non-Cryst. Solids;* 356 (2010) 1447-1451.
5) J.P. Nayak, J. Bera; "Effect of sintering temperature on mechanical behaviour and bioactivity of sol-gel synthesized bioglass-ceramics using rice husk ash as a silica source"; Applied Surface Science, 257 (2010) 458-462.
6) J.P. Nayak, J. Bera; "*In vitro* bioactivity of amorphous silica ceramics derived from rice husk ash"; *Silicon*, DOI 10.1007/s12633-010-9058-3.
7) J.P. Nayak, J. Bera; "*In vitro* characterization of mesoporous silica aerogel monoliths prepared by ambient pressure drying process using rice husk ash"; (under review).
8) J.P. Nayak, J. Bera; "Mechanical and *in vitro* performance of amorphous silica based scaffolds prepared by polymer sponge replication technique"; (under review).
9) J.P. Nayak, J. Bera; "Low cost silica based porous bioceramics by gelcasting technique"; (Communicated).

Professional Membership:

• Associate Membership: Indian Institute of Chemical Engineers (IIChE) [AM-5069].